SAPIENZA
UNIVERSITÀ DI ROMA

Searches for Long-Transient Gravitational Waves from Newborn Magnetars Triggered by Electromagnetic Counterparts with Current and Next-Generation Detectors

Dipartimento di Fisica
Dottorato di Ricerca in Fisica (XXXVIII cycle)

Sandhya Sajith Menon
ID number 2132808

Advisor
Prof. Pia Astone

Co-Advisor
Prof. Dafne Guetta

Academic Year 2025/2026

Searches for Long-Transient Gravitational Waves from Newborn Magnetars Triggered by Electromagnetic Counterparts with Current and Next-Generation Detectors

PhD thesis. Sapienza University of Rome

This thesis has been typeset by LaTeX and the Sapthesis class.

Author's email: sandhya.sajithmenon@uniroma1.it

"Somewhere, something incredible is waiting to be known."

— Carl Sagan

Abstract

Long-transient gravitational waves, lasting from hours to days, form an intermediate class of signals between short-duration compact binary coalescences and persistent continuous waves. A promising source of such signals is the newborn magnetar: a rapidly rotating, highly magnetised neutron star formed in a core-collapse supernova or binary neutron star merger. Strong internal magnetic fields can induce non-axisymmetric deformations in the stellar structure, driving gravitational-wave emission at twice the rotation frequency while causing the star to spin down on timescales of hours to days.

In this thesis, we use a signal model for long-transient gravitational waves from newborn magnetars in the regime where spin-down is dominated by gravitational-wave emission. The waveform is characterised by a continuously decreasing frequency and strain amplitude, governed by the initial spin frequency and ellipticity of the source. We implement this model within an improved version of the Generalized Frequency Hough search pipeline, GFH-v2, which is designed to efficiently track such signals over large parameter spaces.

We validate the GFH-v2 pipeline through an extensive injection study using LIGO O4a data, characterising its sensitivity as a function of source parameters and establishing the detection threshold and follow-up procedure. We then apply the pipeline in a directed search for gravitational-wave emission from the possible magnetar remnant of SN 2023ixf, one of the nearest core-collapse supernovae of the last decade in the M101 galaxy, using data from LIGO Engineering Run 15 (ER15).

In parallel, we develop a multi-messenger framework connecting magnetar spin-down to shock-breakout emission observable in the near-ultraviolet, with particular application to the upcoming ULTRASAT satellite mission. We compute the expected UV light curves, detection horizons, and event rates for magnetar-driven supernovae, demonstrating that ULTRASAT will be able to identify magnetar-forming events and provide electromagnetic triggers for directed gravitational-wave searches.

No evidence for gravitational-wave emission associated with SN 2023ixf is found in the analysed data. We thus place upper limits on the maximum detectable distance as a function of initial frequency and ellipticity. While these limits fall below the distance to SN 2023ixf, they represent a sensitive directed search of these signals applied to ER15 data and demonstrate the operational readiness of the GFH-v2 framework for future searches. The methods and results presented here provide a foundation for long-transient searches targeting nearby core-collapse supernovae in forthcoming LIGO-Virgo-KAGRA observing runs.

Contents

List of Figures

Abbreviations

- ASD - Amplitude Spectral Density
- AXP - Anomalous X-ray Pulsar
- BNS - Binary Neutron Star
- BSD - Band Sampled Data
- CBC - Compact Binary Coalescence
- CCSN - Core-Collapse Supernova
- CCSNe - Core-Collapse Supernovae
- CE - Cosmic Explorer
- CR - Critical Ratio
- CSM - Circumstellar Material
- CW - Continuous Wave
- Dec - Declination
- EM - Electromagnetic
- EOS - Equation of State
- ER15 - Engineering Run 15
- ET - Einstein Telescope
- FAR - False Alarm Rate
- FFT - Fast Fourier Transform
- FH - Frequency Hough
- GFH - Generalized Frequency Hough
- GFH-v2 - Generalized Frequency Hough Version 2
- GPU - Graphics Processing Unit
- GR - General Relativity

- GRB - Gamma-Ray Burst
- GW - Gravitational Wave
- H1 - LIGO Hanford Detector
- KAGRA - Kamioka Gravitational Wave Detector
- L1 - LIGO Livingston Detector
- LIGO - Laser Interferometer Gravitational-wave Observatory
- LVK - LIGO-Virgo-KAGRA Collaboration
- MJD - Modified Julian Date
- NS - Neutron Star
- NUV - Near-Ultraviolet
- O4a - First Part of the Fourth Observing Run
- PSD - Power Spectral Density
- RA - Right Ascension
- SBO - Shock Breakout
- SFT - Short Fourier Transform
- SFDB - Short Fourier Transform Database
- SGR - Soft Gamma Repeater
- SN - Supernova
- SNR - Signal-to-Noise Ratio
- tCW - Long-Transient Gravitational Wave
- TT - Transverse-Traceless
- UL - Upper Limit
- UV - Ultraviolet
- Virgo - Virgo Gravitational-wave Detector
- ZTF - Zwicky Transient Facility

Chapter 1

Introduction

For as long as we have looked at the night sky, we have tried to understand what lies beyond our world. Over time, our picture of the Universe has grown step by step, driven by new ideas and better instruments. Almost everything we know about the cosmos has come from one source: light.

But light does not always tell the full story. Some of the most extreme events in the Universe happen in places where electromagnetic radiation is weak. To completely understand these systems, we need a different kind of messenger.

Gravitational waves provide exactly that. First predicted by Albert Einstein in 1916, they represent tiny distortions in spacetime that travel across the Universe carrying information about their sources. For decades they remained completely theoretical, until their first direct detection in 2015 by the LIGO detectors. That discovery opened a completely new way of observing the Universe.

Today, gravitational-wave astronomy allows us to study objects that cannot be fully understood through light alone. Among the most interesting of these are compact objects such as neutron stars. These are remnants of massive stars that have collapsed into some of the densest forms of matter known. To give an idea, a neutron star packs more mass than the Sun into a sphere with a diameter only about 20 km. Their internal structure reaches densities far beyond anything that can be reproduced on Earth.

Some neutron stars, known as magnetars, go even further. They have inferred surface dipolar magnetic fields that can reach about 10^{14}-10^{15} G, far stronger than those of typical astrophysical objects and many orders of magnitude beyond magnetic fields achievable in laboratories. Their internal magnetic fields may be even stronger and can induce significant deformations of the stellar structure. When such an object is born, it can rotate extremely rapidly and store enormous amounts of rotational energy. This energy can power GW emission through small asymmetries in the star's shape or internal motion. Detecting such signals would open a direct window into the physics of newborn magnetars, including their magnetic structure, deformation, and early evolution. However, these signals are expected to be weak and uncertain in form, which makes their detection a challenging data analysis problem.

This thesis focuses on developing and applying methods to search for gravitational waves from newborn magnetars. It combines gravitational-wave data analysis with information from electromagnetic observations in a multi-messenger framework, in order to improve our chances of detecting and understanding these extreme systems.

1.1 Motivation

Gravitational waves (GWs) are propagating perturbations of spacetime generated by the accelerated motion of mass distributions with a time-varying quadrupole moment. Their existence was first predicted by Einstein in 1916 as a consequence of General Relativity [1]. For many decades gravitational waves remained an indirect prediction of the theory, as their extremely small amplitudes made direct detection challenging. The first strong indirect evidence for their existence came in 1974 with the discovery of the binary pulsar PSR B1913+16 by Hulse and Taylor [2]. Measurements of the gradual decrease in the orbital period of the system were found to be in good agreement with the energy loss expected from gravitational-wave emission, providing indirect confirmation of Einstein's prediction. Direct detection was finally achieved in 2015 when the Advanced LIGO detectors observed gravitational waves from the binary black hole merger GW150914 [3]. This discovery marked the beginning of gravitational-wave astronomy and opened a new observational window onto the Universe.

Since the first detection, numerous gravitational-wave events have been observed by the global network of interferometric detectors which includes the LIGO, Virgo and KAGRA detectors [4–7]. To date, all confirmed detections are consistent with compact binary coalescences (CBCs) involving black holes and neutron stars [8–12]. Notable detections include GW170814, the first event observed by all three detectors (the two LIGO detectors and Virgo), which significantly improved sky localisation. GW170817, a binary neutron star merger which is also associated with electromagnetic counterparts, marked the beginning of multimessenger astronomy [13, 14]. These observations have provided important insights into the population of compact objects, the physics of strong gravitational fields, and the astrophysical processes governing stellar evolution, as summarised in the latest gravitational-wave transient catalog GWTC-5.0 [12].

Beyond compact binary mergers, gravitational-wave detectors are also sensitive to other classes of signals, which remain undetected to date, including those produced by isolated compact objects. In particular, neutron stars represent promising sources of long-lasting gravitational-wave emission [15–17]. These extremely dense stellar remnants can emit gravitational radiation through several mechanisms, including non-axisymmetric deformations, oscillation modes, and hydrodynamic or magnetic instabilities [15–17]. Among neutron stars, magnetars, which have inferred surface dipolar magnetic fields reaching 10^{14}-10^{15} G [18], are of particular interest. Newly born magnetars formed in core-collapse supernovae or in the remnants of compact binary mergers are expected to rotate rapidly and possess large amounts of rotational energy. If the star develops a non-axisymmetric deformation, part of this rotational energy can be emitted in the form of gravitational waves as the star spins down. In such scenarios the gravitational-wave frequency evolves over time as the star loses angular momentum through electromagnetic and gravitational radiation. The resulting signals, commonly referred to as long-transient gravitational waves (tCWs) [19], correspond to intermediate duration emission, ranging from seconds to days depending on the source and emission mechanism [20–24].

The detection of such signals would provide valuable information about the internal physics of magnetars, including their equation of state, magnetic field configuration, and early rotational evolution [25, 26]. However, searching for long-transient gravitational waves is challenging due to their weak amplitude and the large parameter space associated with their frequency evolution. Dedicated data analysis methods are therefore required to efficiently search for these signals in detector data.

This thesis focuses on the search for long-transient gravitational-wave signals from newly born magnetars, combining gravitational-wave data analysis techniques with information from electromagnetic observations in a multi-messenger framework.

1.2 Long-transient gravitational waves from newborn magnetars

Long-transient gravitational waves constitute an intermediate class of signals between short transient signals from CBCs and long-lived, nearly monochromatic continuous waves (CWs). Continuous waves are signals persisting over timescales much longer than the typical duration of observation runs [16]. Long-transient gravitational waves are a special subclass of continuous waves, typically associated with sources whose emission lasts for finite periods, during which the gravitational-wave frequency can evolve significantly as the source loses rotational energy. In this work, the models and parameter spaces considered cover signal durations ranging from hours to days.

Newborn magnetars produced in core-collapse supernovae are expected to rotate rapidly at birth, potentially with millisecond periods [18, 27]. If the star possesses strong internal magnetic fields, as in the case of magnetars, magnetic stresses may induce non-axisymmetric deformations of the stellar interior. Such deformations can generate gravitational radiation.

The gravitational-wave strain amplitude emitted by a rotating neutron star depends on the ellipticity, moment of inertia, and rotation frequency [28]. As the star spins down, the gravitational-wave frequency evolves according to a power-law relation governed by the braking index, which depends on the dominant spin-down mechanism [29]. For example, electromagnetic dipole radiation produces a braking index $n = 3$, while gravitational-wave dominated spin-down corresponds to $n = 5$. The gravitational-wave strain amplitude measured at the detector is also inversely proportional to the distance to the source. These different regimes lead to characteristic trajectories of the signal in the time-frequency plane.

Because the relevant source parameters- such as the initial rotation frequency, ellipticity, and the signal start time - are generally unknown, searches must explore a large parameter space. Fully coherent searches over such a parameter space are not computationally feasible. Semi-coherent methods therefore provide an efficient alternative. These approaches combine coherent analyses of short data segments with incoherent combinations across longer timescales, allowing searches for weak signals with evolving frequency [28, 30].

One of the most powerful techniques for this purpose is the Frequency Hough (FH) transform [31], which maps peaks in the time-frequency plane to candidate signal parameters. A generalisation of this method, the Generalized Frequency Hough (GFH) transform [32], extends the approach to more general power-law frequency evolutions and has already been applied in searches for long-transient signals, including the post-merger remnant associated with GW170817 [33]. In this work, we use an advanced implementation of the GFH method, referred to as GFH-v2 [34], which incorporates several improvements with respect to the original implementation. In particular, GFH-v2 includes enhanced parameter-space coverage and improved computational efficiency, enabling more sensitive searches for long-transient signals from newborn magnetars.

1.3 Multi-messenger astronomy

The study of astrophysical phenomena increasingly relies on the combination of different observational channels. This approach, known as multi-messenger astronomy, combines information from gravitational waves, electromagnetic radiation, neutrinos, and cosmic rays in order to obtain a more complete picture of energetic astrophysical events.

The potential of this approach was clearly demonstrated in 2017 with the detection of the binary neutron star merger GW170817 and its associated electromagnetic counterparts [13, 14]. This sequence of observations is illustrated in Fig. 1.1. Observations across the electromagnetic spectrum revealed a short gamma-ray burst and

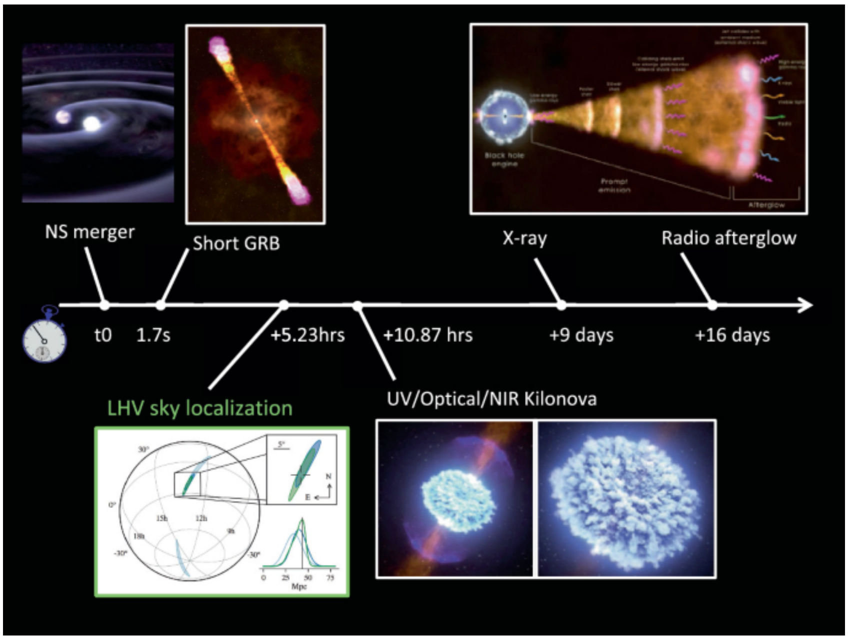

Figure 1.1. Timeline of the multi-messenger observations associated with the binary neutron star merger GW170817. The sequence includes the gravitational-wave detection, the prompt gamma-ray burst (GRB 170817A), the rapid release of the gravitational-wave sky localization, and the subsequent electromagnetic counterparts across the spectrum, including the optical kilonova (AT 2017gfo), followed by X-ray and radio emission from the relativistic jet. Adapted from [35].

a kilonova powered by the radioactive decay of heavy elements synthesized in the merger ejecta [36, 37]. This event established a direct connection between neutron star mergers, short gamma-ray bursts, and heavy element nucleosynthesis.

Multi-messenger observations are also particularly relevant for the study of newly formed magnetars. In the case of core-collapse supernovae, electromagnetic signals such as shock breakout (SBO) emission can provide precise information about the time and location of the explosion [38]. This information can significantly reduce the parameter space that must be explored in gravitational-wave searches.

Recent studies suggest that ultraviolet observations of supernova shock breakout can provide valuable constraints on the formation of rapidly rotating magnetars [38–41]. Future space-based ultraviolet missions, such as ULTRASAT, are expected to detect large numbers of shock breakout events from nearby supernovae [42]. Such observations can serve as triggers for directed searches for long-transient gravitational waves associated with newborn magnetars, significantly enhancing the prospects for multi-messenger detections.

1.4 Outline of the thesis

This thesis investigates the search for long-transient gravitational waves from newborn magnetars using advanced data analysis methods and multi-messenger observations.

Chapter 2 introduces the theoretical framework of gravitational waves and the principles of interferometric detection. The chapter covers the basic equations of gravitational radiation, different classes of gravitational-wave signals, the operating principles of ground-based detectors, and the main sources of detector noise and sensitivity limitations.

Chapter 3 provides an overview of neutron stars and magnetars, discussing their formation, internal structure, equation of state, rotation, and magnetic fields. Particular attention is given to magnetars as potential sources of gravitational waves, including the physical mechanisms that can generate non-axisymmetric deformations and long-lived gravitational-wave emission.

Chapter 4 focuses on long-transient gravitational-wave signals, presenting the main signal models used in this work. In particular, the frequency evolution, strain amplitude evolution, and relevant physical parameters are described.

Chapter 5 discusses electromagnetic counterparts associated with newborn magnetars, with emphasis on magnetar-driven supernova emission and ultraviolet observations in the ULTRASAT band. Expected event rates and detection horizons are also presented. The work presented in this chapter is based on a published paper in which the author is first author [38].

Chapter 6 describes the search methods used for long-transient gravitational waves. It introduces semi-coherent search techniques, the construction of peakmaps from detector data, the Frequency Hough transform, and the Generalized Frequency Hough method. The chapter also presents the candidate-selection procedure, coincidence analysis, follow-up strategy, and theoretical sensitivity estimation

Chapter 7 presents the development and validation of the GFH-v2 pipeline. The optimized parameter-space selection, algorithmic improvements, and analysis setup are described. The performance of the pipeline is evaluated through simulated signal injections into LIGO O4a data, and theoretical and empirical sensitivity estimates are compared. The work presented in this chapter is based on a paper published in Physical Review D, in which the author is first author [34].

Chapter 8 presents a directed search for long-transient gravitational-wave emission from the possible magnetar remnant of the nearby supernova SN2023ixf using data from LIGO Engineering Run 15. The chapter describes the search configuration, candidate-selection procedure, follow-up analysis, and upper-limit estimation. This work is based on a manuscript in preparation, to be submitted to Physical Review D, in which the author is first author.

Finally, Chapter 9 presents the discussion and conclusions of this work. It brings together the main results, their interpretation, and a summary of the overall findings, followed by a discussion of the multi-messenger perspective, future developments, and final conclusions.

Chapter 2

Gravitational Waves and Detection

Gravitational waves are small perturbations of space-time that propagate as waves at the speed of light. They are a direct prediction of Einstein's theory of General Relativity, where gravity is described not as a force but as the consequence of the curvature of space-time caused by matter and energy [1, 43, 44].

This chapter follows the standard treatment given in [44], focusing on the aspects most relevant for gravitational-wave detection and data analysis. It introduces the basic concepts needed to describe gravitational waves and their detection. Section 2.1 develops the theoretical framework in linearized General Relativity, including plane-wave solutions and the quadrupole description of gravitational radiation. Section 2.2 provides an overview of the main classes of gravitational-wave signals expected from astrophysical sources. Section 2.3 describes the principle of ground-based laser interferometers and their response to an incoming gravitational-wave signal. Finally, Section 2.4 summarizes the main noise sources that limit detector sensitivity.

2.1 Gravitational-wave fundamentals

2.1.1 Einstein field equations and space-time curvature

In General Relativity the geometry of space-time is described by the metric tensor $g_{\mu\nu}$, where the Greek indices $\mu, \nu = 0, 1, 2, 3$ label the space-time coordinates, with 0 denoting the time coordinate and $1, 2, 3$ the spatial coordinates. In the absence of gravity, space-time is flat and the metric reduces to the Minkowski metric, $\eta_{\mu\nu} = \mathrm{diag}(-1, 1, 1, 1)$. When matter or energy is present, the metric deviates from this flat form, and these deviations describe the gravitational field.

The relation between the space-time geometry and the matter content is given by the Einstein field equations (EFEs),

$$R_{\mu\nu} - \frac{1}{2} g_{\mu\nu} R = \frac{8\pi G}{c^4} T_{\mu\nu}. \tag{2.1}$$

Here, G is the gravitational constant, c is the speed of light, and $T_{\mu\nu}$ is the stress-energy tensor, which specifies the density and flux of energy and momentum. The quantities $R_{\mu\nu}$ and R describe the curvature of space-time, where $R_{\mu\nu}$ is the Ricci tensor and R is the Ricci scalar.

Eq. 2.1 is often summarized by the statement: matter tells space-time how to curve, and curved space-time tells matter how to move. This idea forms the foundation of General Relativity.

The Einstein equations consist of ten coupled, non-linear partial differential equations for the ten independent components of the symmetric metric tensor $g_{\mu\nu}$.

Exact analytical solutions exist only for systems with a high degree of symmetry. Important examples include the Schwarzschild solution, which describes the space-time around a non-rotating spherical mass, and the Kerr solution, which describes a rotating black hole. In many astrophysical situations, including those relevant to this thesis, the gravitational field is weak in the region far from the source. In this regime the curvature is small, and the space-time metric can be written as the Minkowski metric plus a small perturbation. Linearizing the Einstein equations under this approximation leads to a set of wave equations. Their solutions describe perturbations that propagate at the speed of light. These perturbations are gravitational waves.

This weak-field approximation is sufficient to describe the gravitational radiation emitted by distant compact objects, such as the newly born magnetars considered in this thesis, and provides the basis for the discussion in the following sections.

2.1.2 Linearized gravity and wave equation

As discussed in the previous subsection, in regions very far from the source the gravitational field is weak and the space-time metric can be written as a small perturbation of the Minkowski metric,

$$g_{\mu\nu} = \eta_{\mu\nu} + h_{\mu\nu}, \tag{2.2}$$

where $|h_{\mu\nu}| \ll 1$. The tensor $h_{\mu\nu}$ represents a small deviation from flat space-time and contains the gravitational-wave signal.

Substituting this equation into the Einstein field equations (2.1) and retaining only terms linear in $h_{\mu\nu}$ gives the linearized Einstein equations. This approximation is valid when the gravitational field is weak and it can describe gravitational waves observed far from their source.

It is convenient to define the trace-reversed perturbation,

$$\bar{h}_{\mu\nu} = h_{\mu\nu} - \frac{1}{2}\eta_{\mu\nu} h, \tag{2.3}$$

where $h = h^{\alpha}{}_{\alpha}$ is the trace of the perturbation tensor.

The equations can be simplified further by imposing the Lorenz gauge condition,

$$\partial^{\mu}\bar{h}_{\mu\nu} = 0. \tag{2.4}$$

Applying this condition, the Einstein equations can be written as,

$$\Box\bar{h}_{\mu\nu} = -\frac{16\pi G}{c^4} T_{\mu\nu}, \tag{2.5}$$

where

$$\Box = -\frac{1}{c^2}\frac{\partial^2}{\partial t^2} + \nabla^2 \tag{2.6}$$

is the d'Alembert operator.

Eq. 2.5 has the same form as a standard wave equation, with the stress-energy tensor $T_{\mu\nu}$ acting as the source term. This shows that time-varying mass-energy distributions can generate perturbations that propagate through space-time.

In the vacuum region far from the source, where $T_{\mu\nu} = 0$, Eq. 2.5 reduces to

$$\Box\bar{h}_{\mu\nu} = 0. \tag{2.7}$$

The solutions of this equation are waves that travel at the speed of light. These propagating metric perturbations are gravitational waves.

2.1.3 Plane-wave solutions and Transverse-Traceless gauge

Since Eq. 2.7 is a linear wave equation, its solutions can be expressed as plane waves. A general plane wave solution can be written as

$$\bar{h}_{\mu\nu}(x) = A_{\mu\nu}e^{ik_\alpha x^\alpha}, \tag{2.8}$$

where $A_{\mu\nu}$ is a symmetric tensor called the polarization tensor, and k_α is the wave four-vector.

Substituting this into the vacuum wave Eq. 2.7 leads to the condition

$$k_\alpha k^\alpha = 0, \tag{2.9}$$

which shows that the wave vector is null. This implies that gravitational waves propagate at the speed of light.

The Lorenz gauge condition, introduced in the previous section, further imposes a constraint on the amplitude,

$$k^\mu\bar{h}_{\mu\nu} = 0. \tag{2.10}$$

This condition shows that the perturbation is transverse, meaning that its oscillations are orthogonal to the direction of propagation.

Even after imposing the Lorenz gauge, the metric perturbation still contains non-physical components due to residual gauge freedom. To isolate the physical content of the field, it is convenient to adopt the transverse-traceless (TT) gauge, in which the metric perturbation satisfies

$$h^{0\mu} = 0, \qquad h^i_i = 0, \qquad \partial^i h_{ij} = 0. \tag{2.11}$$

In this gauge, only the physical degrees of freedom remain. In particular, gravitational waves in general relativity have two independent polarization states, commonly denoted h_+ and $h_\times$. These correspond to the two propagating degrees of freedom of linearized gravitational waves in vacuum.

2.1.4 Effect of gravitational waves on test masses

The physical meaning of GWs can be understood by studying their effect on freely falling test masses. In General Relativity, freely falling particles move along geodesics,

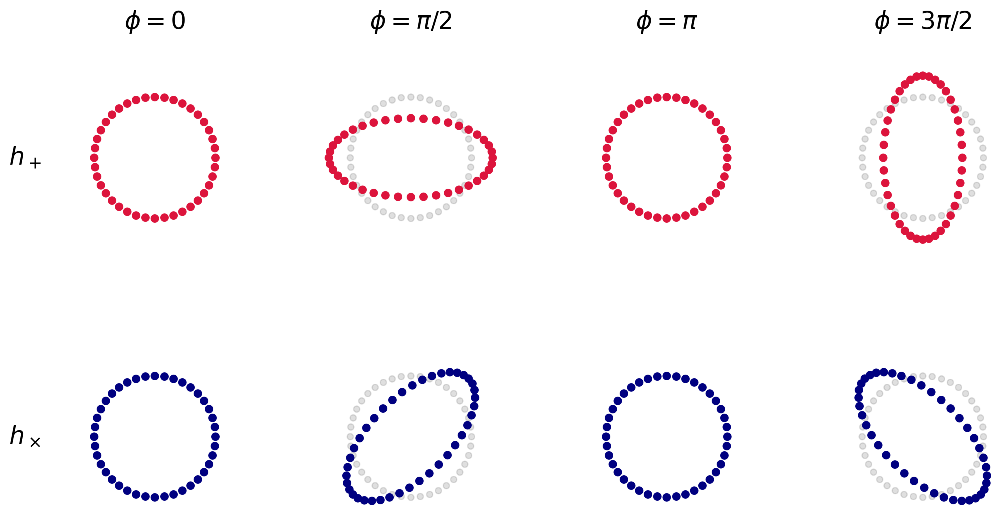

Figure 2.1. Effect of h_+ and $h_\times$ polarizations on a ring of freely falling test masses. The wave propagates perpendicular to the plane of the ring.

and the relative motion between nearby geodesics is described by the geodesic deviation equation,

$$\frac{D^2\xi^\mu}{d\tau^2} = -R^\mu{}_{\nu\rho\sigma}\,\xi^\rho u^\nu u^\sigma, \tag{2.12}$$

where ξ^μ is the separation vector between two neighbouring geodesics, u^μ is the four-velocity of the reference particle, and $R^\mu{}_{\nu\rho\sigma}$ is the Riemann curvature tensor.

This equation shows that the relative acceleration of free particles is fully determined by space-time curvature. In the weak-field regime, gravitational waves produce a small, time-dependent curvature, which leads to oscillatory relative motion of test masses.

To explain this, we consider the proper detector frame of a local observer, where the test masses are initially at rest before the arrival of the wave. In this frame, the geodesic deviation equation becomes

$$\ddot{\xi}^i = -c^2 R^i{}_{0j0}\,\xi^j, \tag{2.13}$$

where the dot denotes derivatives with respect to coordinate time t.

At this point it is convenient to use the linearized theory explained in the previous subsections. Since GWs are treated as small perturbations around flat space-time, the Riemann tensor is already of first order in the metric perturbation $h_{\mu\nu}$. Therefore, it is sufficient to compute $R^i{}_{0j0}$ within linearized gravity, where it takes a particularly simple form in the transverse-traceless (TT) gauge.

In the TT gauge, and in the proper detector frame, the relevant components of the Riemann tensor are

$$R_{i0j0} = -\frac{1}{2c^2}\,\ddot{h}^{\mathrm{TT}}_{ij}. \tag{2.14}$$

Substituting this result into the geodesic deviation equation gives

$$\ddot{\xi}^i = \frac{1}{2}\,\ddot{h}^{\mathrm{TT}}_{ij}\,\xi^j. \tag{2.15}$$

For a slowly moving test mass configuration, this equation can be integrated to obtain the fractional change in proper distance between two masses,

$$\frac{\Delta L(t)}{L} = \frac{1}{2} h_{ij}^{\mathrm{TT}}(t). \tag{2.16}$$

This result shows that gravitational waves directly produce oscillatory changes in the proper distance between freely falling test masses. A standard illustration is a ring of test particles in the plane perpendicular to the propagation direction. A h_+ polarization stretches the ring along one axis while compressing it along the perpendicular axis, while the $h_\times$ polarization produces the same effect rotated by 45°. This is shown schematically in Fig. 2.1.

This is the basis for all laser interferometer detectors, where the change in proper distance between suspended test masses is measured using phase shift of laser light, as discussed in the next sections.

2.1.5 Retarded solution and far-zone approximation

In the previous section, gravitational waves were introduced as solutions of the linearized Einstein equations. In the presence of matter and energy, the metric perturbation satisfies

$$\Box \bar{h}_{\mu\nu} = -\frac{16\pi G}{c^4} T_{\mu\nu}, \tag{2.17}$$

where $T_{\mu\nu}$ is the stress-energy tensor of the source.

Eq. 2.17 has the form of a wave equation with a source term. Its solution can be obtained using the retarded Green's function of the d'Alembert operator. In flat space-time, the retarded solution is

$$\bar{h}_{\mu\nu}(t, \mathbf{x}) = \frac{4G}{c^4} \int \frac{T_{\mu\nu}(t_r, \mathbf{x}')}{|\mathbf{x} - \mathbf{x}'|} \, d^3x', \tag{2.18}$$

where

$$t_r = t - \frac{|\mathbf{x} - \mathbf{x}'|}{c} \tag{2.19}$$

is the retarded time.

For the astrophysical sources we are considering, the detector is located very far from the source. If the typical radius of the source is d and the observer is at distance r, then

$$r \gg d. \tag{2.20}$$

In this region, the denominator in Eq. 2.18 can be approximated as

$$|\mathbf{x} - \mathbf{x}'| \simeq r, \tag{2.21}$$

and the retarded time becomes

$$t_r \simeq t - \frac{r}{c}. \tag{2.22}$$

Under these approximations, the solution can be expanded in multipoles.

2.1.6 Multipole expansion and quadrupole radiation

For sources moving slowly compared to the speed of light ($v \ll c$), the dominant contribution to gravitational radiation comes from the mass quadrupole moment of the system. The monopole term does not contribute because the total mass of an isolated system is conserved, while the dipole term also does not contribute because of conservation of linear momentum.

Keeping only the leading-order radiative term, the gravitational-wave field in the far zone can be written in the transverse-traceless gauge as

$$h_{ij}^{\mathrm{TT}}(t, \mathbf{x}) = \frac{1}{r} \frac{2G}{c^4} \ddot{Q}_{ij}^{\mathrm{TT}} \left(t - \frac{r}{c} \right), \tag{2.23}$$

where Q_{ij} is the mass quadrupole moment tensor,

$$Q_{ij}(t) = \int d^3x \, \rho(t, \mathbf{x}) \left(x_i x_j - \frac{1}{3} r^2 \delta_{ij} \right). \tag{2.24}$$

Here $\rho(t, \mathbf{x})$ is the mass density of the source.

Eq. 2.23 is known as the quadrupole formula. It shows that gravitational waves are generated by the second time derivative of the quadrupole moment. Therefore, gravitational radiation is produced only by accelerated non-spherical mass distributions with a time-dependent quadrupole moment.

In practice, different astrophysical systems realise this condition in very different ways. Compact binary systems produce rapidly evolving, short-duration signals, while transient explosive events generate short bursts with poorly modelled waveforms. In contrast, isolated rotating neutron stars produce long-lasting signals where the quadrupole deformation evolves slowly in time.

These differences in duration, frequency evolution, and waveforms lead to a classification of gravitational-wave signals into distinct observational categories.

2.2 Classes of gravitational-wave signals

Eq. 2.23 shows that gravitational waves are produced by the second time derivative of the mass quadrupole moment. This means that gravitational waves are emitted only when a source has a time-varying, non-spherical motion. A perfectly spherical motion does not produce gravitational radiation.

Different astrophysical systems produce gravitational waves with different durations, frequency behaviour, and signal shapes. For this reason, gravitational-wave signals are usually classified into four main groups based on how long they last, or equivalently how long their signal is observable within the detector's sensitive frequency band, how their frequency changes in time, and how well their waveform can be modelled. These four classes are compact binary coalescences, burst signals, stochastic backgrounds and continuous waves (including long transients).

2.2.1 Compact binary coalescences

Compact binary coalescences are systems composed of two compact objects in a bound orbit, such as binary neutron stars, binary black holes, or neutron star-black hole binaries. As the system evolves, it loses energy through gravitational-wave emission, causing the two objects to slowly spiral towards each other until they eventually merge.

CBC signals are well-modelled GW sources as their evolution can be accurately described using post-Newtonian (PN) theory during the early stages and numerical relativity (NR) near merger. This accurate waveform modelling enables CBC searches to use matched-filtering techniques, in which the detector data are compared against banks of theoretical waveform templates.

The gravitational-wave emission from a CBC is commonly divided into three stages: inspiral, merger, and ringdown.

Inspiral: During the inspiral phase, the two compact objects orbit each other with increasing speed while losing orbital energy. As a result, both the amplitude and the frequency of the emitted gravitational waves increase with time, producing the

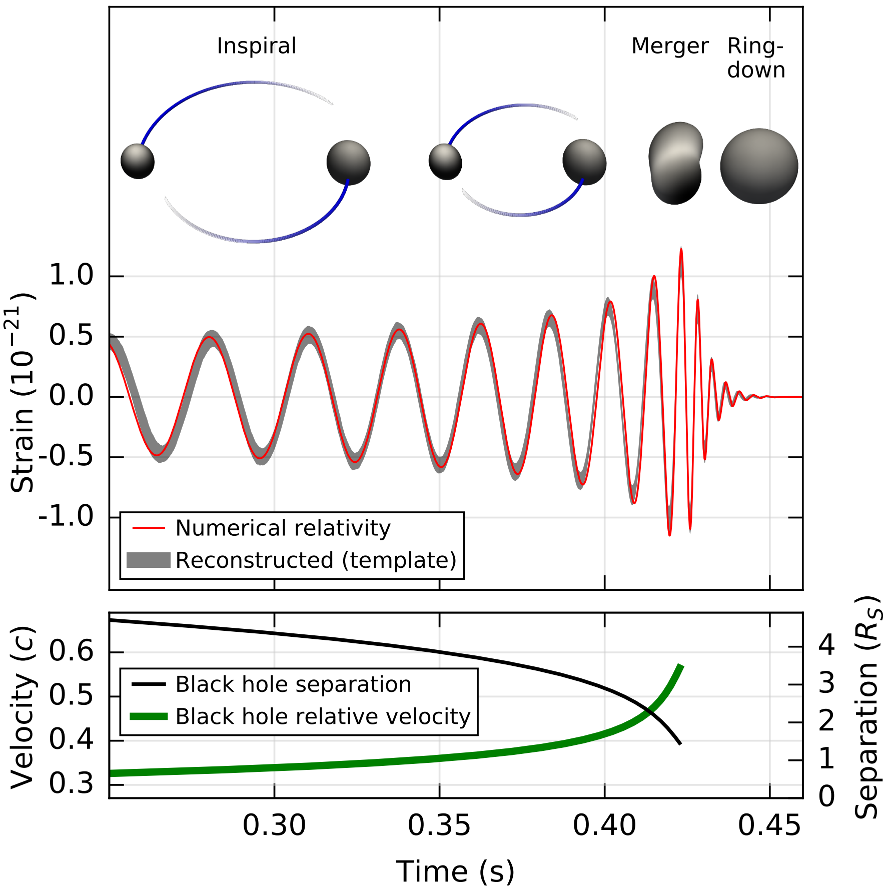

Figure 2.2. Gravitational-wave signal from the binary black hole merger GW150914, illustrating the inspiral, merger, and ringdown phases of a compact binary coalescence. The increasing amplitude and frequency produce the characteristic 'chirp' waveform. Figure adapted from Abbott *et al.* [3].

characteristic 'chirp' waveform. The evolution of the signal is mainly determined by the chirp mass,

$$\mathcal{M}_c = \frac{(m_1 m_2)^{3/5}}{(m_1 + m_2)^{1/5}}, \tag{2.25}$$

where m_1 and m_2 are the component masses of the binary system. The chirp mass controls how rapidly the orbital frequency evolves during the inspiral. More massive systems inspiral and merge more quickly, producing shorter signals at lower frequencies, while less massive systems lose energy more slowly, their inspiral phase takes much longer.

Merger: When the orbital separation becomes very small, strong-field relativistic effects dominate and the two bodies merge into a single compact object. During this stage, the post-Newtonian approximation breaks down and the system enters a highly non-linear regime that must be described using numerical relativity. The merger phase produces the peak gravitational-wave amplitude.

Ringdown: After the merger, the final remnant object settles into a stable configuration through the emission of damped oscillations known as quasi-normal modes.

Because CBC waveforms are highly predictable, they can be modelled using several template waveforms parameterised by the component masses and spins. This enables coherent matched-filter searches, which currently is the most sensitive method for detecting gravitational waves from compact binaries.

A schematic representation of the characteristic 'chirp' waveform is shown in Fig. 2.2, illustrating the increase in frequency and amplitude during inspiral, followed by merger and ringdown.

2.2.2 Burst signals

Burst gravitational waves are short-duration transient signals produced by violent astrophysical events. Unlike CBCs, burst signals are often difficult to model accurately because the physical processes generating them may be highly complex and not fully understood [45–47].

Possible burst sources include core-collapse supernovae, magnetar flares, and other transient phenomena [47]. These events can produce gravitational-wave emission over timescales ranging from a few milliseconds to several seconds.

Since the waveforms are not precisely known, searches for these signals generally rely on methods that identify excess power in the time-frequency plane [48] rather than matched filtering. These techniques look for transient features in the detector data without assuming a specific waveform model [49].

2.2.3 Stochastic gravitational-wave background

The stochastic gravitational-wave background (SGWB) is formed by the superposition of many different gravitational-wave sources [50, 51]. The signals from these sources overlap in time and cannot be distinguished separately. The resulting signal appears as a persistent random background of gravitational radiation.

SGWB is generally divided into two main categories based on its origins: astrophysical [52] and cosmological [53]. Astrophysical contributions can arise from the combined emission of many distant compact binary mergers, rotating neutron stars, or supernovae. Cosmological backgrounds may originate from physical processes in the early Universe, such as inflation, cosmic strings, or phase transitions shortly after the Big Bang.

Since the SGWB is expected to be very weak compared to detector noise, searches typically rely on cross-correlating data from multiple detectors. A correlated signal between geographically separated detectors may indicate the presence of a stochastic gravitational-wave background.

2.2.4 Continuous gravitational waves

Continuous gravitational waves (CWs) are long-lasting signals produced by rotating compact objects that are not perfectly symmetric, most commonly neutron stars [15–17]. In the simplest case, these signals are almost monochromatic and their phase changes slowly enough that they last over long observation times.

For a rigid star rotating around a principal axis with a fixed ellipticity, the gravitational-wave emission happens mainly at twice the rotation frequency,

$$f_{\mathrm{gw}} = 2 f_{\mathrm{rot}} = \frac{\Omega}{\pi}. \tag{2.26}$$

In this case, the strain amplitude is given by [54]

$$h_0(t) = \frac{4\pi^2 G}{c^4} \frac{I\epsilon}{d} f_{\mathrm{gw}}^2(t), \tag{2.27}$$

where I is the moment of inertia, ϵ is the ellipticity of the star, and d is the distance to the source.

In the standard picture of continuous waves, it is assumed that the star's shape and rotation change very slowly. Because of this, the signal stays almost monochromatic over the time span of observations. But there are special cases where the spin-down is much faster. In particular, newly born neutron stars can spin down quite quickly. In such cases, both the frequency and amplitude of the signal change noticeably with time.

This leads to a broader class of signals called long-transient gravitational waves (tCWs) [15, 16, 55]. These are still based on the same physical mechanism as continuous waves, but they last only for a limited time, typically from hours to days, and show clear evolution in both frequency and amplitude. Long-transient signals are expected, for example, from newborn magnetars: rapidly rotating, highly magnetized neutron stars formed in events such as core-collapse supernovae or binary neutron star mergers. In these systems, gravitational-wave emission can arise from non-axisymmetric deformations, strong internal magnetic fields, or dynamical instabilities, leading to a rapidly evolving signal.

In this thesis, we focus on these long-transient gravitational waves. The specific case of newborn magnetars as long-transient GW sources is discussed in detail in Chapter 3, while the signal model used in the analysis is presented in Chapter 4.

The gravitational-wave signals discussed so far produce extremely small distortions of space-time by the time they reach the Earth. Detecting these signals requires highly sensitive detectors capable of measuring tiny relative changes in length. The operating principles and sensitivity of modern gravitational-wave detectors are discussed in the following section.

2.3 Gravitational-wave detectors

Although Einstein predicted gravitational waves in 1916, the experimental search did not start right away. For nearly fifty years, the technology to measure such tiny signals did not exist. This changed in the 1960s when Joseph Weber built the first resonant bar detectors, famously known as Weber bars [56]. These detectors consisted of large metallic cylinders designed to vibrate when a gravitational wave passed through them. Although they were not sensitive enough to make confirmed detections, they marked the beginning of experimental gravitational-wave research.

Over time, laser interferometry emerged as a promising method for gravitational-wave detection because of its much higher sensitivity. The basic concept was developed by several researchers during the 1970s and 1980s, driven by early proposals from Rainer Weiss and Kip Thorne, alongside Ronald Drever and Heinz Billing, which led to the construction of large-scale interferometric detectors [7, 57] such as LIGO in the United States (led by Weiss, Thorne, and Barry Barish), Virgo in Italy (founded by Alain Brillet and Adalberto Giazotto), and later KAGRA in Japan (led by Takaaki Kajita).

A major breakthrough occurred on 14 September 2015, when the two Advanced LIGO detectors made the first direct detection of gravitational waves during the event GW150914 [3]. The signal originated from the merger of two black holes and provided the first direct confirmation of gravitational waves as predicted by general relativity. This discovery marked the beginning of gravitational-wave astronomy. Today, gravitational-wave observations are carried out using a global network of interferometric detectors.

2.3.1 Principle of interferometric detectors

Ground-based gravitational-wave detectors such as LIGO, Virgo, and KAGRA are based on the Michelson interferometer design. In its basic layout, an interferometer consists of a laser source, a beam splitter, two perpendicular arms of equal length, highly reflective mirrors, and a photodetector. A simplified schematic of such an interferometer is shown in Fig. 2.3.

In a simplified representation, a laser beam is split into two beams that travel along perpendicular arms. These beams are reflected by mirrors placed at the ends of the arms and then recombined at the beam splitter before reaching a photodetector. If the two arms have exactly the same length, the returning light waves interfere destructively and no light reaches the detector output. When a gravitational wave passes through the interferometer, it stretches one arm while compressing the other. This changes the relative distance travelled by the laser beams and produces a phase shift between them. As a result, the interference pattern changes at the output. By measuring this change, the gravitational-wave strain can be detected.

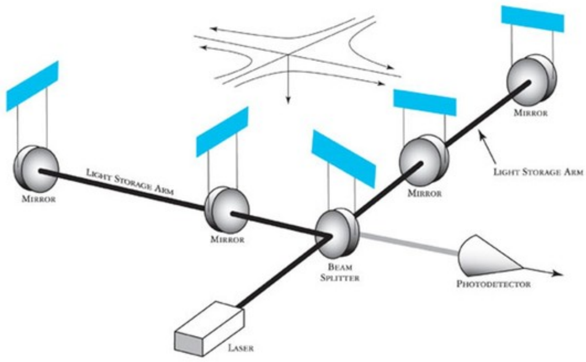

Figure 2.3. Basic schematic of a laser interferometric detector. A laser beam is split into two perpendicular arms, reflected by test masses, and recombined at the beam splitter. A passing gravitational wave changes the relative optical path lengths in the two arms, producing a measurable interference signal. Credit: Caltech/MIT/LIGO Lab.

The quantity measured by the detector is the strain,

$$h(t) = \frac{\Delta L(t)}{L}, \tag{2.28}$$

where L is the arm length and $\Delta L(t)$ is the differential change in the arm lengths caused by the gravitational wave.

For astrophysical sources, the strain reaching Earth is extremely small, corresponding to extremely small differential changes in the interferometer arm lengths and making their detection very challenging.

2.3.2 Sensitivity enhancement: Fabry-Perot cavities and recycling

To improve sensitivity, modern detectors use several optical techniques that increase the effective interaction time between the laser light and the gravitational wave.

The most important improvement is the use of Fabry-Perot cavities inside the arms. A Fabry-Perot cavity is basically a pair of highly reflective mirrors placed at the ends of each arm. Instead of the laser light passing through the arm just once, it bounces back and forth many times between these mirrors before returning to the beam splitter. Because of these repeated reflections, the light effectively travels a much longer distance inside the arm, which increases the phase shift produced by a passing gravitational wave.

Another important improvement is power recycling. A partially reflecting mirror is placed at the input of the interferometer. This reflects light that would otherwise escape back into the system, increasing the circulating laser power. This improves the sensitivity by reducing shot noise, which comes from statistical fluctuations in the detected photons.

A third technique is signal recycling. Here, an additional mirror is placed at the output (before the photodetector). This allows the detector response to be tuned in frequency, making it more sensitive in certain frequency ranges.

2.3.3 Ground-based detector network

Gravitational-wave observations are carried out using a network of interferometric detectors located around the world. Operating multiple detectors simultaneously is essential for confirming candidate signals and improving source localization on the sky.

LIGO: The Laser Interferometer Gravitational-wave Observatory (LIGO) consists of two detectors located in Livingston, Louisiana, and Hanford, Washington, in the United States [4]. Each detector has two perpendicular arms of length 4 km. The two LIGO detectors are separated by about 3000 km. A real GW signal is expected to appear in both detectors with a time delay of at most about 10, ms, consistent with propagation at the speed of light. The first direct detection of gravitational waves, GW150914, was made by the two Advanced LIGO detectors in September 2015.

Virgo: Virgo is a European gravitational-wave detector located near Pisa, Italy [58]. It has arm lengths of 3 km. Virgo joined observing runs with the LIGO detectors in 2017 and has significantly improved the ability of the detector network to localize sources on the sky.

KAGRA: KAGRA is located in the Kamioka mine in Japan and has arm lengths of 3 km [6]. It is the first large-scale gravitational-wave detector built underground and the first to use cryogenically cooled test masses. These features are designed to reduce seismic and thermal noise.

GEO600: GEO600 is a detector located near Hannover, Germany [59]. Although its arm length is only 600 m, much shorter than those of LIGO and Virgo, it has played an important role in the development and testing of advanced interferometric technologies.

LIGO-India: LIGO-India is an upcoming detector currently under construction in Hingoli, India [60]. It will use technology similar to the Advanced LIGO detectors and will significantly improve source localization by increasing the geographical separation between detectors.

2.3.4 Observing runs and gravitational-wave discoveries

The first gravitational-wave observing run (O1) was carried out between 2015 and 2016 using the two Advanced LIGO detectors [8, 61]. During this run, GW150914 was detected, marking the first direct observation of gravitational waves and the first observation of a binary black hole merger [3]. This discovery confirmed a major prediction of General Relativity.

The second observing run (O2) took place between 2016 and 2017 and included both LIGO detectors together with Virgo during the later part of the run [8, 61]. One of the most important discoveries of O2 was GW170817, the first binary

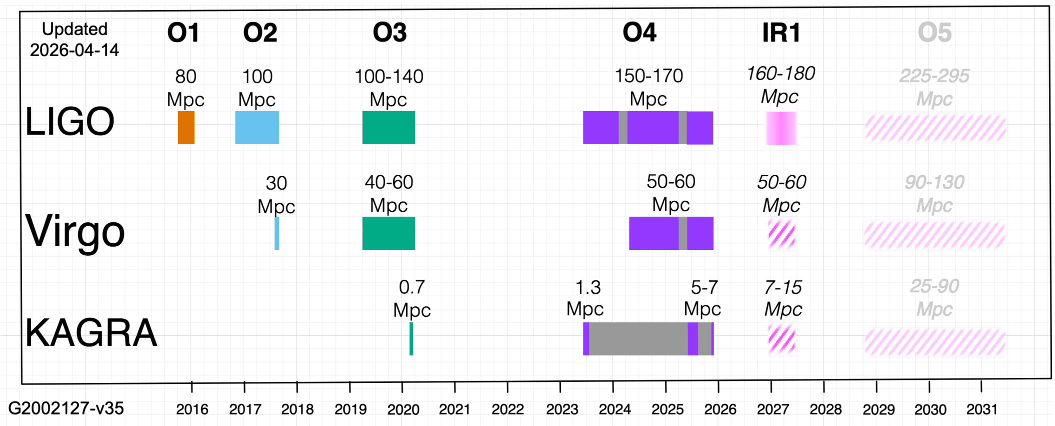

Figure 2.4. Timeline of the gravitational-wave observing runs and the participation of different detectors. The sensitivity of the detector network has improved progressively from O1 to the planned O5 run. Figure adapted from the LVK Observing Plan document [65].

neutron star merger detected through both gravitational waves and electromagnetic observations [13]. This event marked the beginning of multi-messenger astronomy.

The third observing run (O3), conducted between 2019 and 2020, increased the number of detected compact binary mergers. KAGRA joined the detector network during the final stage of O3 [9, 10, 62].

The fourth observing run (O4) began in 2023 and continued until 2025. It involved the Advanced LIGO detectors, with Virgo and KAGRA joining later after commissioning activities. O4 further increased the number of detected gravitational-wave events and expanded the growing catalogue of compact binary mergers [11, 12, 63, 64].

Following O4, the LIGO-Virgo-KAGRA collaboration is planning an intermediate observing period known as Intermediate Run 1 (IR1), during which the two LIGO detectors will observe and Virgo and KAGRA are expected to join as they are available.

The fifth observing run (O5) is planned to begin with improved detector sensitivities and is expected to further increase the detection rate. Future observing runs will also benefit from the addition of LIGO-India, which will improve sky localization and strengthen the global detector network.

The timeline of the observing runs and detector participation is shown in Fig. 2.4.

2.3.5 Next-generation and future detectors

Even though the current network of detectors has already made many discoveries, more sensitive instruments are planned for the future.

The Einstein Telescope (ET) [66] in Europe and Cosmic Explorer (CE) [67] in the United States are proposed third-generation ground-based detectors. These detectors will have much better sensitivity than the current ones. This improvement would allow the detection of gravitational-wave sources at much larger distances.

For the Einstein Telescope, two detector configurations are currently being studied. One is a triangular design consisting of three detectors with arm lengths of 10 km arranged at angles of 60°. The other is a configuration based on two L-shaped detectors with arm lengths of 15 km located at separate sites. Studies are currently being carried out to determine the final design [68]. In both cases, the detector is planned to be built underground in order to reduce seismic and environmental noise. ET will also use advanced technologies such as cryogenic mirrors and improved laser interferometry to achieve high sensitivity.

For the Cosmic Explorer, the current concept consists of two facilities, one with arm lengths of 40 km and a second with arm lengths of 20 km [69]. Like LIGO, CE uses a conventional L-shaped interferometer design, but its much longer arms will significantly increase the detector sensitivity. CE is expected to build on technologies developed for Advanced LIGO and its upgrades, ultimately achieving a sensitivity improvement of about an order of magnitude over current detectors.

Future observations will also explore much lower frequencies than ground-based detectors can reach. For this purpose, the Laser Interferometer Space Antenna (LISA) is being developed. LISA is a planned space-based gravitational-wave observatory led by the European Space Agency, with launch currently expected in the mid-2030s [70]. LISA will consist of three spacecraft arranged in an approximately equilateral triangular configuration with arm lengths of about 2.5×10^6 km. Unlike ground-based detectors, which are limited at low frequencies by seismic and environmental noise, LISA will operate in space and will be sensitive to gravitational waves in the frequency range from roughly 10^{-4} Hz to 1 Hz. Thus LISA will observe sources that cannot be detected from the ground, including mergers of supermassive black holes, extreme mass-ratio inspirals etc. Together with ground-based observatories, it will provide gravitational-wave observations across a much wider range of frequencies and source populations.

Several other future gravitational-wave observatories have also been proposed, including the space-based missions DECIGO [71] and TianQin [72], which aim to complement both LISA and ground-based detectors by improving coverage across different frequency ranges.

2.3.6 Detector response and antenna pattern

A gravitational-wave detector is not equally sensitive to signals coming from all directions in the sky. The measured signal depends on the position of the source, the polarization of the gravitational wave, and the orientation of the detector.

A gravitational wave has two independent polarization components, denoted by $h_+(t)$ and $h_\times(t)$ as discussed in Section 2.1. The strain measured by an interferometric detector is a linear combination of these two polarizations,

$$h(t) = F_+(t)h_+(t) + F_\times(t)h_\times(t), \tag{2.29}$$

where F_+ and $F_\times$ are the antenna pattern (or beam pattern) functions, which describe how sensitive the detector is to a signal coming from a given direction and polarization.

Their values depend on the source sky position, the polarization angle ψ, and the orientation of the detector on Earth.

For a ground-based interferometer, the antenna pattern functions can be written as [54]

$$F_+(t) = \sin\zeta\left[a(t)\cos 2\psi + b(t)\sin 2\psi\right], \tag{2.30}$$
$$F_\times(t) = \sin\zeta\left[b(t)\cos 2\psi - a(t)\sin 2\psi\right], \tag{2.31}$$

where ζ is the angle between the detector arms ($\zeta = 90°$ for LIGO, Virgo, and KAGRA), ψ is the polarization angle, and the functions $a(t)$ and $b(t)$ depend on the source location and detector geometry [54].

Because the Earth rotates, the orientation of a detector relative to a fixed astrophysical source changes continuously. As a result, F_+ and $F_\times$ vary with time with a period of one sidereal day, producing a characteristic amplitude modulation of the observed signal.

For continuous-wave signals from rotating neutron stars, the two gravitational-wave polarizations can be written as [44]

$$h_+(t) = h_0 \frac{1+\cos^2\iota}{2}\cos\Phi(t), \tag{2.32}$$
$$h_\times(t) = h_0\cos\iota\sin\Phi(t), \tag{2.33}$$

where h_0 is the intrinsic strain amplitude, ι is the inclination angle between the star's spin axis and the line of sight, and $\Phi(t)$ is the phase evolution of the signal. Combining these expressions gives the strain measured by the detector.

2.4 Detector noise and sensitivity limits

The detection of gravitational waves is very challenging due to the extremely small strain amplitudes produced by astrophysical sources by the time they reach Earth [44]. In ground-based detectors, the measured signal is thus always dominated by instrumental and environmental noises. As a result, the detector output consists of a possible gravitational-wave signal along with noise contributions from the instrument and its surroundings [44].

The detector output time series can be written as

$$s(t) = h(t) + n(t), \tag{2.34}$$

where $h(t)$ denotes the gravitational-wave signal and $n(t)$ represents the detector noise. To extract these weak astrophysical signals it is important to understand the statistical properties of $n(t)$ and how this noise affects the detectability of signals.

In gravitational-wave data analysis, the noise is commonly modeled as a stationary Gaussian random process [44]. Under this assumption, the noise is fully characterised in the frequency domain by its one-sided power spectral density (PSD), $S_n(f)$, defined through

$$\langle \tilde{n}(f)\tilde{n}^*(f')\rangle = \frac{1}{2}S_n(f)\,\delta(f-f'), \tag{2.35}$$

where $\tilde{n}(f)$ is the Fourier transform of $n(t)$ and angle brackets denote an ensemble average.

The function $S_n(f)$ describes how the noise is distributed as a function of frequency and has units of Hz^{-1}. Its square root, $\sqrt{S_n(f)}$, is commonly referred to as the amplitude spectral density (ASD). Sensitivity curves of ground-based interferometers are typically plotted in terms of this quantity, as it provides a measure of the characteristic noise amplitude as a function of frequency.

Equivalently, the noise spectral density can be defined in terms of the autocorrelation function

$$R(\tau) = \langle n(t+\tau)n(t)\rangle, \tag{2.36}$$

through the Wiener-Khintchin relation [44],

$$S_n(f) = 2\int_{-\infty}^{+\infty} d\tau\, R(\tau)\, e^{i2\pi f\tau}. \tag{2.37}$$

The noise $n(t)$ is not caused by a single effect, but is instead the result of many different contributions coming from both the detector itself and its surrounding environment. These different noise sources typically dominate in different frequency ranges.

We can group the main noise sources into a few broad categories. One important distinction is between optical read-out noise, which comes from the way the laser light is used to measure the motion of the mirrors, and displacement noise, which

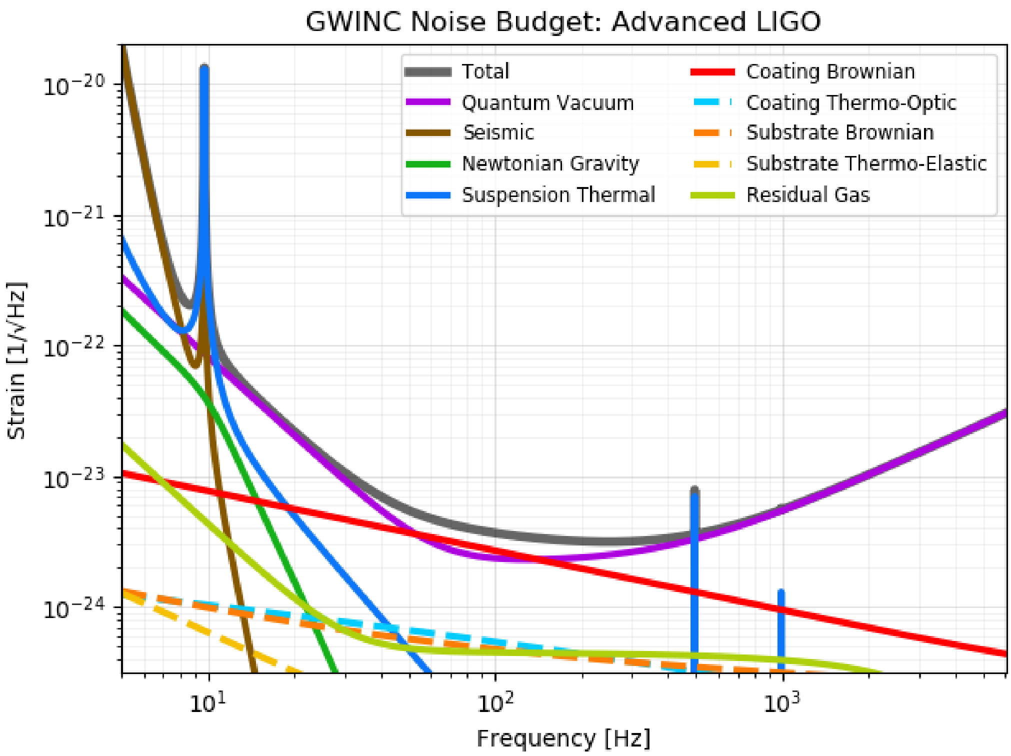

Figure 2.5. Noise budget of aLIGO generated using PyGWINC [73]. The plot shows the main noise contributions including quantum noise, seismic and Newtonian noise, and thermal noise sources.

is due to real physical motion of the test masses [44]. On top of these, there are also several technical and environmental noises that can affect the measurements, especially at low frequencies. The different contributions shown in Fig. 2.5 dominate in different frequency ranges and together determine the overall detector sensitivity.

In the next subsections, we discuss the most important noise contributions in ground-based interferometers, starting from the fundamental quantum noise of the optical read-out and then moving on to displacement and other technical noise sources.

2.4.1 Optical read-out noise

Optical read-out noise arise from the quantum nature of light used to measure the differential motion of the interferometer mirrors. Since the measurement is performed using laser photons, quantum fluctuations in the light field introduce an uncertainty in the detector output. The two main categories are shot noise and radiation pressure noise. Together they form the quantum noise of the interferometer.

Shot noise

Shot noise arises because light is made of discrete photons. The photodetector measures the laser power by counting the number of photons arriving during a finite time interval. If N_γ photons are detected in a time T, the measured power is

$$P = \frac{N_\gamma \hbar \omega_L}{T}, \tag{2.38}$$

where ω_L is the laser angular frequency.

The arrival of photons is a random process that follows Poisson distribution. For a Poisson distribution, the fluctuation in the number of photons is

$$\Delta N_\gamma = \sqrt{N_\gamma}. \tag{2.39}$$

As a result, the measured optical power also fluctuates. The corresponding power fluctuation is

$$(\Delta P)_{\text{shot}} = \frac{1}{T} {N_\gamma}^{1/2} \hbar \omega_L = \left(\frac{\hbar \omega_L}{T} P \right)^{1/2}. \tag{2.40}$$

These fluctuations limit how accurately the phase difference between the two interferometer arms can be measured. For a Fabry-Perot Michelson interferometer, the strain sensitivity associated with shot noise can be written as [44]

$$S_n^{1/2}(f)\Big|_{\text{shot}} = \frac{1}{8\mathcal{F}L} \left(\frac{4\pi\hbar\lambda_L c}{\eta P_{\text{bs}}} \right)^{1/2} \sqrt{1 + \left(\frac{f}{f_p} \right)^2}, \tag{2.41}$$

where $\hbar$ is the reduced Planck constant, λ_L is the laser wavelength, $\mathcal{F}$ is the finesse of the cavity, L is the arm length, η is the photodetector efficiency, f_p is the cavity pole frequency and P_{bs} is the power at the beam splitter given by $P_{\text{bs}} = CP_0$ where P_0 is the input power and C is the factor gained with power recycling.

From this expression we see that shot noise decreases as the laser power increases. A larger number of photons reduces relative statistical fluctuations in the photon count, improving the precision of the measurement. Shot noise is typically the dominant noise source at high frequencies.

Radiation pressure noise

Increasing the laser power reduces shot noise, but it also introduces another source of quantum noise. Each photon carries momentum, and when it reflects from a mirror it exerts a pressure on the mirror. This produces a force known as radiation pressure. For a laser beam with power P, the force exerted on a reflecting mirror is

$$F = \frac{2P}{c}. \tag{2.42}$$

Because the number of photons fluctuates, the radiation pressure also fluctuates. These force fluctuations cause small random displacements of the mirrors. The corresponding fluctuation in force is related to the power fluctuations by $\Delta F = 2\Delta P/c$. Using Eq. 2.40,

$$\Delta F = 2\left(\frac{\hbar\omega_L}{c^2 T}P\right)^{1/2}. \tag{2.43}$$

For an interferometer with Fabry-Perot cavities, the strain sensitivity due to radiation pressure can be expressed as [44]

$$S_n^{1/2}(f)\Big|_{\text{rad}} = \frac{16\sqrt{2}\mathcal{F}}{ML(2\pi f)^2}\sqrt{\frac{\hbar P_{\text{bs}}}{2\pi\lambda_L c}}\frac{1}{\sqrt{1+(f/f_p)^2}}, \tag{2.44}$$

where M is the mirror mass.

Unlike shot noise, radiation pressure noise increases with laser power because larger power fluctuations produce larger force fluctuations on the mirrors. The $1/f^2$ dependence also shows that radiation pressure noise is most important at low frequencies.

Standard Quantum Limit

Shot noise and radiation pressure noise have opposite dependences on laser power. Increasing the power reduces shot noise but increases radiation pressure noise. The total optical read-out noise is obtained by combining the two contributions,

$$S_n(f)\Big|_{\text{opt}} = S_n(f)\Big|_{\text{shot}} + S_n(f)\Big|_{\text{rad}}. \tag{2.45}$$

For a given frequency, there exists an optimal laser power for which the two noise contributions become comparable. At this point the total optical noise reaches its minimum value. The corresponding sensitivity is known as the Standard Quantum Limit (SQL).

For a Fabry-Perot Michelson interferometer, the SQL strain sensitivity can be written as [44]

$$S_{\mathrm{SQL}}^{1/2}(f) = \frac{1}{2\pi f L}\sqrt{\frac{8\hbar}{M}}, \tag{2.46}$$

where L is the arm length and M is the mirror mass.

The SQL is not an absolute limit set by quantum mechanics. More advanced techniques, such as quantum non-demolition methods and the use of squeezed states of light, can further improve the sensitivity of gravitational-wave detectors.

2.4.2 Displacement noise

The optical read-out noise discussed above comes from the way we measure the motion of the test masses using laser light. However, the mirrors also move due to many other physical effects that are not related to gravitational waves. We group these effects as *displacement noise* and we characterize them with a displacement spectral density $S_x^{1/2}(f)$, which we simply denote as $x(f)$.

Since a gravitational wave changes the arm length as $\Delta L = hL$, a displacement Δx of a mirror produces the same effect as an equivalent strain $\Delta x/L$. Therefore, to express displacement noise in terms of strain, we divide by the arm length L. Unlike optical read-out noise, the finesse of the cavity does not improve displacement noise, because both the signal and the mirror motion are enhanced in the same way by the multiple bounces of light.

In general, displacement noise depends on many technical and environmental effects. The most important contributions are discussed below.

Seismic and Newtonian noise

Ground-based interferometers are constantly affected by ground motion. The Earth's surface is never completely still due to human activity such as traffic and trains, as well as natural effects like wind and ocean waves. There is also a micro-seismic background caused mainly by ocean activity, which produces surface waves that propagate through the Earth and shake the suspension system and the mirrors. This ground motion is referred to as *seismic noise*.

A simple model for seismic displacement noise can be written as [44]

$$x(f) \simeq A\left(\frac{1\,\mathrm{Hz}}{f^{\nu}}\right)\ \mathrm{m\,Hz^{-1/2}}, \tag{2.47}$$

where typically $\nu \simeq 2$ for frequencies above about 1 Hz, and $A \sim 10^{-7}$ in a quiet location. When this displacement is converted into strain by dividing by the arm length $L \sim$ 3-4 km, the resulting noise is still many orders of magnitude above the level needed for gravitational-wave detection. For this reason, seismic noise must be strongly reduced.

This is achieved by isolating the mirrors using multi-stage pendulum suspension systems. Each pendulum at frequencies above its resonance f_0, suppresses the noise by a factor roughly $(f_0/f)^2$. With multiple stages, the total suppression becomes much stronger. This is why ground-based detectors are only sensitive above roughly 10 Hz.

There is another fundamental source of noise called *Newtonian noise* or *gravity gradient noise*. This comes from small time-dependent changes in the local gravitational field produced by moving matter near the detector. The main contribution comes from density fluctuations in the ground caused by micro-seismic waves.

This type of noise is particularly difficult because gravity cannot be shielded. Unlike seismic noise, it cannot be removed by mechanical isolation. At present detectors, Newtonian noise is not the dominant limitation, since it is usually hidden by seismic noise at low frequencies and by thermal noise at higher frequencies. However, it is expected to become an important ultimate limit for ground-based detectors at low frequencies.

Thermal noise

Thermal noise arises from the random motion of atoms in the detector components due to their finite temperature. These thermal fluctuations cause small vibrations in both the mirrors and their suspension systems, producing displacement noise that can limit the sensitivity of the interferometer.

Thermal noise can be divided into two main categories: suspension thermal noise and test-mass thermal noise.

Suspension thermal noise: The mirrors are suspended by pendulum systems to isolate them from ground vibrations. These suspension itself undergoes thermal motion which can cause the mirrors to move and therefore introduce noise into the measurement. Suspension thermal noise is particularly important at low frequencies, typically from a few hertz up to several tens of hertz. The suspension wires also have resonant modes, known as violin modes, which appear as narrow peaks in the noise spectrum at frequencies of a few hundred hertz and above.

Test-mass thermal noise: Thermal fluctuations also occur within the mirrors themselves. One important contribution is Brownian noise, which originates from the random motion of atoms inside the mirror substrate and coating materials. In current detectors, coating Brownian noise is one of the dominant noise sources in the most sensitive frequency band. Temperature fluctuations can also produce noise through thermal expansion of the mirror materials. This effect is known as thermo-elastic noise. In addition, temperature variations change the refractive index of the mirror coatings, producing thermo-refractive noise.

Thermal noise is directly related to the dissipation present in the system, which depends strongly on the materials used. For this reason, considerable effort is spent on developing materials with lower mechanical losses for the mirrors, coatings, and suspension systems.

2.4.3 Other noise sources

In addition to optical read-out noise and displacement noise, a number of other noise sources can affect the sensitivity of a gravitational-wave interferometer. These effects are usually smaller, but they must still be controlled in order to reach the required sensitivity.

One important requirement is that the laser beams propagate in ultra-high vacuum. This is necessary to avoid fluctuations in the refractive index of air. In current detectors, the pressure is typically kept below 10^{-7} mbar, and even lower values (10^{-9} mbar) are required for advanced detectors. The vacuum system must also be free from contaminating gases, since even very small amounts of residual molecules can slowly deposit on the optical surfaces and reduce their performance over time.

Another limitation comes from scattered light. The mirror surfaces must be extremely smooth to reduce optical losses and unwanted reflections. Also, fluctuations in the laser itself, both in power and frequency, must also be kept under control. In addition, the interferometer relies on many servo systems to keep all optical degrees of freedom stable. Noise in these control systems can also couple into the signal.

Together, these noise sources illustrate the high level of control required to achieve the sensitivity of gravitational-wave detectors and highlight the complexity of these instruments.

Chapter 3

Neutron Stars and Magnetars

Neutron stars are the compact remnants left behind after core-collapse supernova explosions and as remnants of compact binary mergers, and are among the densest objects in the Universe. They provide a unique way to study matter at densities higher than those found in atomic nuclei, where the equation of state is still not well understood. Rapidly rotating neutron stars, especially newly born magnetars, are expected to be promising sources of long-transient gravitational waves because of their strong magnetic fields that can induce non-axisymmetric deformations, leading to the emission of gravitational radiation. Understanding the formation and physical properties of these objects is therefore important for developing astrophysical models of GW emission. On the other hand, the detection of such signals could provide valuable information about neutron-star properties and the physics of dense matter.

3.1 Structure and basic properties of neutron stars

Neutron stars represent the final evolutionary stage of massive stars that undergo core-collapse supernova explosions. They were first proposed theoretically by Baade and Zwicky [74] soon after the discovery of the neutron by Chadwick [75]. Observational confirmation came decades later through the discovery of bright X-ray sources such as Scorpius X-1 [76] and the subsequent identification of radio pulsars [77]. Today, thousands of neutron stars are known, including radio pulsars, X-ray binaries, magnetars, and millisecond pulsars.

Neutron stars typically possess masses upto about $2\,M_\odot$ or higher, compressed within radii of about 10-14 km, leading to central densities that exceed nuclear saturation density. Their interiors therefore provide a unique natural laboratory for studying matter under extreme conditions inaccessible to terrestrial experiments.

3.1.1 Stellar collapse and the formation of neutron matter

Neutron stars are formed during the final stages of the evolution of massive stars, typically with initial masses greater than about 8-10 $M_\odot$ [78], when they exhaust their nuclear fuel and can no longer support themselves against gravitational collapse. In these stars, nuclear burning proceeds through successive stages until an iron-rich core is formed. Since iron nuclei have the highest binding energy per nucleon, further fusion reactions no longer release energy. As the core mass approaches the Chandrasekhar limit [79], electron degeneracy pressure becomes insufficient to balance gravity and the core rapidly collapses. During the collapse, the density and pressure inside the core increase rapidly. Electrons are forced into protons through inverse beta decay,

$$e^- + p \rightarrow n + \nu_e, \tag{3.1}$$

where e^- is the electron, p is the proton, n is the neutron, and ν_e is the electron neutrino. This process decreases the number of electrons available to provide electron degeneracy pressure and causes the matter in the core to become increasingly neutron rich. The neutrinos produced escape from the collapsing core, carrying away a large fraction of the gravitational binding energy released during the collapse [80–82].

As the density rises to values comparable to nuclear density, $\rho \sim 2 \times 10^{14}\,\mathrm{g\,cm^{-3}}$, neutron degeneracy pressure and repulsive nuclear interactions halt the collapse of the inner core. The collapsing outer layers then rebound from the stiffened core, generating a shock wave that propagates outward and disrupts the star in a core-collapse supernova explosion [82–84]. The compact remnant left behind after the explosion is a neutron star.

3.1.2 Internal structure of neutron stars

The internal structure of a neutron star is commonly described as a sequence of distinct layers characterized by increasing density and changing physical composi-

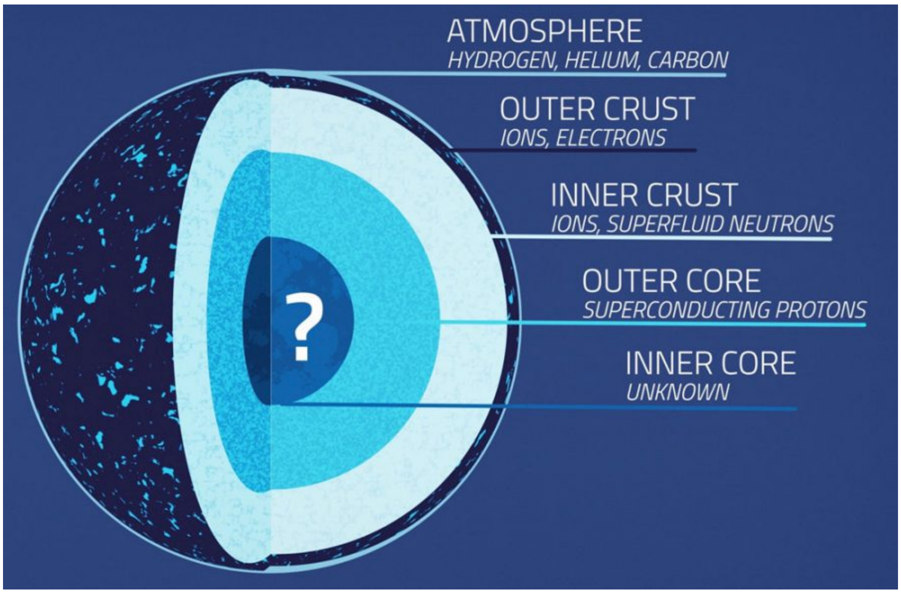

Figure 3.1. Schematic cross-section of a neutron star's internal anatomy, illustrating the progression from the outer atomic crust to the core. While the star is predominantly composed of neutrons, it features layers of varying nuclear compositions, with the exact state of matter and composition within the ultra-dense inner core remaining an active area of unknown physics. Image courtesy of NASA's Goddard Space Flight Center / Conceptual Image Lab.

tion, ranging from a solid crust to an ultra-dense fluid core. Although the exact composition of the deepest regions depends on the still uncertain equation of state of dense matter, the general layered structure is a robust prediction of neutron-star models [80, 81].

Accordingly, a neutron star is divided into three main regions: the atmosphere and outer crust, the inner crust, and the core. A schematic representation of this internal structure is shown in Figure 3.1.

Atmosphere and outer crust

The outermost layer of a neutron star is a thin atmosphere with a thickness of only a few centimetres. Below the atmosphere lies the outer crust, which extends from densities of roughly $10^6\,\mathrm{g\,cm^{-3}}$ up to the neutron drip threshold[1] at about $10^{11}\,\mathrm{g\,cm^{-3}}$. The outer crust is composed of a Coulomb lattice of increasingly neutron-rich nuclei embedded in a highly degenerate relativistic electron gas. As the density increases with depth, electron capture processes become more efficient, leading to progressively more neutron-rich isotopes.

Inner crust and neutron drip region

At densities above the neutron drip threshold ($\rho \sim 4 \times 10^{11}\,\mathrm{g\,cm^{-3}}$), neutrons begin to escape from nuclei and form a dilute neutron gas coexisting with neutron-rich nuclei and electrons. This region is known as the inner crust.

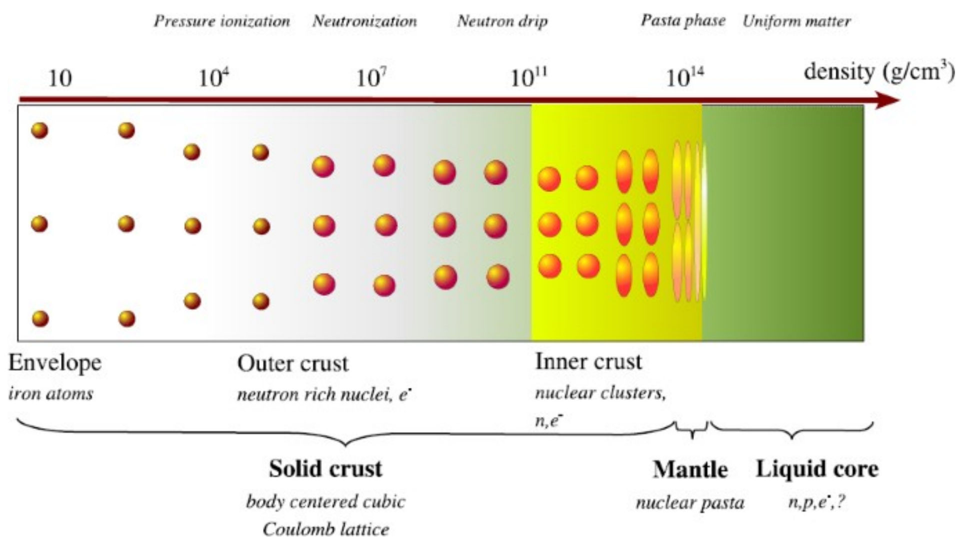

Figure 3.2. Schematic progression of the "nuclear pasta" phases within the inner crust and mantle of a neutron star, shown along the increasing density axis. The structural configurations transition from spherical droplets to complex rods and slabs as matter approaches the uniform core liquid boundary. Image adapted from Chamel and Haensel [85].

[1]The neutron drip threshold corresponds to the density at which neutrons are no longer completely bound inside atomic nuclei and begin to drip out into the surrounding space.

In the inner crust, the competition between nuclear attraction and Coulomb repulsion gives rise to complex nuclear configurations. As the density approaches nuclear saturation density, nuclei are predicted to deviate from spherical symmetry and may form extended structures collectively known as nuclear pasta phases (see Fig. 3.2). These include rod-like ("spaghetti") and slab-like ("lasagna") geometries, and are expected to occur near the transition between the crust and the uniform liquid core [85].

Core

The core contains most of the neutron star mass and extends to densities above nuclear saturation density, $\rho_0 \approx 2.7 \times 10^{14}\,\mathrm{g\,cm^{-3}}$. The outer core is generally expected to consist of neutrons with a small fraction of protons, electrons, and muons in beta equilibrium, where weak interaction processes maintain equilibrium between neutrons, protons, and leptons. At higher densities, corresponding to the inner core, the composition is not well constrained and may include exotic degrees of freedom such as hyperons, meson condensates, or deconfined quark matter [86, 87].

3.1.3 Equation of state of dense matter

The equation of state (EOS) describes the relation between pressure, density, and temperature inside neutron star matter. It determines the properties of neutron stars, including their mass-radius relation, maximum stable mass, and internal structure [81, 86].

At densities below nuclear saturation density, the EOS is relatively well constrained by nuclear experiments. But at the much higher densities reached in neutron star cores, the behaviour of matter remains uncertain. Different theoretical models predict different compositions and pressure-density relations, leading to significant uncertainties in neutron star radii and core properties. This dependence is commonly illustrated through the neutron star mass-radius relation, which varies significantly between different EOS models [88, 89].

The EOS is particularly important for gravitational-wave studies because it affects quantities such as the moment of inertia and maximum possible ellipticity [86]. These properties influence both the amplitude and evolution of GW signals emitted by these sources.

3.1.4 Rotation and magnetic fields in neutron stars

Neutron stars are characterized by extremely fast rotation and strong magnetic fields. These properties arise during the collapse of the progenitor star. As the stellar core contracts from a radius of several thousand kilometres to only about 10 km, conservation of angular momentum causes the rotation rate to increase dramatically. At the same time, magnetic flux conservation amplifies the stellar magnetic field to values many orders of magnitude larger than those found in ordinary stars [18, 80, 81, 90].

Newly formed neutron stars are therefore expected to rotate rapidly, with initial spin periods that may range from milliseconds to several seconds. The corresponding rotational energy can be very large and is given approximately by

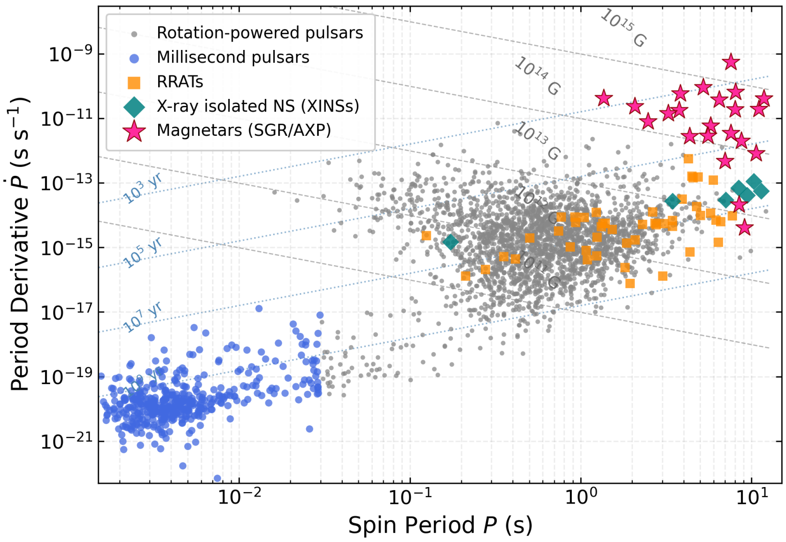

Figure 3.3. The P-$\dot{P}$ diagram for the known neutron star population, using data from the ATNF Pulsar Catalogue [91]. Few standard sub-populations are labelled. Dashed black lines are contours of constant inferred surface dipolar magnetic field; dotted blue lines mark contours of constant characteristic age. Magnetars occupy the upper-right region with the highest inferred field strengths. The newborn magnetars targeted in this thesis are expected to have been born with millisecond spin periods, placing them initially at the far left of the diagram before spinning down under combined electromagnetic dipole and gravitational-wave torques.

$$E_{\rm rot} = \frac{1}{2} I \Omega^2, \tag{3.2}$$

where I is the moment of inertia and Ω is the angular velocity of the star. For millisecond rotation periods, the rotational energy may exceed 10^{52} erg, making young neutron stars potentially important central engines for energetic astrophysical phenomena.

The magnetic fields of neutron stars are typically inferred from measurements of their rotational spin-down. Ordinary radio pulsars generally possess surface dipolar magnetic fields of order 10^{11}-10^{13} G, while more extreme neutron stars known as magnetars may reach inferred surface dipolar field strengths of 10^{14}-10^{15} G [92]. These magnetic fields strongly influence the rotational evolution and electromagnetic emission of the star. The diverse neutron star population and its sub-classes are visualised in the P-$\dot{P}$ diagram, shown in Figure 3.3, which displays the spin period against its time derivative for all known neutron stars with measured timing parameters [91].

The largest known population of Neutron Stars consists of radio pulsars, which emit highly regular pulses of radio waves powered by rotational energy loss. Millisecond pulsars are a rapidly rotating subclass with spin periods below about $1 - 10$ ms and relatively weaker magnetic fields.

In contrast, magnetars are characterized by intense X-ray and gamma-ray activity which are primarily powered by magnetic energy rather than rotation [18, 92, 93].

Their extremely strong magnetic fields are believed to play an important role in the production of energetic bursts and flares observed from these sources [93–95]. Because of their rapid initial rotation and extremely strong magnetic fields, newborn magnetars are particularly interesting in the context of gravitational-wave astronomy. Strong magnetic fields may deform the stellar structure from perfect axial symmetry, while rapid rotation provides a large reservoir of rotational energy that can power long-lasting gravitational-wave emission. These properties make newborn magnetars promising candidates for long-transient gravitational-wave signals.

3.2 Magnetars

Magnetars are a special type of neutron star with extremely strong magnetic fields. Their surface magnetic fields are typically of the order of 10^{14}-10^{15} G, making them the strongest known magnets in the Universe [18, 27, 92–94].

3.2.1 Observed properties of magnetars

Magnetars are mainly observed as two classes of X-ray sources known as Soft Gamma Repeaters (SGRs) and Anomalous X-ray Pulsars (AXPs). These objects show recurrent X-ray and gamma-ray bursts, giant flares, and persistent X-ray emission [27, 92–94]. Unlike ordinary radio pulsars, their observed emission cannot be explained only through rotational energy loss. Instead, the main energy source is believed to be the decay of their extremely strong magnetic fields [27, 94].

Although only a relatively small number of magnetars are currently known in our galaxy, population studies suggest that their formation rate in the galaxy is estimated to be 2.3-20 per kyr, with a fraction $0.4^{+0.6}_{-0.28}$ of all neutron stars being born as magnetars (corresponding to 12-100% at the 2σ confidence level) [96]. Because newborn magnetars combine rapid rotation, strong magnetic fields, and possible asymmetries produced during their formation, they are considered promising sources of long-transient gravitational waves.

3.2.2 Formation of newborn magnetars

Magnetars are suggested to form during core-collapse supernova explosions of massive stars or after binary neutron star mergers [18, 24]. In the first seconds after the birth of the neutron star, the hot proto-neutron star is expected to undergo strong convection together with rapid differential rotation. If the newborn star rotates sufficiently rapidly, with an initial spin period of the order of a few milliseconds, these motions can amplify the magnetic field through an efficient dynamo mechanism [18].

In this scenario, differential rotation inside the proto-neutron star strengthens the magnetic field lines, while convective motions help regenerate the poloidal component of the field. Together, these dynamo processes can amplify the surface magnetic field to strengths of about 10^{14}-10^{15}, G within a few seconds after the neutron star is born, leading to the formation of a magnetar.

Newborn magnetars are expected to rotate very rapidly, with initial spin periods of only a few milliseconds. Combined with their extremely strong magnetic fields, this makes them possible central engines for energetic astrophysical transients such as superluminous supernovae and gamma-ray bursts [40, 97–99]. Their rapid rotation also provides a large reservoir of rotational energy that can potentially power long-lasting gravitational-wave emission [20–24].

3.2.3 Internal and external magnetic fields

The magnetic field of a magnetar is expected to have both poloidal and toroidal components. The poloidal field is the component whose field lines emerge from one magnetic pole and re-enter through the other pole. Its large-scale dipole component extends outside the star and is responsible for the electromagnetic spin-down observed in pulsars and magnetars [16].

The toroidal field has magnetic field lines that go around the star in the azimuthal direction and are expectd to be mainly confined to the interior [100]. Although this component cannot be measured directly, theoretical studies suggest that it may form a significant fraction of the total magnetic energy inside a magnetar [24, 100, 101].

Modern models considers mixed poloidal-toroidal configurations, referred to as twisted-torus magnetic fields. Such configurations are expected to be more stable than purely poloidal or purely toroidal fields [102, 103] and may survive on long timescales inside neutron stars [24, 100].

The geometry of the internal magnetic field is particularly important because it determines the magnitude and sign of the magnetic deformation of the star [104, 105] and thus, it directly affects the strength of any gravitational-wave emission [24].

3.3 Magnetic deformations and ellipticity

Magnetars can emit gravitational waves only if their mass distribution is not perfectly symmetric around the rotation axis. In newborn magnetars, one of the sources that results in this asymmetry is the presence of extremely strong internal magnetic fields.

Magnetic fields exert anisotropic stresses on the stellar matter and can deform the equilibrium shape of the star. The resulting deformation is commonly described by the ellipticity

$$\epsilon = \frac{I_{xx} - I_{yy}}{I_{zz}}, \tag{3.3}$$

where I_{xx}, I_{yy} and I_{zz} are the principal moments of inertia, with the z-axis taken to be the rotation axis. A non-zero ellipticity corresponds to a non-axisymmetric mass distribution and therefore to a time-varying quadrupole moment, which is required for gravitational-wave emission.

The value of ϵ depends mainly on the internal magnetic field geometry. A predominantly poloidal magnetic field generally produces an oblate deformation, whereas a strong toroidal field tends to deform the star into a prolate shape [100].

For a magnetically deformed neutron star, the ellipticity is approximately proportional to the ratio between magnetic energy and gravitational binding energy,

$$\epsilon_B \sim \frac{E_B}{W}, \tag{3.4}$$

where E_B is the magnetic energy stored inside the star and W is its gravitational binding energy [24]. For strong toroidal magnetic fields, the ellipticity can be estimated as

$$\epsilon_B \approx 4 \times 10^{-4} \left(\frac{k_B}{4}\right) B_{\mathrm{int},16}^2 R_6^4 M_{1.4}^{-2}, \tag{3.5}$$

where $B_{\mathrm{int},16}$ is the internal magnetic field strength in units of 10^{16} G, R_6 is the stellar radius in units of 10^6 cm, $M_{1.4}$ is the stellar mass in units of $1.4\,M_\odot$, and k_B is a geometrical factor that depends on the magnetic-field configuration [24]. This relation shows that magnetars with internal magnetic fields around 10^{16} G can develop ellipticities of order 10^{-4}-10^{-3}.

Other mechanisms may also produce non-axisymmetric deformations. Examples include secular bar-mode instabilities in rapidly rotating proto-neutron stars and accretion-induced mountains formed by asymmetric matter accumulation [106–108].

3.4 Spin evolution and braking mechanisms

After their formation, newborn magnetars gradually lose rotational energy and spin down over time. The spin evolution is due to the torques acting on the magnetar, mainly electromagnetic dipole radiation and gravitational-wave emission [21, 80].

The rotational evolution of a neutron star is commonly described as

$$\dot{\Omega} = -k\Omega^n, \tag{3.6}$$

where Ω is the angular velocity of the star, k is a constant that depends on the physical emission mechanism, and n is known as the braking index. The braking index determines how strongly the spin-down depends on the rotational frequency of the source.

Different values of n correspond to different physical mechanisms [29]. In the case of wind braking ($n = 1$), the spin-down is driven by a relativistic outflow of particles from the neutron star magnetosphere. This wind is powered by strong electric fields induced by strong magnetic fields, which can extract charged particles from the stellar surface and accelerate them to relativistic speeds [109].

The standard magnetic dipole braking model corresponds to $n = 3$. In this case, the magnetar is considered as a rotating magnetic dipole in vacuum, and energy loss is dominated by electromagnetic radiation [110].

If the star has a non-axisymmetric mass distribution, gravitational waves are emitted at twice the rotation frequency. In the simplest case of a static quadrupolar deformation, the resulting gravitational-wave spin-down corresponds to $n = 5$ [44]. This regime is particularly relevant for newborn magnetars, where strong internal magnetic fields can generate such deformations. Higher braking indices, such as $n = 7$, can occur when spin-down is dominated by gravitational-wave emission from fluid oscillation modes (r-modes), which involve time-dependent perturbations of the stellar fluid [111]. In this case, the emission is not caused by a fixed deformation but by unstable oscillations driven by rotation.

In realistic magnetars, more than one mechanism can operate simultaneously. As a result, the effective braking index may differ from these ideal values and can evolve with time depending on the internal structure, magnetic field configuration, and other conditions [112]. In this thesis, two limiting cases are considered. The long-transient gravitational-wave searches presented in Chapters 4 and 8 assume a gravitational-wave dominated spin-down regime with $n = 5$ for a rotating non-axisymmetric newborn magnetar. In contrast, the electromagnetic shock breakout analysis in Chapter 5 assumes magnetic dipole spin-down with $n = 3$.

As the magnetar spins down, the gravitational-wave frequency evolves in time, producing long-lasting signals that slowly drift in frequency over timescales of hours to days. This frequency evolution is a key feature exploited by semi-coherent search methods used in this work.

3.5 Gravitational-wave emission mechanisms in magnetars

Several physical mechanisms have been proposed that can generate gravitational-wave emission from rapidly rotating newborn magnetars. These mechanisms differ in both the physical origin of the emission and the resulting gravitational-wave signal. We discuss some of the most important mechanisms below.

3.5.1 Magnetically-induced quadrupolar deformations

Strong internal magnetic fields in newborn magnetars can deform the stellar structure away from spherical symmetry, as described in Sec. 3.3. The properties of the resulting deformation depend on the geometry and relative strength of the internal magnetic-field components. In simplified configurations, a predominantly poloidal field tends to produce an oblate deformation, while a strong toroidal component tends to produce a prolate deformation [100]. More generally, magnetic stresses can support non-axisymmetric distortions of the stellar mass distribution.

In this thesis, the detailed internal magnetic-field geometry is not modeled explicitly. Instead, the gravitational-wave source is described phenomenologically as a non-precessing triaxial neutron star rotating about one of its principal axes. The relevant equatorial asymmetry is characterized by the ellipticity ϵ, which measures the difference between the principal moments of inertia perpendicular to the rotation axis. For a non-axisymmetric configuration with $I_{xx} \neq I_{yy}$, the stellar mass quadrupole changes orientation as the star rotates, giving rise to gravitational-wave emission.

For this emission model, the dominant gravitational-wave component is emitted at twice the stellar rotation frequency,

$$f_{\rm gw} = 2 f_{\rm rot}, \tag{3.7}$$

where $f_{\rm rot}$ is the stellar rotation frequency [44]. As the star loses rotational energy, its rotation frequency decreases and the gravitational-wave amplitude also evolves, producing a long-transient signal whose frequency sweeps downward over timescales ranging from hours to days [24, 113]. The corresponding gravitational-wave luminosity and spin-down evolution are discussed in detail in Sec. 3.6.

3.5.2 Free precession and the spin-flip mechanism

A different possible configuration arises when an approximately axisymmetric deformation has its symmetry axis misaligned with the stellar angular momentum. In this case, the neutron star can undergo free precession [114]. During free precession, the orientation of the deformation changes with respect to the angular momentum, leading to a time-dependent quadrupole moment and potentially modifying the gravitational-wave emission.

Internal viscous dissipation gradually damps the precession while approximately conserving angular momentum [21, 100, 114]. The effect of this dissipation depends on the shape of the star. For a prolate star, as expected when the internal magnetic field is dominated by a strong toroidal component, dissipation tends to increase the angle between the symmetry axis and the angular momentum. The star can therefore evolve towards a nearly perpendicular configuration, a process known as the spin-flip mechanism [21, 100]. This configuration increases the time-varying quadrupole moment and can enhance the gravitational-wave emission. For an oblate star, dissipation instead tends to drive the system towards alignment, reducing the gravitational-wave emission.

Free precession and spin-flip evolution therefore represent additional possible channels through which magnetic deformations can produce or enhance gravitational-wave emission from newborn magnetars. These dynamics are not explicitly included in the signal model adopted in this thesis, which assumes a non-precessing triaxial neutron star rotating about a principal axis. They are discussed here as complementary astrophysical motivation for gravitational-wave emission from magnetically deformed newborn neutron stars.

3.5.3 Bar-mode instabilities

Very rapidly rotating proto-neutron stars may also develop non-axisymmetric fluid instabilities. If the ratio between rotational kinetic energy T and gravitational binding energy $|W|$ becomes sufficiently large, the star can become unstable to bar-like deformations [106, 115]. The secular bar-mode instability is triggered when $T/|W| \gtrsim 0.14$, while the dynamical instability requires $T/|W| \gtrsim 0.27$ [106, 115].

In this scenario the stellar fluid adopts an elongated shape that rotates with respect to an inertial observer, producing strong gravitational-wave emission. The emitted signal frequency is typically $f_{\rm gw} \approx 2f_{\rm rot}$ [106].

Bar-mode instabilities can in principle produce stronger gravitational-wave signals than magnetically induced deformations, but they require extremely rapid rotation and their occurrence in newborn neutron stars remains uncertain [24].

3.5.4 r-mode oscillations

Another possible source of gravitational waves is provided by r-modes, which are global oscillation modes of rotating fluid stars. These modes are restored primarily by the Coriolis force and can become unstable through the Chandrasekhar-Friedman-Schutz (CFS) mechanism [116, 117].

Unlike the case of a permanent deformation, the gravitational radiation is generated by oscillatory fluid motions inside the star rather than by a fixed quadrupole moment. For the dominant $l = m = 2$ r-mode, the gravitational-wave frequency is approximately $f_{\rm gw} \approx (4/3) f_{\rm rot}$ [111].

In the standard model in which r-mode gravitational-wave emission dominates the spin-down, the corresponding braking index is $n = 7$. The growth and saturation of r-modes depend on several uncertain physical processes, including viscosity, superfluidity, and the thermal evolution of the neutron star [118, 119]. Their role in newborn magnetars therefore remains an active area of research.

3.5.5 Accretion-induced mountains

In accreting neutron stars, asymmetric accretion of material onto the stellar surface can build up a non-axisymmetric mountain, sustaining a persistent ellipticity [107, 108]. This mechanism is less relevant for the isolated newborn magnetars considered in this thesis, but is an important GW source for accreting systems in low-mass X-ray binaries.

In this thesis we focus on gravitational-wave emission from a rotating neutron star with a long-lived quadrupolar deformation produced by strong internal magnetic fields. In this model the GW signal is emitted predominantly at twice the rotation frequency and the spin evolution is described by a braking index $n = 5$.

3.6 Newborn magnetars as sources of gravitational waves

As discussed in the section 3.5.1, strong internal magnetic fields can induce a non-zero ellipticity in newborn magnetars. In the signal model adopted in this thesis, the neutron star is treated phenomenologically as a non-precessing triaxial rotator, with the relevant non-axisymmetric deformation characterized by an ellipticity ϵ. The rotating deformation produces a time-varying mass quadrupole moment and therefore gravitational-wave emission [20, 100, 120].

The power emitted in gravitational waves from a rotating non-axisymmetric neutron star is approximately given by [44]

$$\dot{E}_{\rm GW} = \frac{32}{5}\frac{G\epsilon^2 I^2 \Omega^6}{c^5}, \tag{3.8}$$

where G is the gravitational constant, c is the speed of light, I is the moment of inertia, ϵ is the ellipticity, and Ω is the angular velocity of the star. The strong dependence on Ω shows that rapidly rotating newborn magnetars are very efficient emitters of gravitational waves.

As the star emits gravitational waves, it loses rotational energy. The rotational energy of the star is

$$E_{\rm rot} = \frac{1}{2} I \Omega^2. \tag{3.9}$$

The loss of rotational energy must equal the energy carried away by gravitational waves,

$$\dot{E}_{\rm rot} = -\dot{E}_{\rm GW}. \tag{3.10}$$

Assuming that the moment of inertia I remains constant during the spin-down evolution, the time derivative of the rotational energy is $\dot{E}_{\text{rot}} = I\Omega\dot{\Omega}$. Substituting the expression for $\dot{E}_{\text{GW}}$, we obtain

$$I\Omega\dot{\Omega} = -\frac{32}{5}\frac{G\epsilon^2 I^2 \Omega^6}{c^5}. \tag{3.11}$$

Dividing both sides by $I\Omega$ gives

$$\dot{\Omega} = -\frac{32G\epsilon^2 I}{5c^5}\Omega^5. \tag{3.12}$$

This corresponds to the gravitational-wave dominated regime with braking index $n = 5$, emitted at frequency $f_{\text{gw}} = 2f_{\text{rot}} = \Omega/\pi$. As the emission of gravitational waves removes angular momentum from the star, the rotation rate gradually decreases. As a result, the gravitational-wave frequency also decreases with time.

Newborn magnetars are therefore expected to be long-transient gravitational-wave sources. Their signals can last from hours to days, depending on the initial spin period, magnetic field strength, ellipticity, and the dominant spin-down mechanism. During this time, the signal evolves continuously in frequency, rather than remaining monochromatic. These characteristics make newborn magnetars promising targets for directed searches in detector data. Their time-evolving signals require dedicated semi-coherent search methods that can track frequency evolution over long durations. These methods are introduced in the following chapters on long-transient gravitational waves.

Chapter 4

Long-Transient Gravitational Waves

Long-transient gravitational waves form an intermediate class of signals between short-duration transients, such as those produced by compact binary coalescences or core-collapse supernovae, and persistent continuous waves, such as those emitted by isolated spinning neutron stars [16]. They are expected to last from several hours to days, during which both the amplitude and the frequency of the signal evolve significantly.

In this thesis, we focus on long-transient signals produced by newborn magnetars under the assumption that their early evolution is dominated by gravitational-wave emission. This assumption provides a specific signal model that can be used for directed searches.

4.1 Signal model

We consider a newborn magnetar emitting gravitational waves due to a non-axisymmetric deformation. The key quantity describing the deviation from axial symmetry is the ellipticity, ϵ (see Eq. 3.3). A non-zero ellipticity leads to a time-varying quadrupole moment, which is necessary for GW emission. Throughout this work, we assume ϵ is constant over the signal duration. This simplifies the evolution of both amplitude and frequency, and is a commonly adopted approximation in models of gravitational-wave emission from rapidly rotating neutron stars. Time-dependent deformations would introduce additional complexity and are beyond the scope of this work.

4.1.1 Frequency evolution

The rotational kinetic energy stored in a rapidly rotating newborn magnetar can exceed 10^{52} erg. If a significant fraction of this energy is radiated through gravitational waves, the star can undergo rapid spin-down, resulting in a significant evolution of the GW frequency over the signal duration. While frequency spin-down is also present in standard continuous-wave signals, it is typically described using a Taylor expansion in frequency derivatives over the relevant observation time. For the rapidly evolving newborn-magnetar signals considered here, such an approximation may become inaccurate. We therefore model the frequency evolution directly using the physical power-law spin-down relation derived below.

As derived in Sec. 3.6, in the gravitational-wave dominated regime the angular velocity evolves as

$$\dot{\Omega} = -\frac{32G\epsilon^2 I}{5c^5}\Omega^5, \tag{4.1}$$

which corresponds to a braking index $n = 5$.

This equation shows that the loss of rotational energy through gravitational-wave emission causes the star to spin down more rapidly at higher rotation rates. As Ω decreases, the spin-down becomes progressively slower.

For a rigid star rotating about a principal axis, the spin frequency is $f_{\rm rot} = \Omega/2\pi$, and the gravitational-wave frequency is emitted at twice this value,

$$f_{\rm gw} = 2f_{\rm rot} = \frac{\Omega}{\pi}. \tag{4.2}$$

Therefore, the evolution of the gravitational-wave frequency directly follows from the evolution of Ω.

Using $f_{\rm gw} = \Omega/\pi$, the spin-down equation can be rewritten as

$$\dot{f}_{\rm gw} = -kf_{\rm gw}^5, \tag{4.3}$$

where the constant k describes the physical parameters of the source:

$$k = \frac{32\pi^4 G}{5c^5}\epsilon^2 I. \tag{4.4}$$

Solving this equation gives the time evolution of the frequency,

$$f_{\rm gw}(t) = \frac{f_0}{(1+\frac{t-t_0}{\tau})^{1/4}}, \tag{4.5}$$

where $f_0 \equiv f_{\rm gw}(t_0)$ is the initial GW frequency at the start of the observation and

$$\tau = \frac{1}{4kf_0^4}. \tag{4.6}$$

Here, τ is the characteristic spin-down timescale. In the limits $(t-t_0) \ll \tau$ and $(t-t_0) \gg \tau$, Eq. (4.5) approaches $f_{\rm gw}(t) \simeq f_0$ and $f_{\rm gw}(t) \propto (t-t_0)^{-1/4}$, respectively.

This result shows that the GW frequency decreases smoothly with time as the star loses rotational energy. The evolution is faster at early times when the star rotates rapidly, and gradually slows down as the star spins down. As a result, the emitted signal is not monochromatic but drifts in frequency over time, producing a characteristic long-transient gravitational-wave signal. This behaviour is illustrated in Fig. 4.1 for representative values of f_0 and ϵ.

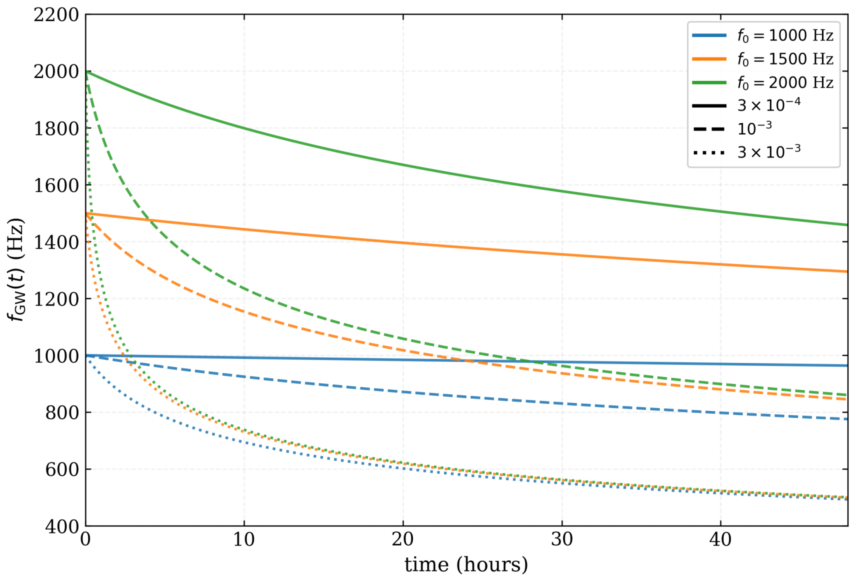

Figure 4.1. Gravitational-wave frequency evolution $f_{\mathrm{gw}}(t)$ for a newborn magnetar in the GW-dominated spin-down regime ($n = 5$), computed from Eq. (4.5). Line colour indicates the initial GW frequency $f_0 \in \{1000, 1500, 2000\}$ Hz; line style indicates the ellipticity $\epsilon \in \{3 \times 10^{-4}, 10^{-3}, 3 \times 10^{-3}\}$. The magnetar parameters are fixed at $M = 1.4\, M_\odot$ and $R = 12\,\mathrm{km}$. Higher ellipticity produces faster spin-down and a steeper frequency drift, while higher f_0 sets a larger initial frequency.

4.1.2 Strain amplitude evolution

The gravitational-wave strain amplitude from a rotating triaxial star is [54]

$$h_0(t) = \frac{4\pi^2 G}{c^4} \frac{I\epsilon}{d} f_{\mathrm{gw}}^2(t), \tag{4.7}$$

where d is the source distance. The f_{gw}^2 dependence means the amplitude is largest at early times when the star rotates fastest, and decreases as it spins down. Similarly, $h_0 \propto \epsilon$, so larger deformations produce stronger signals.

Substituting the frequency evolution gives

$$h_0(t) = \frac{4\pi^2 G}{c^4} \frac{I\epsilon}{d} f_0^2 \left(1 + \frac{t - t_0}{\tau}\right)^{-1/2}. \tag{4.8}$$

This shows that both amplitude and frequency decrease together as the star spins down.

The moment of inertia I is a key parameter in both the amplitude and frequency evolution of the gravitational-wave signal. It is estimated from neutron star structure models, which depend on the equation of state of dense matter. To estimate realistic values of I, we use the empirical relation [121]

$$I \approx MR^2 \left(0.247 + 0.642\beta + 0.466\beta^2\right), \tag{4.9}$$

where the compactness parameter is defined as

$$\beta = \frac{GM}{c^2 R}. \tag{4.10}$$

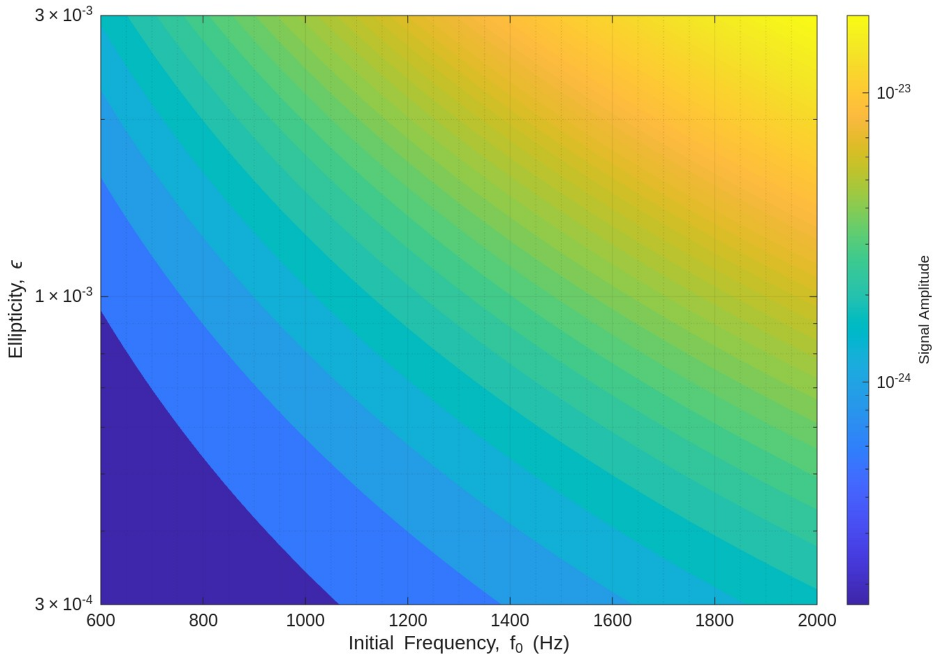

Figure 4.2. Initial gravitational-wave strain amplitude $h_0(t_0)$ as a function of initial GW frequency f_0 and ellipticity ϵ, computed using Eq. 4.8. The moment of inertia is estimated using Eq. 4.9 for a fiducial neutron star with $M = 1.4\,M_\odot$ and $R = 12\,\mathrm{km}$. The source distance is fixed to 1 Mpc for illustration. This figure shows the expected range of GW amplitudes for newborn magnetars in the GW-dominated spin-down regime.

This relation is valid for neutron star compactness values ($\beta \gtrsim 0.1$) and assumes a maximum mass satisfying $M_{\max} \gtrsim 1.97\,M_\odot$.

Figure 4.2 shows the expected range of initial gravitational-wave amplitudes for newborn magnetars. The amplitude strongly depends on both the initial frequency and the ellipticity. Rapidly rotating magnetars with larger deformations produce significantly stronger signals, making them promising candidates for detection.

4.1.3 Dependence on source parameters

The amplitude and evolution of the long-transient signal considered here depend primarily on the source distance d, ellipticity ϵ, and initial frequency f_0. From Eq. (4.8),

$$h_0 \propto \frac{\epsilon f_0^2}{d}. \tag{4.11}$$

Therefore, nearby sources, large ellipticities, and high initial frequencies produce larger gravitational-wave amplitudes. However, the instantaneous amplitude h_0 alone does not determine whether a signal can be detected. Detectability also depends on the detector noise and on how the signal evolves and accumulates over the observation time.

The same source parameters that determine the amplitude also determine the spin-down timescale τ, and therefore the duration and frequency evolution of the signal. For example, a larger ellipticity increases the GW amplitude but also produces a faster spin-down. Therefore the sensitivity of a search depends on the combined effect of the signal amplitude, its evolution and duration, and the detector noise.

4.2 Energy budget and detectability

The total rotational energy available to power gravitational-wave emission is

$$E_{\mathrm{rot},0} = \frac{1}{2} I \Omega_0^2 \tag{4.12}$$

In the gravitational-wave-dominated spin-down regime adopted throughout this thesis ($n = 5$), we assume that all rotational energy is released through gravitational-wave emission. Thus $E_{\mathrm{rot},0}$ is the actual total energy radiated as gravitational waves over the lifetime of the signal.

Figure 4.3 shows $E_{\mathrm{rot},0}$ as a function of f_0 across the parameter space explored in this thesis. Note that $E_{\mathrm{rot},0}$ depends only on f_0 and not on ϵ: the ellipticity determines how quickly the energy is radiated through the timescale τ (Eq. (4.6)), but not the total energy reservoir. Across the range $f_0 \in [600, 2000]$ Hz, the total GW energy emitted ranges from approximately 3×10^{51} to 3×10^{52} erg, comparable to the total energy released in a core-collapse supernova. This large energy output, combined with the $h_0 \propto f_0^2$ scaling of the strain amplitude, makes rapidly rotating newborn magnetars among the most energetically promising sources for long-transient gravitational-wave searches with current detectors.

The signal model described in this chapter forms the basis of all searches presented in the rest of this thesis. The frequency evolution (Eq. 4.5) and amplitude evolution

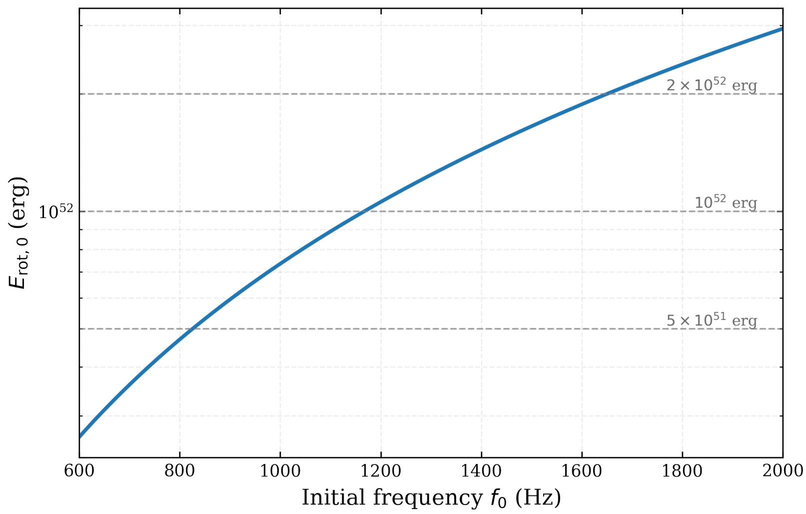

Figure 4.3. Total rotational energy emitted $E_{\mathrm{rot},0} = \frac{1}{2} I \Omega_0^2$ as a function of initial GW frequency f_0, computed from Eq. (4.12) for $M = 1.4\, M_\odot$ and $R = 12$ km. In the $n = 5$ GW-dominated regime assumed throughout this thesis, all rotational energy is radiated as gravitational waves, so $E_{\mathrm{rot},0}$ gives the total emitted GW energy.

(Eq. 4.8) define the trajectories followed by candidate signals in the parameter space explored by the GFH-v2 pipeline discussed in Chapters 6, 7, and 8.

Chapter 5

Electromagnetic Counterpart: Shock breakout

The study of electromagnetic counterparts to gravitational-wave sources has become an essential part of multi-messenger astrophysics. As discussed in Chapters 3 and 4, newly born magnetars are promising sources of long-transient gravitational waves. However, the detection of these GW signals critically depends on independent EM triggers, which provide precise source localization and timing information [22, 23, 122].

A core-collapse supernova produces electromagnetic emission as the explosion evolves and the ejecta expand. If the core collapse leaves behind a rapidly rotating magnetar, the newborn compact object can additionally inject its rotational energy into the expanding supernova ejecta. This central-engine energy injection can drive a shock through the ejecta and produce an early-time emission known as a magnetar-driven shock breakout (SBO) [40].

By the time the magnetar-powered shock propagates through the outer ejecta, the material has expanded to a relatively large radius. The resulting emission can consequently extend over several days and emerge predominantly at ultraviolet wavelengths [40]. Importantly, its properties depend on the energy injected by the central engine and therefore on the magnetar spin period and magnetic field, in addition to the properties of the supernova ejecta. This makes the magnetar-driven SBO a potential observational signature of a rapidly rotating newborn magnetar.

The ultraviolet emission is particularly relevant for wide-field UV missions such as ULTRASAT, which will operate in the 230-290 nm range with high cadence [123]. An early UV detection can identify the explosion promptly and provide a trigger for a directed long-transient gravitational-wave search. Also, the luminosity and timescale of a magnetar-powered SBO depend on the magnetar spin period P and magnetic field B, as well as on the ejecta mass and explosion energy. Modeling the observed light curve can therefore possibly constrain these parameters and provide information on the nature of the compact remnant.

In this chapter, we investigate the theoretical modeling, observational properties, and detectability of magnetar-powered SBOs, with particular focus on their multi-messenger implications, directly connecting the EM signal properties with the GW emission discussed in Chapters 2-4. We build upon the results presented in [38], which explored the ULTRASAT detectability and expected event rates of such SBOs.

5.1 Magnetar-driven shock breakout

A newly born, rapidly rotating magnetar can significantly affect the early evolution of a core-collapse supernova. Following its formation, the magnetar loses rotational energy and launches a highly magnetized relativistic wind. This wind carries energy predominantly in the form of electromagnetic flux and relativistic particles. Because the wind is confined by the surrounding supernova ejecta, its energy accumulates behind the ejecta and inflates an high pressure magnetar-wind bubble [40].

The pressure of this bubble acts dynamically on the inner supernova ejecta, sweeping material into a shell and driving a forward shock through the already expanding ejecta. As the magnetar-driven shock propagates outward, it heats and compresses the ejecta. When the shock approaches the outer layers, the optical depth decreases and radiation can begin to escape. At this point, the shock becomes radiative and releases a burst of electromagnetic emission. This event is known as a magnetar-driven shock breakout (SBO).

The magnetar-driven shock breakout occurs after the supernova ejecta have expanded to radii of order 10^{14} cm. The large emitting radius results in a relatively long-duration and cooler transient, with characteristic effective temperatures of order $\sim 10^4$-2×10^4 K, which therefore places the emission in the UV band targeted by missions such as ULTRASAT.

In the context of this thesis, the magnetar-driven SBO is particularly interesting because it can provide information beyond the detection of the supernova itself.

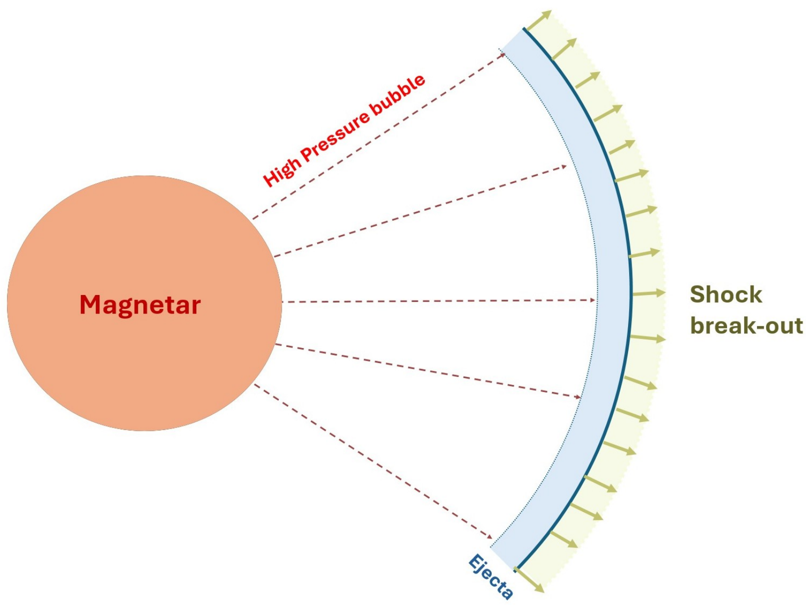

Figure 5.1. Schematic representation of a magnetar-driven shock breakout.

While the observation of a CCSN establishes that a massive star has exploded, a magnetar-powered feature in the early UV light curve can provide evidence for continued energy injection by a rapidly rotating compact remnant. Such an observation can therefore help identify systems in which a newborn magnetar may be present, making them particularly interesting targets for the directed long-transient gravitational-wave searches considered in this thesis.

The luminosity, breakout time, duration, and temperature of the magnetar-driven SBO depend on the rate at which rotational energy is injected into the ejecta. Within the model adopted here, this dependence is controlled primarily by the initial spin period P and dipole magnetic field strength B, together with the supernova ejecta mass and explosion energy. Therefore, a well-sampled UV light curve, especially when combined with information on the supernova ejecta, can constrain the region of (B, P) parameter space compatible with the observed transient. This makes it a useful probe of the physical conditions immediately following the magnetar birth.

5.2 SBO model and light curves

A newly born millisecond spinning magnetar, with angular velocity $\Omega = 2\pi/P$ and moment of inertia I, has the rotational energy

$$E_{\rm rot} = \frac{1}{2} I \Omega^2 \approx 3 \times 10^{52}\ P_{\rm ms}^{-2} M_{1.4} R_{12}^2\ {\rm erg}\,, \tag{5.1}$$

where $P_{\rm ms}$ is the spin period in milliseconds, $M_{1.4}$ is the neutron star mass in units of $1.4\,M_\odot$, and R_{12} is the radius in units of 12 km. The magnetar loses rotational energy through magnetic dipole radiation. The corresponding spin-down timescale is ([124])

$$t_m = \frac{I c^2}{2\mu^2 \Omega^2} \approx 7 \times 10^4\ \left(\frac{P_{\rm ms}}{B_{14}}\right)^2 \frac{M_{1.4}}{R_{12}^4}\ {\rm s}\,, \tag{5.2}$$

where μ is the magnetic dipole moment of the magnetar, B_{14} is the dipole magnetic field strength in units of 10^{14} G. This expression assumes an aligned dipole rotator in vacuum.

The corresponding spin-down luminosity is

$$L_m = \frac{E_{\rm rot}/t_m}{(1 + t/t_m)^2} \sim 10^{47}\ \frac{E_{{\rm rot},52}}{t_{m,5}}\,(1 + t/t_m)^{-2}\ {\rm erg\ s^{-1}}\,. \tag{5.3}$$

The spin-down luminosity supplies the magnetar wind described in Sec. 5.1, whose pressure drives a shock through the expanding supernova ejecta. We model the evolution of this interaction following the prescription of [40], adopting a characteristic explosion energy of 10^{51} erg.

The density profile within the ejecta shell can be approximated by a broken power-law, which is shallow in the inner region and becomes very steep close to the surface,

$$\rho(r,t) = \begin{cases} \zeta_\rho \dfrac{M_{SN}}{v_t^3 t^3} \left(\dfrac{r}{v_t t}\right)^{-\delta} & \text{if } v < v_t \\ \zeta_\rho \dfrac{M_{SN}}{v_t^3 t^3} \left(\dfrac{r}{v_t t}\right)^{-n} & \text{if } v \geq v_t\,, \end{cases} \tag{5.4}$$

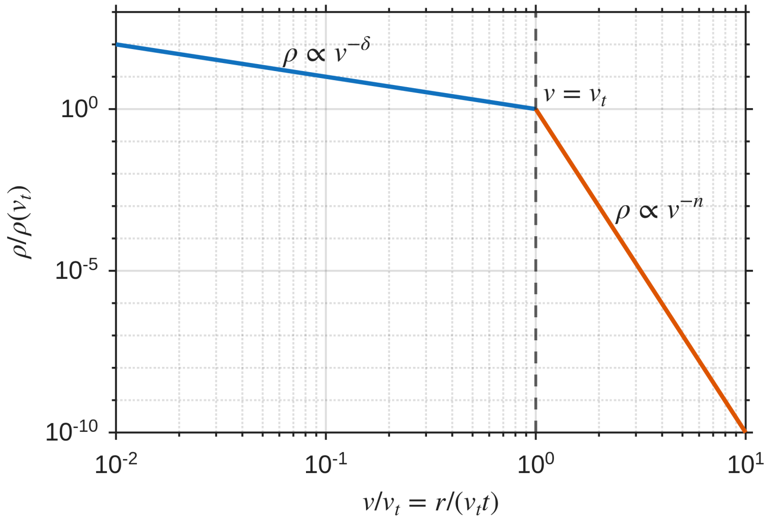

Figure 5.2. Dimensionless broken power-law density profile of the supernova ejecta described by Eq. 5.4, shown for the representative values $\delta = 1$ and $n = 10$. The density decreases relatively slowly in the inner ejecta ($v < v_t$) and steeply in the outer ejecta ($v \geq v_t$). The vertical dashed line marks the transition velocity $v = v_t$.

with the transition occurring at the velocity coordinate

$$v_t \approx 3 \times 10^8 \, \zeta_v \left(\frac{E_{SN,51}}{M_{SN}/5M_\odot} \right)^{1/2} \text{ cm s}^{-1} \tag{5.5}$$

for an homologous expansion of the shell. Here E_{SN} and M_{SN} are initial kinetic energy of the SN ejecta and ejecta mass respectively. Typical values for core-collapse supernovae are $\delta \approx 1$ and $n \approx 10$ [125], while

$$\zeta_v = \frac{2(5-\delta)(n-5)}{(n-3)(3-\delta)}^{1/2} \tag{5.6}$$

$$\zeta_\rho = \frac{(n-3)(3-\delta)}{4\pi(n-\delta)} \, . \tag{5.7}$$

Figure 5.2 illustrates the resulting broken power-law structure for the representative values $\delta \approx 1$ and $n \approx 10$, highlighting the shallow inner profile and the much steeper decline in the outer ejecta.

By using the mass, momentum, and energy equations for the shock ([40]), we can determine its radius $r_{\rm s}$ as a function of time

$$r_{\rm s}(t) = v_t t_{\rm tr}^{1-\alpha} t^\alpha \tag{5.8}$$

$$\alpha = \begin{cases} 5/4 & \text{if } v < v_t \\ 3/2 & \text{if } v \geq v_t \, , \end{cases} \tag{5.9}$$

where $t_{\rm tr}$ is the time it takes for the shock to propagate through the inner ejecta,

$$t_{\rm tr} = \zeta_{\rm tr}(E_{SN}/E_{\rm rot}) t_m \tag{5.10}$$

$$\zeta_{\rm tr} = \frac{2(n-5)(9-2\delta)(11-2\delta)}{(5-\delta)^2(n-\delta)(3-\delta)}\,. \tag{5.11}$$

Inside the shock, energy is dissipated at the rate $\dot{\epsilon}_{\rm sh}$

$$\dot{\epsilon}_{\rm sh} = 4\pi r_{\rm s}^2 \frac{\rho}{2} v_{\rm ej}^3 \eta^3\,, \tag{5.12}$$

where $v_{\rm ej} = r_{\rm s}/t$ is the ejecta velocity at radius $r_{\rm s}$ and η is the shock strength parameter

$$\eta(t) = \frac{v_{\rm s} - v_{\rm ej}}{v_{\rm ej}} = \frac{t}{r_{\rm s}}\left(\frac{dr_{\rm s}}{dt} - \frac{r_{\rm s}}{t}\right)\,, \tag{5.13}$$

v_s being the shock velocity.

Fig. 5.3 depicts the time evolution of the shock heating rate for selected values of the magnetar spin period and magnetic dipole field .

Shock breakout occurs when the optical depth ahead of the shock satisfies $\tau \sim c/v_s$. At this point, radiation can escape efficiently from the outer ejecta layers. This shock breakout happens at radius

$$r_{\rm bo} = v_t t \left(\frac{t_d}{\sqrt{n-1}t}\right)^{2/(n-2)}\,, \tag{5.14}$$

where t_d is the effective diffusion time,

$$t_d = \sqrt{\frac{\zeta_\rho \kappa M_{SN}}{v_t c}}\,, \tag{5.15}$$

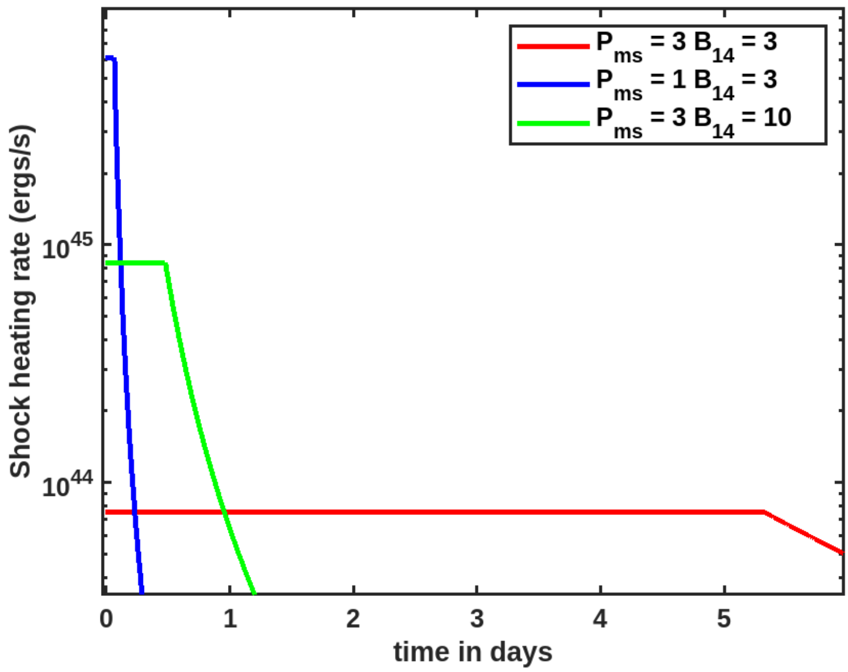

Figure 5.3. Shock heating rate, $\dot{\epsilon}_{\rm sh}$ vs. time (Eq. 5.12) for fiducial parameter values of the SN ejecta ($E_{SN} = 10^{51}$ erg, $M_{SN} = 5M_\odot$) and three sets of (P, B)-values for the magnetar central engine, as indicated in the legend

and $\kappa = 0.1$ cm^2 g^{-1} the opacity of the ejecta material.

Equating the breakout radius $r_{\rm bo}$ to the shock radius r_s, we obtain the SBO time $t_{\rm bo}$,

$$t_{\rm bo} \approx \left[\frac{\zeta_{\rm tr}^{1-\beta}}{(n-1)^{\beta/2}}\right] t_d^{\beta} t_m^{1-\beta} (E_{SN}/E_{\rm rot})^{1-\beta} \tag{5.16}$$

with

$$\beta = \frac{2}{(\alpha-1)(n-2)+2}\,. \tag{5.17}$$

Most of the radiation will escape from the region where the photon optical depth $\tau \approx 1$, which defines the photospheric radius,

$$r_p = 1.2 v_t t_d \left(\frac{t_{\rm bo}}{t_d}\right)^{(n-3)/(n-1)}\,. \tag{5.18}$$

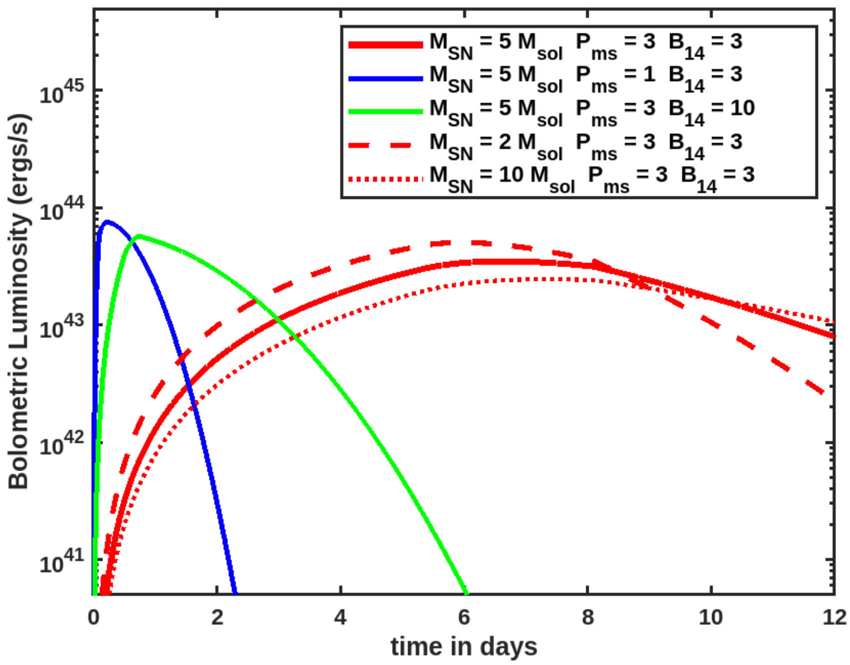

Figure 5.4. Bolometric SBO luminosity $L_{\rm sbo}(t)$ (Eq. 5.19) for the same set of parameters as in the Fig. 5.3. The dashed and dot-dashed red curves are for the same magnetar as the solid red curve, but for different ejecta masses: 2 $M_\odot$ (dashed) or 10 $M_\odot$ (dot-dashed). The impact of changing the ejecta mass is substantially smaller than that of different magnetar parameters, to which our model is much more sensitive. In particular, while the (bolometric) peak luminosity has a moderate dependence on the magnetar spin and B-field, the light curve evolution and peak time are strongly dependent on these parameters. For reference the peak time of the blue, green and red solid curves are, respectively, $\approx 0.2, 0.7$ and 5.5 days. The explosion energy is fixed at $E_{\rm SN} = 10^{51}$ erg in all cases shown.

The resulting luminosity evolution is ([40])

$$L_{\rm sbo}(t) \approx e^{-\left(\frac{t}{t_{\rm bo}}\right)^2} \int_0^t 2\dot{\epsilon}_{sh}(t') \frac{t'}{t_{\rm bo}^2} e^{\left(\frac{t'}{t_{\rm bo}}\right)^2} dt' \,. \tag{5.19}$$

Equation 5.19 gives the time evolution of the bolometric SBO luminosity. Fig. 5.4 shows the SBO bolometric luminosity for selected values of the magnetar spin period and magnetic dipole field (see caption for details). We verified that the SBO lightcurve peak corresponds approximately to the shock heating rate at the SBO time, $t_{\rm bo}$, and can therefore be expressed as

$$L_{\rm sbo}^{\rm peak} \approx 9 \frac{E_{SN}}{t_d} \eta^3 \left(\frac{t_m}{t_d} \frac{E_{SN}}{E_{\rm rot}} \right)^{(n-8)(1-\beta)/(n-2)} \,. \tag{5.20}$$

5.3 ULTRASAT and UV observations

ULTRASAT is a planned space telescope designed for time-domain observations in the near-ultraviolet (NUV) band (230-290 nm). It is expected to be launched to a geostationary orbit and will operate as a wide-field survey mission for transient and variable sources. The main feature of ULTRASAT is its very large field of view of about 204 deg^2, which allows it to monitor a significant fraction of the sky at any given time [42, 123].

A key capability of ULTRASAT is its fast response and high cadence observing strategy. The satellite will be able to generate transient alerts within minutes after observations, allowing rapid follow-up from ground-based telescopes. In addition, it will continuously monitor selected sky regions with minute-scale cadence, which is crucial for capturing short-lived phases such as shock breakout emission.

ULTRASAT will be able to observe early UV emission from explosive events such as core-collapse supernovae. ULTRASAT is also highly relevant for multi-messenger astronomy. Its wide field of view and fast sky coverage make it well suited to search for electromagnetic counterparts of gravitational-wave events.

For core-collapse supernovae, ULTRASAT is expected to detect a large number of events very early after explosion, often within hours. This makes it an ideal instrument for studying the early evolution of the supernova light curve. In the case of magnetar-powered explosions, ULTRASAT can capture the early UV signal produced when the magnetar-driven shock breaks out of the expanding ejecta, providing a direct probe of the central engine activity.

Overall, ULTRASAT will significantly improve our ability to study the early ultraviolet sky, enabling studies of early emission phases that are difficult to access with current optical surveys.

5.4 Peak luminosity in the ULTRASAT band and detection horizon

The fraction of shock breakout emission that falls within the ULTRASAT observing band (230-290 nm) can be estimated by assuming that the emission is approximately thermal. In this case, the spectrum is described by a blackbody with temperature $T_{\rm bb}$.

The SBO peak luminosity in the ULTRASAT band, $L_{\rm UV}^{\rm peak}$, can be expressed as a fraction $f_{\rm UV}$ of the bolometric SBO peak luminosity, $L_{\rm sbo}^{\rm peak}$,

$$L_{\rm UV}^{\rm peak} = f_{\rm UV} L_{\rm sbo}^{\rm peak}. \tag{5.21}$$

The fraction $f_{\rm UV}$ is estimated from the blackbody spectrum as

$$f_{UV} = \frac{\displaystyle\int_{\lambda_{\rm min}/(1+z)}^{\lambda_{\rm max}/(1+z)} B_\lambda(T_{\rm bb})\, d\lambda}{\sigma T_{\rm bb}^4}\,, \tag{5.22}$$

where $B_\lambda(T_{\rm bb})$ is the spectral radiance per unit wavelength, while $\sigma T_{\rm bb}^4$ represents the total bolometric flux of the blackbody with σ the Stefan-Boltzmann constant and $T_{\rm bb}$ the blackbody temperature. The limits of the integral are divided by $(1+z)$ because the observed wavelength range is redshifted with respect to the source frame. Thus, $f_{\rm UV}$ gives the fraction of the thermal emission falling within the wavelength range corresponding to the ULTRASAT observing band and depends on both $T_{\rm bb}$ and z.

The blackbody temperature $T_{\rm bb}$ is determined by the SBO luminosity and the photospheric radius through the relation

$$L_{\rm sbo}^{\rm peak} = 4\pi r_p^2 \sigma T_{\rm bb}^4. \tag{5.23}$$

Both $L_{\rm sbo}^{\rm peak}$ and r_p are set by the magnetar and supernova parameters, as described in Eqs. 5.20 and 5.18. Therefore, the UV emission depends ultimately on the magnetar spin period P, magnetic field B, and the ejecta properties $E_{\rm SN}$ and $M_{\rm SN}$.

Figure 5.5 summarizes these model quantities across the (B, P) parameter space for fixed ejecta parameters $E_{\rm SN} = 10^{51}$ erg and $M_{\rm SN} = 5\,M_\odot$. The figure shows how the magnetar parameters determine the SBO peak luminosity, photospheric radius, and effective temperature, which in turn set the fraction of the emission falling within the ULTRASAT band.

Once the UV luminosity is known, we can estimate whether the event is detectable by ULTRASAT. The sensitivity of an astronomical telescope is commonly expressed in terms of apparent magnitude, which measures how bright a source appears to an observer. ULTRASAT is expected to reach a limiting magnitude of 22.4 AB mag in the 230-290 nm band [42], with smaller magnitudes corresponding to brighter sources.

The source luminosity cannot be compared directly with this limiting magnitude because luminosity is an intrinsic property of the source, whereas apparent magnitude depends on the flux received by the observer. We therefore first express the predicted UV emission as an absolute magnitude $M_{\rm UV}$ and then determine the luminosity distance at which its apparent magnitude reaches the ULTRASAT detection threshold.

In the calculation adopted here, the bolometric SBO peak luminosity is first expressed as an absolute magnitude,

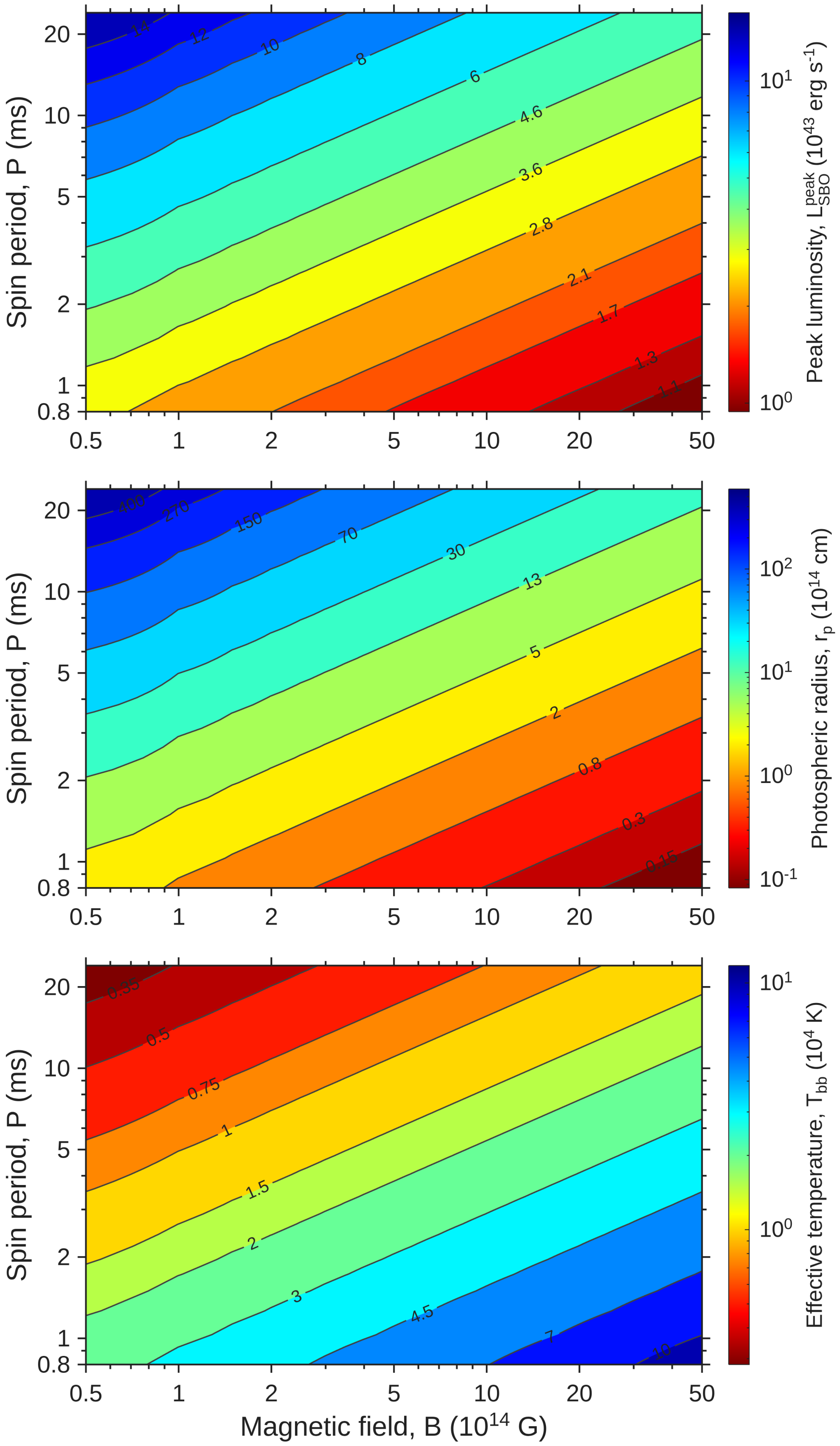

Figure 5.5. *Upper Panel:* the bolometric SBO peak luminosity, $L_{\rm sbo}^{\rm peak}$ in units of 10^{43} erg s^{-1}, as a function of the magnetar parameters (B, P; Eq. 5.20), for fixed ejecta parameters, $E_{SN} = 10^{51}$ erg and $M_{SN} = 5M_\odot$; *Middle Panel:* Photospheric radius, r_p in units of 10^{14} cm, as a function of the magnetar parameters (B, P), and the same ejecta properties as in the upper panel; *Lower Panel:* Effective blackbody temperature, $T_{\rm bb}$ in units of 10^4 K, vs. magnetar parameters as derived from the relation $L_{\rm sbo}^{\rm peak} = 4\pi\sigma r_p^2 T_{\rm bb}^4$, for the same ejecta properties as in the previous panels.

$$M_{\mathrm{bol}} = -2.5 \log_{10}\left(\frac{L_{\mathrm{sbo}}^{\mathrm{peak}}}{L_0}\right), \tag{5.24}$$

where $L_0 = 3.0128 \times 10^{35}\,\mathrm{erg\,s^{-1}}$ is the adopted bolometric luminosity zero point. Using Eq. (5.21), the fraction of the emission falling in the ULTRASAT band then gives

$$M_{\mathrm{UV}} = M_{\mathrm{bol}} - 2.5 \log_{10}(f_{\mathrm{UV}}). \tag{5.25}$$

The corresponding apparent magnitude at luminosity distance D_L is related to M_{UV} through the distance-modulus relation

$$m - M_{\mathrm{UV}} = 5 \log_{10}\left(\frac{D_L}{10\,\mathrm{pc}}\right), \tag{5.26}$$

where D_L is the luminosity distance. Setting $m = m_{\mathrm{lim}} = 22.4$ gives the maximum luminosity distance at which the source can be detected,

$$D_{L,\mathrm{max}} = 10\,\mathrm{pc}\,10^{(m_{\mathrm{lim}} - M_{\mathrm{UV}})/5}. \tag{5.27}$$

The corresponding maximum redshift z_{max} is obtained from the luminosity-distance relation for a spatially flat ΛCDM cosmology,

$$D_L(z) = (1+z)\frac{c}{H_0}\int_0^z \frac{dz'}{\sqrt{\Omega_{\mathrm{M}}(1+z')^3 + \Omega_\Lambda}}, \tag{5.28}$$

by solving

$$D_L(z_{\mathrm{max}}) = D_{L,\mathrm{max}}. \tag{5.29}$$

Thus, for each combination of $(B, P, E_{\mathrm{SN}}, M_{\mathrm{SN}})$, the model determines $L_{\mathrm{sbo}}^{\mathrm{peak}}$, T_{bb} and the fraction of the emission falling in the ULTRASAT band, from which the corresponding $D_{L,\mathrm{max}}$ and z_{max} are calculated. In the calculations presented here, the explosion energy is fixed to $E_{\mathrm{SN}} = 10^{51}\,\mathrm{erg}$, while the effect of varying the ejecta mass is explored explicitly. As shown in Fig. 5.4, changes in M_{SN} over the range considered produce a more moderate variation of the light curve than changes in the magnetar spin period and magnetic field. This results in a similarly weak dependence of the detection horizon on M_{SN}.

A broader exploration of the supernova explosion parameters is beyond the scope of the present study. In particular, different stellar progenitors, such as red supergiants, blue supergiants, or Wolf-Rayet stars, may lead to different explosion energies, which can modify the SBO luminosity, timescale, and detection horizon. Exploring this wider progenitor and explosion parameter space will be an important extension of this work.

So far, we have not included absorption and scattering of UV photons by dust in the host galaxy. This effect can significantly reduce the observed flux, especially in the ultraviolet. To include this in a simplified way, we adopt an average extinction value of $A_{\mathrm{NUV}} \sim 1.75$ mag. This is based on previous UV observations of supernova-like transients using missions such as *Swift*/UVOT and GALEX [126]. The extinction is included in magnitude space by increasing the apparent magnitude of the source according to

$$m_{\rm ext} = m + A_{\rm NUV}, \tag{5.30}$$

where m is the apparent magnitude in the absence of extinction and $m_{\rm ext}$ is the corresponding extincted magnitude. When determining the detection horizon, the limiting magnitude available for the intrinsic source emission becomes $m_{\rm lim} - A_{\rm NUV}$. The maximum luminosity distance including extinction is therefore

$$D_{L,\rm max}^{\rm ext} = 10\,{\rm pc}\,10^{(m_{\rm lim}-A_{\rm NUV}-M_{\rm UV})/5}. \tag{5.31}$$

Since extinction makes the source appear fainter, the corresponding maximum luminosity distance and maximum redshift are reduced. The adopted value represents an average correction; the actual UV extinction can vary substantially between

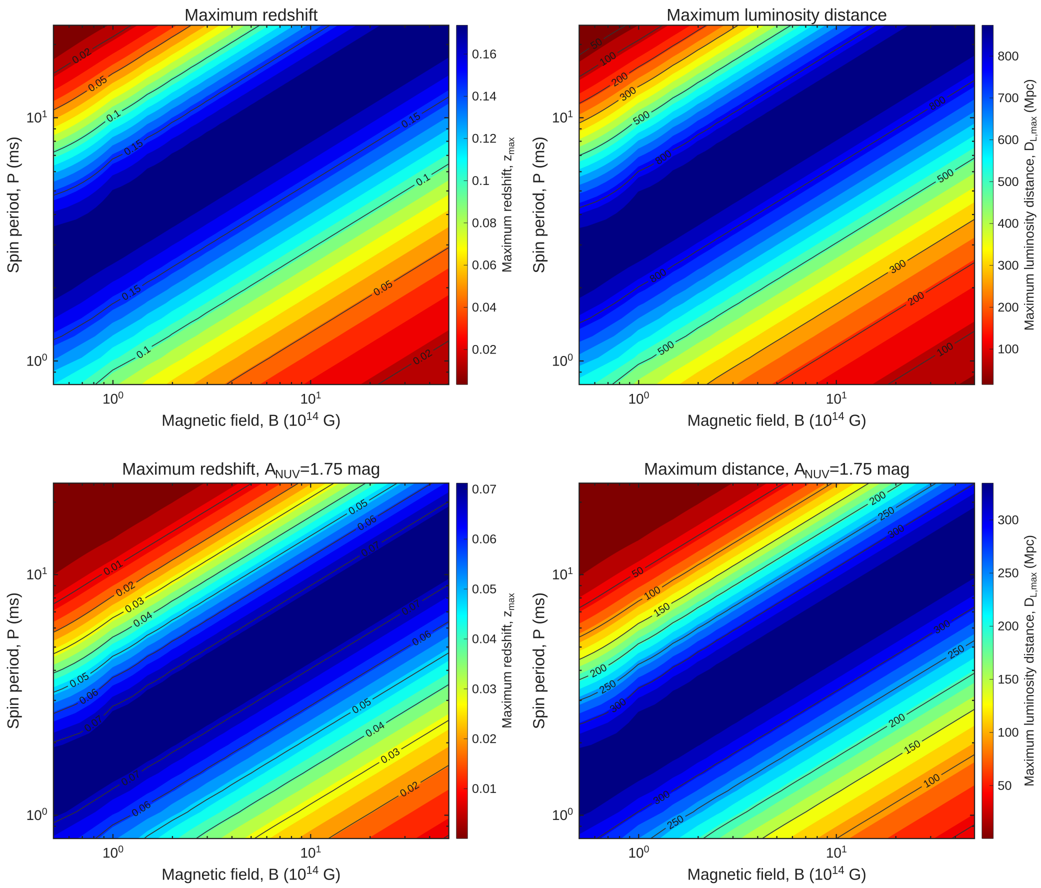

Figure 5.6. ULTRASAT detection horizon for magnetar-driven shock breakouts as a function of the magnetar parameters (B, P), for fiducial ejecta properties $E_{\rm SN} = 10^{51}$ erg and $M_{\rm SN} = 5\,M_{\odot}$. *Upper row:* results without UV extinction. *Lower row:* results including the representative extinction $A_{\rm NUV} = 1.75$ mag. In each row, the left panel shows the maximum detectable redshift $z_{\rm max}$, while the right panel shows the corresponding maximum luminosity distance $D_{L,\rm max}$ in Mpc.

individual events depending on the properties of the host galaxy and the line of sight.

Figure 5.6 shows the resulting ULTRASAT detection horizon as a function of the magnetar parameters (B, P). The horizon is shown both as the maximum detectable redshift $z_{\rm max}$ and as the corresponding maximum luminosity distance $D_{L,\rm max}$. The upper panels show the results without UV extinction, while the lower panels include the representative extinction $A_{\rm NUV} = 1.75$ mag.

5.5 Expected event rate

Our results show that magnetar-driven shock breakouts can be detected by ULTRASAT out to a maximum luminosity distance of roughly $D_{\rm L,max} \approx 300$ Mpc, assuming an average near-ultraviolet extinction of $A_{\rm NUV} = 1.75$ mag. This detection horizon depends strongly on the magnetar properties, in particular the magnetic field strength B and the initial spin period P, since these control the energy available to power the shock breakout emission.

To estimate how many such events ULTRASAT may detect, we need to average the $z_{\rm max}$ distribution (Fig. 5.6) over the probability distribution of magnetar parameters within the population. We therefore use the computed $z_{\rm max}(B, P)$ relation (Fig. 5.6) and integrate it over the allowed range of magnetar magnetic fields and spin periods. We perform this calculation both with and without extinction, in order to quantify how the extinction affects the final detection rate.

The birth distributions of magnetar magnetic fields and spin periods are not well known from observations. For this reason, we adopt simple, agnostic distributions for both parameters that are constant in logarithmic intervals. This corresponds to

$$\mathbb{P}(B) = \frac{k_B}{B}, \quad \mathbb{P}(P) = \frac{k_P}{P}.$$

Here k_B and k_P are normalization constants fixed by the allowed parameter ranges. We later test how sensitive our results are to these assumptions by changing the prior on B.

The expected number of detectable events per year is obtained by integrating over the magnetar parameter space (B, P), redshift (up to $z_{\rm max}$) and the core-collapse supernova rate. For fixed ejecta parameters, as adopted in each calculation below, the expected event rate is

$$\dot{N}_{\rm ev} = \int_{P_{\rm min}}^{P_{\rm max}} dP \int_{B_{\rm min}}^{B_{\rm max}} dB \int_{0}^{z_{\rm max}(B,P,E_{\rm SN},M_{\rm SN})} \mathcal{R}_{\rm mag}(z) \frac{dV}{dz} \mathbb{P}(B)\mathbb{P}(P) dz \tag{5.32}$$

where $\mathcal{R}_{\rm mag}(z)$ is the comoving volumetric formation rate of magnetars. We assume that a fraction $f_{\rm mag} = 0.1$ of core-collapse supernovae produce magnetars [96, 127], so that

$$\mathcal{R}_{\rm mag}(z) = f_{\rm mag}\, \mathcal{R}_{\rm CCSN}(z) = 0.1\, \mathcal{R}_{\rm CCSN}(z). \tag{5.33}$$

The core-collapse supernova rate is written as [128]

$$\mathcal{R}_{CCSN}(z) = k_{\mathrm{CC}} \times \psi(z) \tag{5.34}$$

where the star formation rate density is given by

$$\psi(z) = 0.015 \frac{(1+z)^{2.7}}{1 + \left(\frac{1+z}{2.9}\right)^{5.6}} \ \mathrm{M}_{\odot}\, \mathrm{year}^{-1} \mathrm{Mpc}^{-3} \,,$$

The constant $k_{\mathrm{CC}} = 0.0068\, M_{\odot}^{-1}$ corresponds to the number of core-collapse supernova progenitors per unit stellar mass, assuming a Salpeter initial mass function in the range 8-40 $M_{\odot}$, which produces neutron stars.

The co-moving volume element $dV(z)$ is

$$dV(z) = D_H^3 \frac{d_C^2(z)}{F(z)}\, dz\, d\Omega \,, \tag{5.35}$$

where $D_H = c/H_0$ is Hubble distance and $d\Omega$ is the differential solid angle. Integrating over the full sky gives $\int d\Omega = 4\pi$, and therefore

$$\frac{dV}{dz} = 4\pi \left(\frac{c}{H_0}\right)^3 \frac{d_C^2(z)}{F(z)}. \tag{5.36}$$

Here $d_C(z)$ is the proper distance at redshift z,

$$d_C(z) = \int_0^z \frac{1}{F(z')}\, dz', \tag{5.37}$$

and $F(z)$ describes the cosmological expansion

$$F(z) = \sqrt{\Omega_M (1+z)^3 + \Omega_k (1+z)^2 + \Omega_\Lambda} \,. \tag{5.38}$$

We adopt standard Planck cosmological parameters [129]: $\Omega_M = 0.685$, $\Omega_\Lambda = 0.315$, and $\Omega_k = 0$.

Plugging everything into Eq. 5.32 we finally obtain

$$\begin{aligned} \dot{N}_{\mathrm{ev}} = 4\pi f_{\mathrm{mag}} k_{\mathrm{CC}} k_B k_P \left(\frac{c}{H_0}\right)^3 \int_{P_{\mathrm{min}}}^{P_{\mathrm{max}}} \frac{dP}{P} \int_{B_{\mathrm{min}}}^{B_{\mathrm{max}}} \frac{dB}{B} \\ \times \int_0^{z_{\mathrm{max}}(B,P,E_{\mathrm{SN}},M_{\mathrm{SN}})} \frac{\psi(z) d_C^2(z)}{F(z)}\, dz. \end{aligned} \tag{5.39}$$

where $k_B = [\log(B_{\mathrm{max}}/B_{\mathrm{min}})]^{-1} \approx 0.217$ and $k_P = [\log(P_{\mathrm{max}}/P_{\mathrm{min}})]^{-1} \approx 0.294$. Here $f_{\mathrm{mag}} = 0.1$ explicitly accounts for the assumed fraction of core-collapse supernovae that form magnetars.

We choose the range of spin periods as 0.8-24 ms and dipole B-fields as $(0.5 - 50) \times 10^{14}$ G. The calculation is performed for different assumed ejecta masses and extinction values, which modify the detection horizon entering the upper limit of the redshift integral in Eq. (5.39).

Using these assumptions, we obtain from Eq. 5.39 $\dot{N}_{\rm ev} \approx (3-30)\ {\rm yr}^{-1}$, depending on the amount of extinction ($A_{NUV} = 0 - 1.75$ mag) and on the ejecta mass ($M_{SN} = 5 - 10 M_{\odot}$). This result shows that extinction is one of the main factors limiting detectability in the ultraviolet, while the ejecta mass plays a secondary role compared to the magnetar parameters.

Assuming that about 10% of all core-collapse supernovae produce magnetars, we find that for low extinction ($A_{\rm NUV} \lesssim 0.8$ mag), magnetar-powered SBOs may represent roughly $\sim 10 - 20\%$ of all ULTRASAT SBO detections. On the other hand, for higher extinction ($A_{\rm NUV} = 0.8$-1.75 mag), this fraction drops to about $\sim 2 - 10$ %.

To test the robustness of our results, we repeat the calculation using a Gaussian prior for the magnetic field distribution, centered at $B_{0,14} = 5$ with a standard deviation of $\sigma_{B,14} = 2.5$ in order to reproduce the B-range for known magnetars within a 3σ interval. For the spin period, we keep the log-uniform distribution, since current observations suggest a broad distribution peaking at a few milliseconds.

With these modified assumptions, the expected detection rate for magnetar-powered SBOs becomes in this case $\sim (2 - 20)\ {\rm yr}^{-1}$, showing that our prediction is robust with respect to the prior.

The spin period and magnetic field are the key parameters controlling both the luminosity and the timescale of magnetar-driven SBOs. As shown in Section 5.2, they directly shape the shock evolution and therefore the observable light curve. As a result, ULTRASAT detections can therefore provide crucial evidence for the presence of a magnetar central engine, and constrain its spin energy and magnetic field. Other model parameters that may affect the light curve shape, peak luminosity and overall detectability are the explosion energy and ejecta mass. In this first study we have assumed fiducial values for both parameters, and showed that the ejecta mass may only have a moderate impact on the lightcurve peak (Fig. 5.4), hence on the detectability of the UV SBO. A more complete exploration of the explosion parameter space will be addressed in future work.

5.6 Multi-messenger implications

Magnetar-powered shock breakouts provide an important electromagnetic trigger for gravitational-wave searches. As discussed in Chapter 3, newly born rapidly rotating magnetars are expected to emit long-duration GW signals due to non-axisymmetric deformations and spin evolution. However, these signals are generally weak and difficult to detect without prior information on the source time and sky position.

In this context, an early ultraviolet detection of a shock breakout with ULTRASAT can significantly improve the sensitivity of directed GW searches. The SBO provides a precise explosion time and sky localization, which allows GW data to be analysed in a much narrower time window and parameter space compared to blind all-sky searches.

For nearby events (within approximately ~ 5 Mpc), such triggered searches could be performed with current-generation detectors such as LIGO, Virgo, and KAGRA during their O5 observing run. ULTRASAT can act as a timing and localisation instrument that enables a more focused GW analysis. For next-generation detectors such as the Einstein Telescope, the improved sensitivity could extend the joint detection range to distances of order $\sim$ 35-40 Mpc [38].

Beyond detection prospects, the combination of electromagnetic and gravitational-wave information can also provide stronger constraints on the physical properties of the system. The SBO light curve gives information on the magnetar spin period, magnetic field strength, and ejecta properties, providing critical input for GW waveform modeling. These early EM observations thus complement the long-duration GW signals and enable robust multi-messenger astrophysical studies.

Overall, magnetar-powered SBOs provide a connection between electromagnetic and gravitational-wave observations. They offer a way to identify the birth of a compact object in real time and to study its early evolution using multiple messengers. This makes them a promising target for future multi-messenger searches aimed at understanding neutron star formation and the physics of core-collapse explosions.

Chapter 6

Long Transient Search Methods

Searches for long-transient gravitational waves require analysis techniques capable of tracking signals whose frequency evolves significantly over time while maintaining computational feasibility. Fully coherent matched-filter searches provide optimal sensitivity but become computationally not feasible as the signal duration extends over many hours or days and the parameter space is large. Semi-coherent methods offer a practical compromise between sensitivity and computational cost. These approaches divide the data into shorter segments that are analyzed coherently, while the results from different segments are combined incoherently.

In this work we employ a semi-coherent pipeline based on the Generalized Frequency Hough Transform (GFH) [32], specifically the improved GFH-v2 implementation [34]. The method assumes that the sky position of the source and an approximate signal onset time are known from electromagnetic observations, such as the early shock-breakout discussed in Chapter 5. The method is designed to detect signals from rapidly evolving sources, such as newly born neutron stars or magnetars, whose frequency evolution follows a power-law decay.

This chapter introduces the main components of the long-transient search framework. It begins with the semi-coherent search strategy and the preparation of detector data starting from the Short Fourier Transform Database (SFDB) [130, 131]. The construction of the time-frequency peakmap is then presented, followed by the application of the Frequency Hough transform [31] and its extension to the Generalized Frequency Hough. The procedure used to construct the parameter-space grids, identify significant candidates, and perform coincidence tests between detectors is also described. Finally, the theoretical framework used to estimate the sensitivity of the search is presented.

6.1 Search strategies for long-transient gravitational waves

The choice of a GW search strategy mainly depends on how much information is available about the source before analysis. The less information is known in advance, the larger the parameter space that must be explored and the higher the computational cost of the search.

A fully coherent search, which preserves the phase information of the signal over the entire observation time, provides the highest sensitivity. However, for long-duration signals with uncertain frequency evolution, the number of templates required to cover the parameter space is very high and makes fully coherent searches computationally not feasible [17, 132]. For this reason, searches are commonly divided into three broad categories [16, 133]:

Targeted searches

Targeted searches are applied when the source position and frequency evolution are already known with high precision from electromagnetic observations. In this case the expected signal evolution is well constrained and the data can be integrated coherently over long time intervals, thus maximizing sensitivity. This strategy is typically used for known pulsars with well-known positions and spin information.

Directed searches Directed searches are used when the sky position of the source is known but the GW frequency evolution is uncertain or unknown. In this case, the search must explore a range of frequencies and signal evolution parameters while keeping the source location fixed. Compared to targeted searches, this increases the computational cost. Fully coherent directed searches can be performed when the observation time and parameter space are sufficiently limited, whereas for longer data sets or broader parameter spaces the computational cost can become prohibitive, motivating the use of semi-coherent methods. Directed searches are particularly suitable for compact objects associated with electromagnetic transients, such as supernova remnants or newborn neutron stars.

All-sky searches All-sky searches are performed when no prior information is available on either the source position or its signal parameters. The search must therefore cover the entire sky along with a broad range of frequencies and spin-downs. This results in a very large parameter space and a very high computational cost. As a result, fully coherent approaches become impractical and semi-coherent methods are generally adopted.

The search developed in this thesis belongs to the class of directed searches. The sky position and approximate emission time are constrained by electromagnetic observations like Shock-breakout as explained in Chapter 5 while the signal frequency evolution remains unknown and must be explored over a broad parameter space. This motivates the use of the semi-coherent Generalized Frequency Hough method described in the following sections.

6.2 Semi-coherent searches

Semi-coherent searches are widely used in gravitational-wave data analysis whenever the parameter space is sufficiently large that a fully coherent search becomes computationally not feasible [17, 132]. In these methods, the full dataset is divided into shorter segments, each of which is analyzed coherently using techniques such as Fourier transforms. The results from each segment are then combined incoherently, typically using methods such as the Hough transform [134, 135]. Although semi-coherent searches are generally less sensitive than fully coherent approaches, they provide a good compromise between sensitivity and computational cost, making them suitable for all-sky searches and searches covering large frequency and spin-down parameter spaces.

6.3 Data preparation and Short FFT Database

The first step in the Frequency Hough semi-coherent pipeline is the construction of the *Short Fourier Transform Database* (SFDB) [130, 131]. The SFDB stores sequences of short Fourier transforms (SFTs) generated from calibrated gravitational-wave strain data [5, 136].

In the standard construction of the SFDB, the detector time series is divided into partially overlapping segments, typically with a 50% overlap. Each segment has a duration of several thousand seconds and is transformed into the frequency domain using the Fast Fourier Transform (FFT). The overlap of 50% is used in combination with the windowing of the time-domain segments to reduce the effects of segment boundaries and the associated spectral leakage [137]. During the construction of the SFDB, basic data cleaning is also applied to reduce the effect of transient glitches and other disturbances in the data [130]. Further cleaning can be applied later during the extraction of the frequency band of interest or during the construction of the peakmap. The resulting database covers the full analysis frequency band (0 - 2000 Hz).

For the purposes of the GFH search, the SFDB data are first read and restricted to the frequency interval of interest. The selected frequency band is then inverse Fourier transformed to reconstruct a time series containing only the relevant spectral region. This reduced time series is divided again into shorter segments corresponding to the desired analysis coherence time $T_{\rm FFT}$, which is chosen according to the expected signal evolution and is discussed in detail in Sec. 7.1.2. Each segment is Fourier transformed to produce the set of FFTs with a duration appropriate for the analysis, which depends on the signal parameters.

6.4 Peakmap construction

The next stage of the analysis consists of constructing a time-frequency representation of the data known as the *peakmap*. The peakmap identifies the most significant spectral peaks in each FFT segment. For each of the N FFTs, the periodogram, of the i-th FFT is computed as the squared modulus of its Fourier coefficients,

$$S_{P,i}(f_j) = |\tilde{x}_i(f_j)|^2, \tag{6.1}$$

where i labels the FFT segment, j labels the frequency bin, and $\tilde{x}_i(f_j)$ is the Fourier transform of the data in that segment.

Because the detector noise varies with frequency, the periodogram is normalized by an estimate of the local average noise spectrum, $S_{AR,i}(f_j)$, [31]:

$$R(i,j) = \frac{S_{P,i}(f_j)}{S_{AR,i}(f_j)}. \tag{6.2}$$

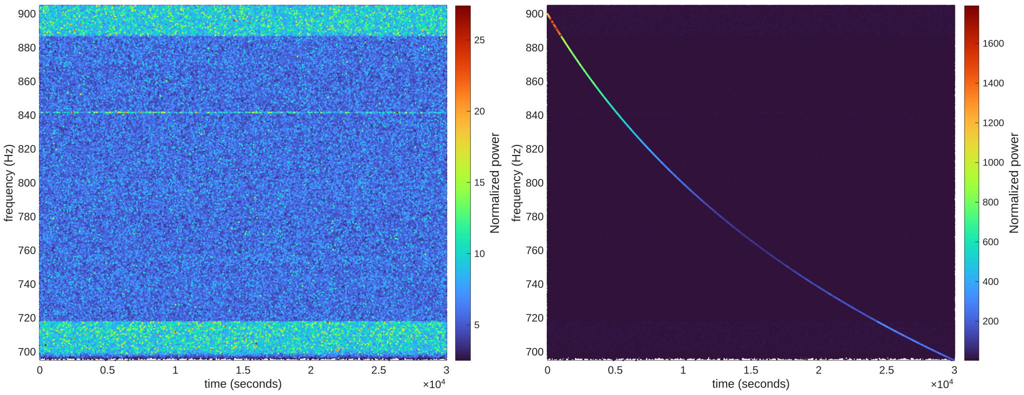

Figure 6.1. Peakmaps constructed from O4a data using the preprocessing described in the text. *Left:* peakmap obtained from noise-only data. *Right:* peakmap obtained after adding a representative simulated long-transient signal generated according to the newborn magnetar signal model described in Chapter 4. The injected signal is chosen to be sufficiently strong for its evolving time-frequency track to be clearly visible. Each point represents a spectral peak that satisfies both the normalized-power threshold and the local-maximum condition.

Here, $S_{AR,i}(f_j)$ provides a local estimate of the noise background around the frequency bin f_j. As commonly done in Frequency Hough and Generalized Frequency Hough analyses, it is estimated from the median spectral power over neighbouring frequency bins, with the appropriate normalization correction for the use of the median. This procedure provides a robust estimate of the local noise level and reduces the influence of isolated spectral outliers [31].

The peakmap is obtained after applying a selection criterion to $R(i,j)$. A frequency bin is retained as a peak only if $R(i,j)$ exceeds a predefined threshold θ and is also a local maximum in frequency. In this work we adopt $\theta = 2.5$, following the standard choice used in Frequency Hough analyses [138]. The additional local-maximum condition is important because it reduces the effect of narrow-band disturbances, which usually affect several neighbouring frequency bins rather than a single one. It also reduces the number of selected peaks, which lowers the computational cost of the Hough analysis.

Each selected peak is represented by its time and frequency coordinates, producing a set of points in the time-frequency plane. The collection of these selected points over all FFT segments forms the peakmap. The peakmap retains the information about possible signal tracks while discarding the majority of noise-dominated data points. These peakmaps forms the input for the Hough-based analysis described in the following sections. An example of the resulting peakmaps is shown in Fig. 6.1, where the effect of a simulated signal injection is shown for a relatively strong (close distance) case to illustrate the signal track clearly.

6.5 Frequency Hough transform

The peakmap described in the previous section provides a time-frequency representation of the data. The next step is to transform these peaks into a parameter space where signal candidates can be more easily identified. This is achieved using the Hough transform, a pattern-recognition technique originally developed for tracking particles in bubble chamber images [139].

In this section, the standard Frequency Hough (FH) [31] transform is introduced as the basis of the methods discussed in this chapter. The FH was adapted for gravitational-wave searches to detect continuous signals from rotating neutron stars whose frequency evolution can be approximated by a linear spin-down, i.e. when higher-order spin-down terms can be neglected over the observation time. Extensions of the method that include second order spin-down terms are possible and are currently being developed. The limitations of the standard FH for rapidly evolving long-transient signals motivate the Generalized Frequency Hough transform discussed in the next section.

Under the linear spin-down approximation, the gravitational-wave frequency can be written as a first-order Taylor expansion around a reference time t_0,

$$f(t) = f_0 + \dot{f}(t - t_0), \tag{6.3}$$

where f_0 is the signal frequency at the reference time and $\dot{f}$ is the spin-down parameter. In this framework, each peak (t, f) in the detector peakmap corresponds to a line in the source parameter space $(f_0, \dot{f})$,

$$\dot{f} = -\frac{f_0}{t - t_0} + \frac{f}{t - t_0}. \tag{6.4}$$

When many peaks originate from the same signal, the corresponding lines intersect in the parameter space at the location corresponding to the true signal parameters. The slope of these lines depends on the choice of the reference time t_0. This reference time is usually chosen at the middle of the observation period, as this reduces parameter uncertainties and limits the spread of the signal across neighboring bins in the Hough map [31]. By counting the number of intersections within each parameter-space bin, a Hough map is constructed in which clusters of high counts indicate candidate signals.

However, this approach assumes that the frequency evolution of the signal is approximately linear over the observation time. While this approximation is valid for continuous wave searches, it breaks down for rapidly evolving sources such as newborn neutron stars or magnetars, whose frequency evolution follows a power-law spin-down. In such cases, a more general formulation is required, motivating the Generalized Frequency Hough transform described in the next section.

6.6 Generalized Frequency Hough transform

To address this limitation , the Generalized Frequency Hough [32] transform introduces a coordinate transformation that linearizes the expected signal trajectory in the time-frequency plane.

For signals whose frequency evolution follows a power-law spin-down characterized by a braking index n, the frequency evolution can be written as

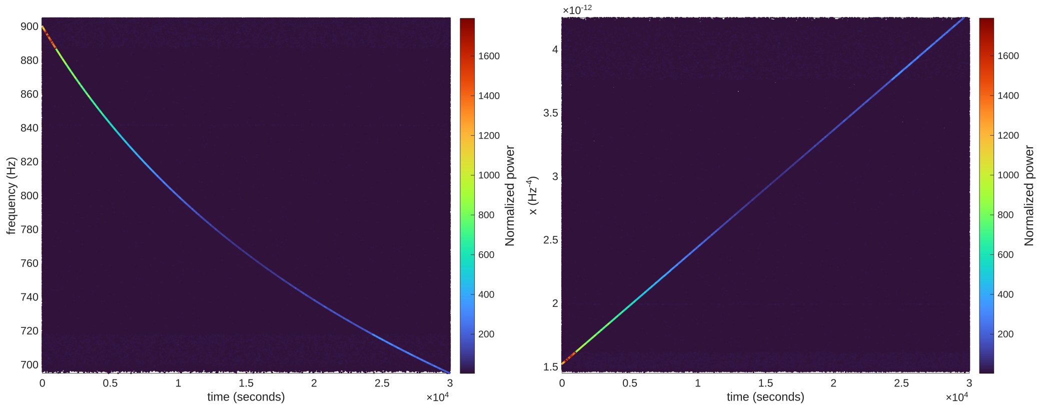

Figure 6.2. Illustration of the coordinate transformation used in the GFH method for O4a data containing an injected long-transient signal. *Left:* original time-frequency peakmap, where the signal appears as a curved track due to its power-law frequency evolution. *Right:* transformed peakmap in the (t, x) plane, with $x = 1/f^{n-1}$, where the same signal is mapped into a straight line. This linearization enables the application of the Hough transform.

$$f(t) = \frac{f_0}{(1 + \frac{t-t_0}{\tau})^{1/(n-1)}}. \tag{6.5}$$

This trajectory becomes linear after introducing the transformed coordinate

$$x = \frac{1}{f^{n-1}}, \quad x_0 = \frac{1}{f_0^{n-1}}. \tag{6.6}$$

In the (t, x) plane the signal trajectory becomes

$$x(t) = x_0 + (n-1)k(t - t_0), \tag{6.7}$$

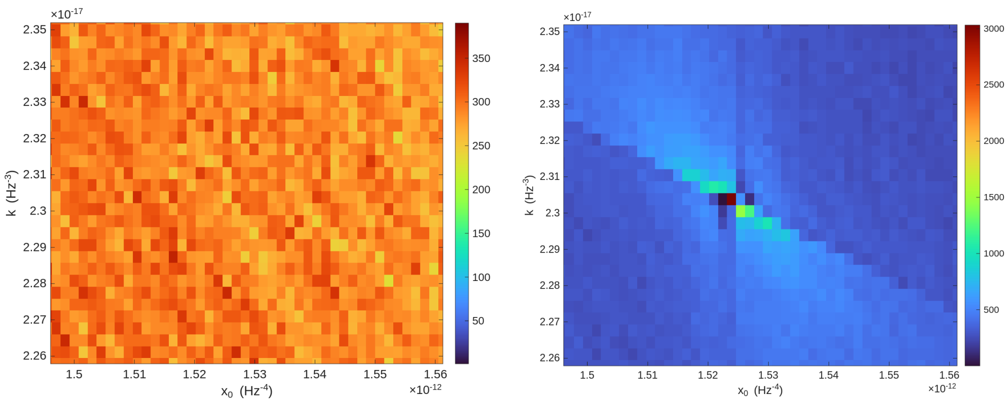

Figure 6.3. Hough maps in the (x_0, k) parameter space obtained from the transformed peakmaps. The color scale represents the number count in each Hough-map bin. *Left:* map constructed from noise-only data, showing no significant accumulation of intersections. *Right:* map obtained in the presence of an injected long-transient signal. The signal produces a clear concentration of intersections in parameter space, appearing as a clear peak that identifies the signal parameters.

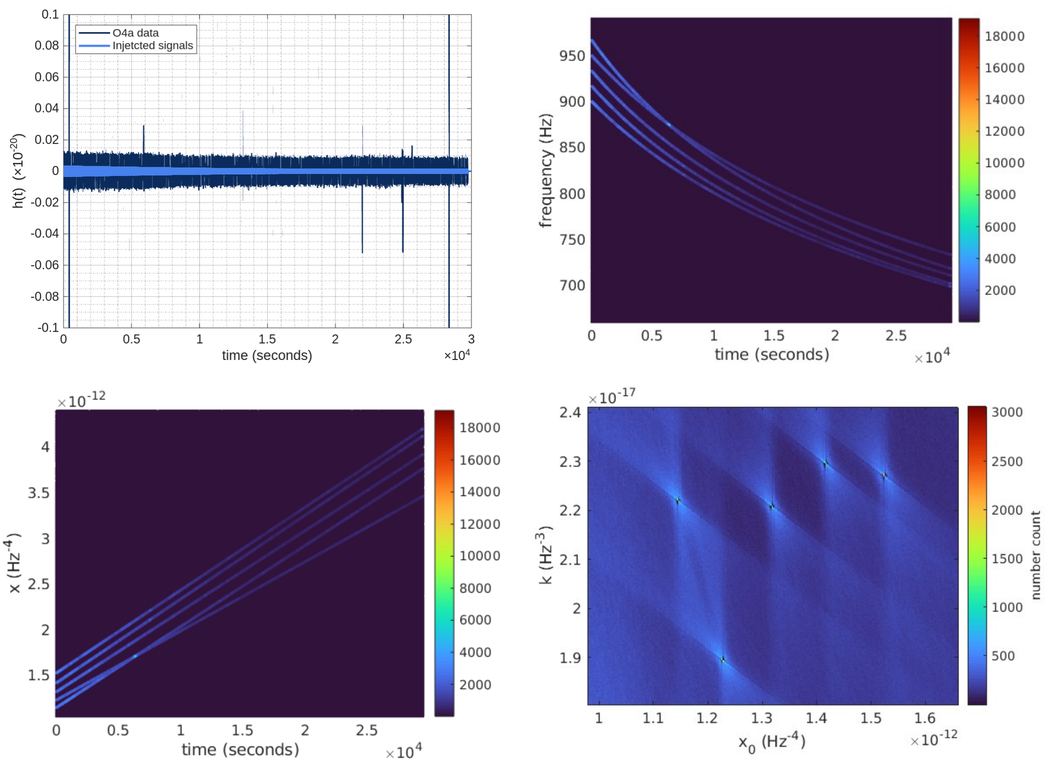

Figure 6.4. Workflow of the GFH transform. *Top left:* Raw strain data with injected signals. *Top right:* Original time-frequency peakmap. *Bottom left:* Coordinate-transformed peakmap, where signal trajectories become linear; color indicates normalized power of the peaks (applies also to the original peakmap above). *Bottom right:* Resulting Hough map, corresponding to 5 simulated signals injected in O4a LIGO Livingston data [63, 140] with $f_0 = 900$-1000 Hz, $\epsilon = (2.5\text{-}3) \times 10^{-3}$, at a distance of 0.1 Mpc and sky location of SN2023ixf.

This transformation converts the curved signal tracks present in the original peakmap into straight lines as shown in the Fig. 6.2, enabling the application of the Hough transform.

Each peak (t, x) in the transformed peakmap is mapped into a line in the (x_0, k) parameter space,

$$k = -\frac{x_0}{(n-1)(t-t_0)} + \frac{x}{(n-1)(t-t_0)}. \tag{6.8}$$

As in the standard FH method, a true signal produces a concentration of intersections in the (x_0, k) parameter space, as shown in Fig. 6.3.

An example of the full GFH workflow is shown in Fig. 6.4. The upper panels display the input strain and its corresponding original peakmap, while the lower panels show the coordinate-transformed peakmap and the resulting Hough map where the clusters indicate potential signal candidates. The clusters appear slanted because the reference time t_0 is set at the start of the dataset.

6.6.1 Grid on parameters

The Hough map is constructed on a discrete grid in the parameter space (x_0, k), where x_0 describes the initial frequency of the signal in the transformed domain and k is related to the strength of the spin-down. The choice of the grid spacing is important, as it determines how well the signal is sampled and, at the same time, affects the computational cost of the search.

The grid is built following the procedure described in [32], based on the requirement that the signal should not drift by more than one frequency bin within a single FFT segment. Since the frequency resolution is $\delta f = 1/T_{\rm FFT}$, this condition can be used to derive both δk and δx_0.

Grid on k. The step in k is obtained by requiring that a small change in k does not change the signal evolution more than what corresponds to one frequency bin. Starting from the relation $\dot{f} = -kf^n$, one can derive the following expression for the step size:

$$\delta k = k \left[\left(1 + \frac{\delta f}{f_{\rm max}} \right)^{-n} - 1 \right]. \tag{6.9}$$

Since $\delta f \ll f_{\rm max}$, this can be approximated as:

$$\delta k \simeq -nk \frac{\delta f}{f_{\rm max}}. \tag{6.10}$$

The step δk depends on both k and n, so the grid in k is non-uniform. This is implemented directly: for each value of k, the next grid point is placed at $k + \delta k(k)$, which is straightforward since the grid is constructed sequentially along the k axis. The range of k values is set by the minimum and maximum spin-down considered in the search:

$$k_{\rm min} = \frac{\dot{f}_{\rm min}}{f^n_{\rm max}}, \qquad k_{\rm max} = \frac{\dot{f}_{\rm max}}{f^n_{\rm min}}. \tag{6.11}$$

Grid on x_0. The parameter $x_0 = f_0^{-(n-1)}$ is related to the initial frequency. Its spacing is obtained by propagating the frequency resolution through this transformation. Taking the derivative, one finds:

$$\delta x_0 = (n-1) \frac{\delta f}{f^n}. \tag{6.12}$$

This step depends on frequency f, so in principle a non-uniform grid in x_0 would also be required. However, unlike the k grid, which is constructed sequentially and can accommodate a variable step naturally, a non-uniform grid in x_0 would prevent filling all x_0 bins simultaneously when constructing the Hough map - a key feature that makes the transform computationally efficient [32]. For this reason, a constant step is used, chosen by evaluating the expression at the maximum frequency in the band,

$$\delta x_0 = (n-1) \, \frac{\delta f}{f^n_{\rm max}}. \tag{6.13}$$

This ensures that the grid is fine enough over the whole frequency range. Although this increases the number of bins at lower frequencies, it does not significantly affect the computational cost.

With these choices, the (x_0, k) grid provides a good sampling of the parameter space, ensuring that signal tracks are properly reconstructed in the Hough map while keeping the computational cost under control. The number of grid points in a Hough map also gives an indication of the computational size of the search. For a given configuration, the number of points is

$$N_{\text{grid}} = N_{x_0} N_k, \tag{6.14}$$

where N_{x_0} and N_k are the numbers of bins along the x_0 and k directions, respectively. Their values depend on the parameter ranges and resolutions defined above and therefore vary between search configurations. For the configurations considered in this work, a single Hough map typically contains several million grid points, with the exact number depending on the signal parameters and the corresponding frequency band and grid resolution.

6.6.2 Candidate Selection

After constructing the Hough maps, the parameter space is explored in order to identify significant outliers. In order to reduce the impact of non-uniform noise and local disturbances, the Hough map is divided into smaller rectangular regions [31]. This allows candidates to be selected locally, making the procedure more uniform and less sensitive to variations across the map.

Within each region, the bin with the highest number count is selected as a candidate. A second candidate is selected only if it is sufficiently far from the first one (typically by at least 6 bins in x_0), to reasonably select candidates of different origin.

To quantify the significance of each selected bin, we use the critical ratio (CR), defined as:

$$\text{CR} = \frac{y - \mu}{\sigma}, \tag{6.15}$$

where y is the number count in the bin, while μ and σ are the mean and standard deviation of the counts computed in the map. The CR therefore measures how much a given bin stands out with respect to the local noise level.

6.6.3 Coincidences

To reduce the number of false alarms, candidates obtained from different detectors are compared and only those that are consistent across datasets are retained.

Following [31], two candidates are considered coincident if their distance in the (x_0, k) parameter space is smaller than a predefined threshold. This distance is defined as:

$$d_{\text{coin}} = \sqrt{\left(\frac{x_{0,2} - x_{0,1}}{\delta x_0}\right)^2 + \left(\frac{k_2 - k_1}{\delta k}\right)^2}, \tag{6.16}$$

where δx_0 and δk are the grid spacings in the two parameters.

Only those pairs with sufficiently small d_{coin} are retained as coincident candidates, significantly reducing the probability of false detections while preserving sensitivity to true signals.

6.6.4 Follow-up

After the candidate selection and coincidence steps, the remaining candidates are further investigated through a follow-up procedure. The goal of this stage is to refine the candidate parameters and to verify whether they are consistent with a true signal.

The GFH transform provides, for each candidate, an estimate of the main signal parameters: the initial frequency f_0, the spin-down $\dot{f}_0$, the braking index n, and the start time t_0 (in the present study n is fixed to 5). Using these parameters, it is possible to return to the original strain data and correct for the expected phase evolution of the signal.

This correction is performed through a heterodyne procedure, which is a standard technique used in several continuous-wave searches [141]. The strain data $h(t)$ are multiplied by a complex exponential that removes the phase evolution associated with the candidate:

$$\tilde{h}(t) = h(t)\, e^{j\phi_{\text{sd}}(t)}, \tag{6.17}$$

where the phase $\phi_{\text{sd}}(t)$ is given by

$$\phi_{\text{sd}}(t) = 2\pi \int_{t_0}^{t} \frac{f_0}{\left[1 + k(n-1) f_0^{n-1} (t' - t_0)\right]^{\frac{1}{n-1}}}\, dt' + \phi_{t_0}. \tag{6.18}$$

This expression is obtained from the assumed power-law evolution of the signal frequency, $\dot{f} = -k f^n$. Integrating this relation provides the time dependence of the frequency, and a further integration gives the phase evolution. The heterodyne correction removes this phase, effectively transforming the signal into nearly constant-frequency.

In the ideal case, if the signal parameters were known exactly, this procedure would completely remove the frequency evolution. The signal would then appear as a horizontal line in the time-frequency plane, allowing the use of longer FFT durations and improving the frequency resolution.

In practice, however, the parameters obtained from the initial search are affected by the finite resolution of the grid. As a result, the correction is not perfect, and a small residual frequency drift may remain. Still, the signal becomes much more localized in frequency compared to the original peakmap.

This effect is illustrated in Fig. 6.5. The original peakmap (left panel) shows the signal track evolving in frequency over time. After applying the heterodyne correction (right panel), most of this evolution is removed and the signal appears as a nearly horizontal track centered around the initial frequency f_0. The zoomed inset highlights how the signal power is concentrated around the initial frequency f_0 after the correction.

Because the frequency evolution is now reduced, it is possible to increase the FFT duration T_{FFT} in the follow-up stage and thus improving the frequency resolution.

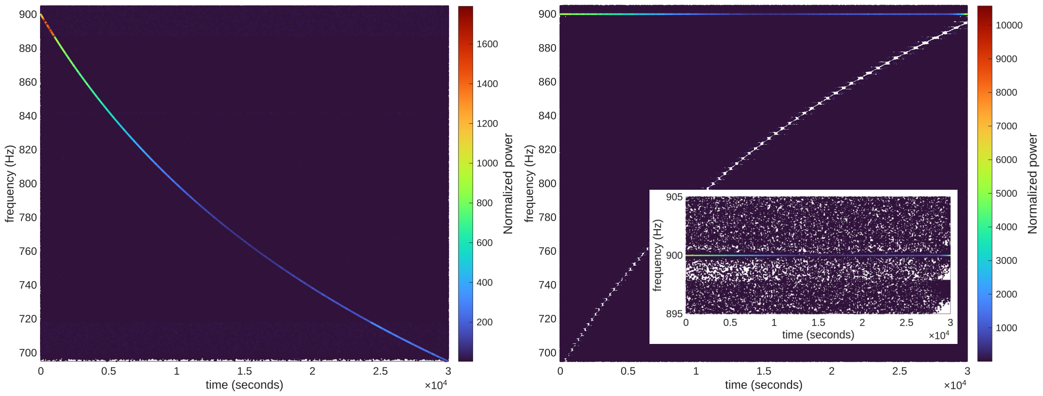

Figure 6.5. Illustration of the heterodyne correction applied during the follow-up stage. Both panels show O4a data containing a representative injected long-transient signal. *Left:* original time-frequency peakmap, where the signal follows a power-law frequency evolution. *Right:* peakmap after applying the heterodyne correction using the estimated signal parameters. The frequency evolution is largely removed, concentrating its power around $f_0 \simeq 900$ Hz, as highlighted in the inset. The additional white curved feature in the corrected peakmap is produced by the heterodyne transformation of a nearly stationary spectral structure near the lower edge of the analyzed band and is unrelated to the injected signal.

The allowed increase in T_{FFT} depends on how well the candidate parameters match the true signal, and therefore a finer grid is constructed around each candidate.

After the phase correction, a new peakmap is generated using the longer T_{FFT}, and a refined Hough transform is applied. Since the residual frequency evolution is small, the standard Frequency Hough transform can be used at this stage.

New candidates are then selected from the refined Hough map and tested for consistency across detectors. If no coincidence is found, the candidate is discarded. Otherwise, the significance of the candidate is evaluated by computing a new critical ratio. The candidate is retained only if the critical ratio increases, otherwise, it is rejected as likely due to noise.

This follow-up step therefore improves the parameter estimation, increases the sensitivity of the search, and reduces the number of false candidates.

6.7 Theoretical sensitivity of the GFH search

The theoretical sensitivity provides an estimate of the minimum signal amplitude that can be detected by the search, or equivalently the maximum distance at which a source can be observed, given the detector noise and the analysis setup.

The derivation follows the general approach used for peakmap-based searches for continuous gravitational waves, as developed in [31] and later extended to long-transient signals in [32]. In this work, we adopt the updated expressions for the peak selection probabilities given in [142], which correct earlier results.

The construction of the peakmap is based on selecting local maxima in the normalized power spectrum that exceed a fixed threshold θ, as described in Sec. 6.4. The first relevant quantity is the probability of selecting a noise peak, denoted by p_0.

Assuming Gaussian noise, the power spectrum follows an exponential distribution, and this probability is

$$p_0 = e^{-\theta} - e^{-2\theta} + \frac{1}{3}e^{-3\theta}. \tag{6.19}$$

In the presence of a signal, the probability of selecting a peak increases slightly. For a weak signal with spectral amplitude λ (expressed in units of the normalized spectrum), this probability can be written as

$$p_\lambda = p_0 + p_1\lambda, \tag{6.20}$$

where p_1 describes how the presence of the signal modifies the peak selection probability. Its expression is

$$p_1 = \theta\left(\frac{1}{2}e^{-\theta} - \frac{1}{2}e^{-2\theta} + \frac{1}{6}e^{-3\theta}\right) + \frac{1}{4}e^{-2\theta} - \frac{1}{9}e^{-3\theta}. \tag{6.21}$$

The quantities p_0 and p_1 determine how efficiently the peakmap captures the presence of a signal.

Following [142], the minimum detectable strain can be written as

$$h_{0,\mathrm{min}} = \mathcal{A}_{\mathrm{min}}\, f_0^2, \tag{6.22}$$

where f_0 is the initial signal frequency.

The coefficient $\mathcal{A}_{\mathrm{min}}$ is given by

$$\begin{aligned} \mathcal{A}_{\mathrm{min}} = \sqrt{\frac{2\pi}{2.4308}}\, \frac{N_{\mathrm{eff}}^{1/4}}{\sqrt{T_{\mathrm{FFT}}}} \left(\frac{p_0(1-p_0)}{p_1^2}\right)^{1/4} \\ \times \left(\sum_{i=1}^{N_{\mathrm{seg}}} \frac{f_i^4\,(F_+A_+ + F_\times A_\times)_i^2}{S_n(f_i)}\right)^{-1/2} \\ \times\sqrt{CR_{\mathrm{thr}} - \sqrt{2}\,\mathrm{erfc}^{-1}(2\Gamma)}. \end{aligned} \tag{6.23}$$

In this expression, T_{FFT} is the duration of each coherent segment, while N_{eff} is the number of effective segments, defined as $N_{\mathrm{eff}} = \frac{T_{\mathrm{obs,eff}}}{T_{\mathrm{FFT}}}$, where $T_{\mathrm{obs,eff}}$ is the total duration of science data within the observation window T_{obs}, excluding gaps due to detector downtime or data quality vetoes [140]. With interlaced FFTs, the total number of FFT segments used in the Hough sum is $N_{\mathrm{seg}} = 2N_{\mathrm{eff}}$. The sum runs over all N_{seg} time segments, and f_i is the signal frequency in the i-th segment.

The quantity $S_n(f_i)$ is the detector noise power spectral density evaluated at frequency f_i[1]. The term $(F_+A_+ + F_\times A_\times)$ describes the detector response to the signal, which depends on the source orientation and polarization. Since the inclination and polarization angles are not known for the sources considered here, the detector response entering the theoretical sensitivity is averaged over these unknown orientation parameters. In particular, we sample $\cos\iota$ uniformly in the interval $[-1, 1]$ and the polarization angle ψ uniformly in the interval $[-45°, 45°]$, while

[1]This quantity should not be confused with $S_{\mathrm{AR,i}}(f_j)$ introduced in Sec. 6.4: $S_{\mathrm{AR,i}}(f_j)$ is the local spectral estimate used to normalize the periodogram during peakmap construction, whereas $S_n(f_i)$ represents the detector noise PSD entering the theoretical sensitivity calculation.

keeping the source sky position fixed. The resulting averaged response is then used in Eq. (6.23). Finally, the factor involving CR_{thr} and Γ sets the detection threshold, determining the balance between detection probability and false-alarm rate.

The corresponding maximum distance is obtained by equating the gravitational-wave strain, Eq. 4.8, to the sensitivity, Eq. 6.22, obtaining

$$D_{\mathrm{max}} = \frac{4\pi^2 G}{c^4} \frac{I\,\epsilon}{\mathcal{A}_{\mathrm{min}}}, \tag{6.24}$$

The expressions above provide the theoretical sensitivity of the search in terms of both the minimum detectable strain amplitude and the corresponding maximum source distance. These estimates depend on the detector noise, the analysis configuration, and the assumed signal parameters, and therefore provide a useful benchmark for evaluating the performance of the search pipeline.

In the next chapter, these theoretical predictions will be compared with empirical sensitivities obtained from signal injections into real detector data. This comparison will be used to validate the performance of the updated GFH-v2 pipeline.

Chapter 7

Development and Validation of the GFH-v2 Pipeline

In the previous chapter, we described the main analysis method used in long-transient gravitational-wave searches, the Generalized Frequency Hough transform. This method provides the standard framework used in earlier searches.

In this chapter, we build on that framework and introduce an improved analysis setup, referred to as the GFH-v2 pipeline. This version includes updated choices for key analysis parameters, such as the coherence time and observation time, which are now set using physically motivated conditions based on the expected signal evolution from newborn magnetars. It also includes improvements in the overall computational implementation.

The goals of this chapter are to test the performance of the updated pipeline using real O4a data [140], to verify its ability to recover simulated signals across the relevant parameter space, and to estimate both theoretical and empirical sensitivities. These results are also presented in our recent study [34], which provides a detailed reference for the full pipeline and its validation.

7.1 Search parameter space

7.1.1 Key parameter ranges

The choice of the search parameter space is guided by both astrophysical considerations and computational constraints. The physical properties of a newly formed or rapidly rotating neutron star determine the evolution of the gravitational-wave frequency and its amplitude. At the same time, the geometry of the source relative to the detectors, including its sky position and orientation, affects the detectability of the signal.

Table 7.1 lists the main parameters considered in this study for a newborn, rapidly rotating magnetar. The initial frequency f_0, ellipticity ϵ, and inclination angle ι primarily control the evolution of the signal, including the coherence time used for Fourier transforms (T_{FFT}), the effective observation duration (T_{obs}), and the frequency range covered by the signal.

The chosen ranges are based on astrophysical expectations. Ellipticities in

Table 7.1. Parameter ranges and fixed values used for the injection study.

Parameter	Range/Value
Initial frequency, f_0 [Hz]	600 - 2000
Ellipticity, ϵ	3×10^{-4} - 3×10^{-3}
Inclination angle, ι [deg]	0 - 180
Braking index, n	5
Neutron star mass, M [$M_\odot$]	1.4
Neutron star radius, R [km]	12
Sky longitude (RA) [deg]	210.91 (equatorial)
Sky latitude (Dec) [deg]	54.31 (equatorial)

the range $\epsilon \in [3 \times 10^{-4}, 3 \times 10^{-3}]$ represent plausible deformations for young magnetars, arising from magnetic stresses, formation asymmetries, or bar-mode instabilities [23, 122, 143]. Initial frequencies $f_0 \in [600, 2000]$ Hz correspond to the early spin-down phase, when gravitational-wave emission is expected to be strongest[1] [23, 120, 144, 145]. Inclinations $\iota \in [0, 180°]$ are sampled uniformly in $\cos\iota$, covering all possible orientations.

For the injection study, we assume a neutron-star mass of $M = 1.4\,M_\odot$ and a radius of $R = 12$ km, and calculate the corresponding moment of inertia I using Eq. (4.9). These values are kept fixed in order to limit the number of parameters varied in the injection study and to focus on the dependence of the search on f_0 and ϵ. However, the mass and radius of a newborn neutron star are not known in general, and different values would result in a different moment of inertia. As shown in Eq. (4.4), the spin-down parameter k depends on both the ellipticity and the moment of inertia. Therefore, changing I would also change the frequency evolution of the signal. The parameter space considered here should thus be understood as corresponding to the fixed neutron-star model adopted for this study. A more general analysis could instead explore the parameter space directly in terms of (f_0, k), or vary both ϵ and I by considering different neutron-star masses and radii. We leave this broader exploration for future work.

The sky position is fixed to the nearby core-collapse supernova SN 2023ixf, discovered in May 2023 in the Pinwheel Galaxy (M101) at a distance of approximately 6.85 Mpc [146–148]. SN 2023ixf is one of the closest Type II supernovae observed in the last decade, and multi-wavelength observations suggest it may have formed a magnetar remnant. Its proximity and well-constrained location make it an astrophysically motivated reference target. The O4a data segment used for the injection study does not overlap with the epoch of the supernova event, so no real signal from this source is expected in the data.

Each combination of parameters determines a unique expected signal evolution. In particular, the coherence time T_{FFT} is chosen to ensure the signal remains confined

[1] The lower limit of 600 Hz is not a physical limit on the initial frequency of magnetars, but a practical choice for the search. In particular, extending the analysis to lower frequencies would include the region around ~ 500 Hz, which contains strong suspension violin-mode resonances in the LIGO detectors. Frequencies below 600 Hz are therefore not excluded astrophysically, but are outside the parameter space explored in this work.

within a single frequency bin (see Sec. 7.1.2), and the observation time T_{obs} is defined according to the signal amplitude decay (see Sec. 7.1.3).

Although Table 7.1 represents the specific choices made for this study, the GFH-v2 methodology can be applied to other astrophysically motivated parameter spaces. The parameter ranges defined here determine the characteristics of the signals that are injected into the O4a data to validate the pipeline, as described in Sec. 7.4.

7.1.2 Coherence time

The coherence time T_{FFT} defines the duration of each data segment over which Fourier transforms are computed. Its choice is determined by the expected frequency evolution of the gravitational-wave signal. On one hand, T_{FFT} must be short enough that the signal's frequency drift, primarily caused by the spin-down $\dot{f}_{\text{gw}}$, remains confined within a single frequency bin during the segment. On the other hand, it should be long enough to limit sensitivity loss.

For the purpose of setting T_{FFT}, we approximate the frequency drift as linear over a single FFT segment. This approximation is valid for the short segment durations considered here, even though the full signal follows a power-law frequency evolution. Higher-order spin-down terms, including the second-order term, contribute negligibly over such short durations. For example, in a conservative case with initial frequency $f_0 = 2000$ Hz and ellipticity $\epsilon = 3 \times 10^{-3}$, the maximum T_{FFT} is approximately 1.17 s. Over this segment, the frequency change due to the first-order spin-down is about 0.86 Hz, while the contribution from the second-order term is only 9.2×10^{-4} Hz. This confirms that the linear approximation is sufficient to safely set T_{FFT}.

Within this linear approximation, the frequency change during a segment is given by

$$\Delta f \simeq |\dot{f}_{\text{gw}}|\, T_{\text{FFT}}. \tag{7.1}$$

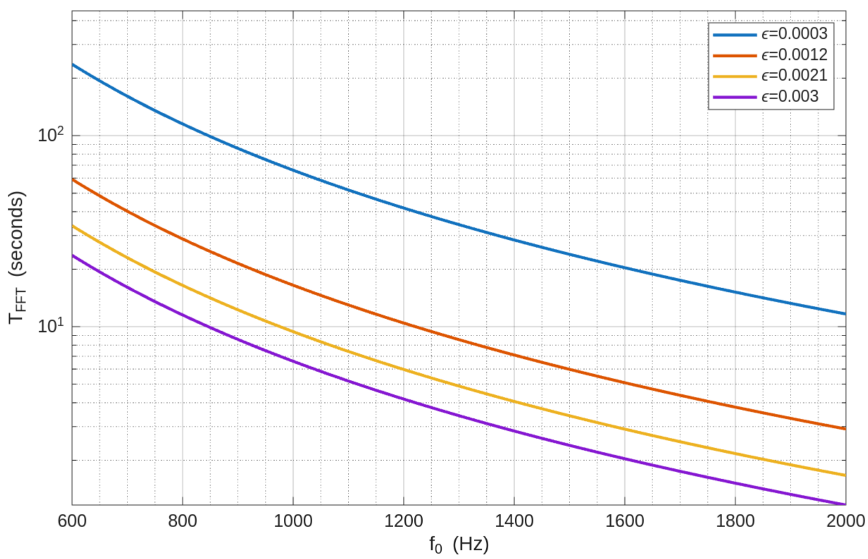

Figure 7.1. FFT duration T_{FFT} versus f_0 for different ellipticities (see Eq. 7.3 - 7.4).

To keep the signal power within a single frequency bin of width $1/T_{\mathrm{FFT}}$, we require:

$$\Delta f \lesssim \frac{1}{T_{\mathrm{FFT}}}. \tag{7.2}$$

Combining the two expressions gives:

$$|\dot{f}_{\mathrm{gw}}|\, T_{\mathrm{FFT}} \lesssim \frac{1}{T_{\mathrm{FFT}}} \quad \Rightarrow \quad T_{\mathrm{FFT}} \simeq \frac{1}{\sqrt{|\dot{f}_{\mathrm{gw}}|}}. \tag{7.3}$$

In practice, $|\dot{f}_{\mathrm{gw}}|$ is evaluated at the start of the signal ($t = t_0$), where the spin-down is largest. This provides a conservative choice for T_{FFT}, ensuring that the signal remains confined to a single frequency bin throughout the segment.

The spin-down rate $\dot{f}_{\mathrm{gw}}$ is related to the ellipticity ϵ and f_{gw} through Eq. (4.1),

$$\dot{f}_{gw} = -\frac{32\pi^4 G\epsilon^2 I f_{\mathrm{gw}}^5}{5c^5}, \tag{7.4}$$

showing that higher ellipticity or frequency results in a faster spin evolution and hence a shorter coherence time.

Figure 7.1 shows the dependence of T_{FFT} on both f_0 and ϵ, highlighting how the segment duration must be adjusted according to the expected properties of the magnetar. These choices are essential to ensure that the injected signals remain coherent within each FFT segment for the pipeline validation study.

7.1.3 Observation time window

In this study, unlike many previous searches where the observation time T_{obs} is typically fixed (see, e.g., [33]), we adopt a strategy that adapts T_{obs} according to the decay of the GW signal amplitude. The motivation for this approach is to integrate only the portion of the data that significantly contributes to the signal-to-noise ratio, thereby optimizing sensitivity while avoiding unnecessary computational cost.

Before adopting the final definition used in this work, we explored a physically motivated way to estimate the observation time based on matched filtering. This approach is useful as a reference because it directly connects the signal duration with the signal-to-noise ratio (SNR) that would be obtained in an optimal search.

In this method, the signal is assumed to follow a known waveform model, and the SNR is computed by correlating the signal with itself while taking into account the detector noise. The accumulated SNR up to a time T is given by

$$\mathrm{SNR}(T) = 2\sqrt{\int_0^T \frac{h^2(t)}{S_n(f(t))}\, dt}, \tag{7.5}$$

where $h(t)$ is the gravitational-wave strain and $S_n(f)$ is the one-sided noise power spectral density evaluated at the instantaneous signal frequency $f(t)$.

The observation time is then defined as the smallest time T_{obs} such that the accumulated SNR reaches a fixed threshold,

$$\mathrm{SNR}(T_{\mathrm{obs}}) = \mathrm{SNR}_{\mathrm{thr}}. \tag{7.6}$$

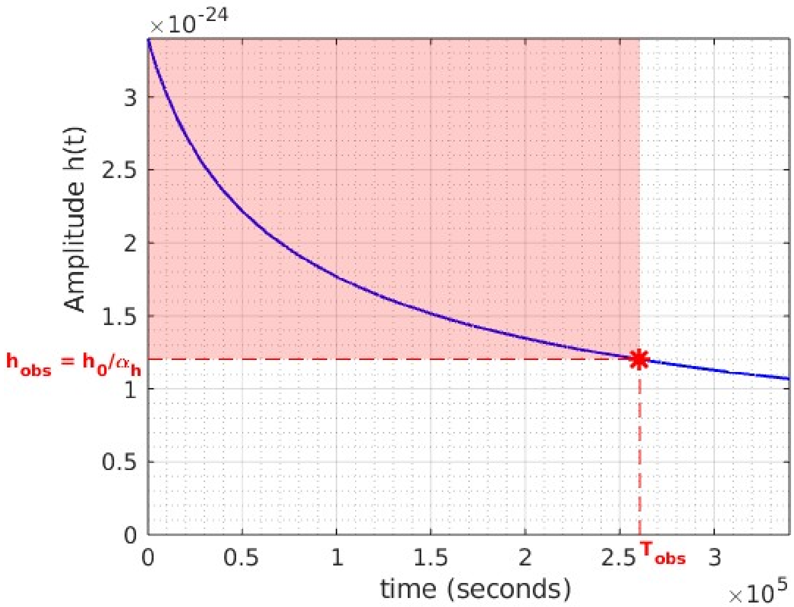

Figure 7.2. Definition of the observation time T_{obs} from the decay of the signal amplitude for a fixed reduction factor α_{h} shown for $\epsilon = 0.002$ and $f_0 = 900$ Hz.

This definition ensures that the signal is integrated only as long as it contributes significantly to the detection statistic. It also provides a physically motivated estimate of how long a signal remains detectable for a given set of source parameters.

Although this method is useful for understanding the expected signal duration, it is computationally expensive in practice because it requires solving the SNR integral for each injection. Moreover, such an approach is not applicable in a real search, where the exact signal waveform is unknown and the parameter space is explored over a large number of templates. For this reason, it was not used in the final pipeline configuration.

Instead, the final definition of T_{obs} is based on the decay of the signal amplitude. This approach is simpler to implement and provides a stable and consistent way to select the portion of the data that contains most of the signal power. Here we define T_{obs} as the time required for the instantaneous signal amplitude $h(t)$ to decrease to a predetermined fraction of its initial value h_0. This fraction is controlled by the amplitude reduction factor α_{h}, such that

$$T_{\text{obs}} = t \quad \text{s.t.} \quad h(t) = \frac{h_0}{\alpha_{\text{h}}}.$$

Figure 7.2 illustrates this definition for a representative case with $f_0 = 900$ Hz, $\epsilon = 0.002$, and a fixed α_{h}. The decay of $h(t)$ is derived from the expected spin-down of a rapidly rotating neutron star, accounting for both the decreasing rotational frequency and the corresponding reduction in gravitational-wave amplitude.

To select an optimal value of α_{h}, we evaluate the sensitivity $h_{0,\text{min}}$ as a function of α_{h} across several representative frequencies and ellipticities, using the formulation described in Section 7.6.1(Eq. 6.22). The results are shown in Fig. 7.3.

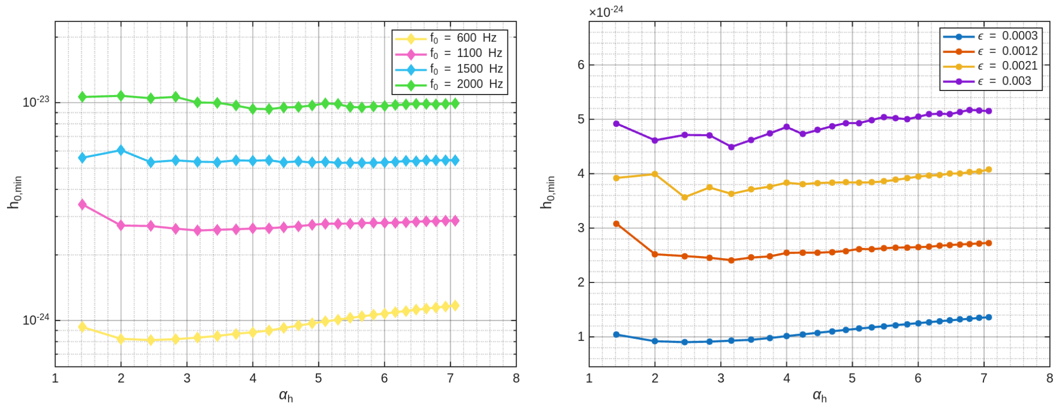

Figure 7.3. *Left:* Sensitivity $h_{0,\mathrm{min}}$ as a function of α_h for different initial frequencies f_0 and fixed ellipticity $\epsilon = 0.001$. *Right:* Dependence of $h_{0,\mathrm{min}}$ on α_h for different ellipticities ϵ at a representative $f_0 = 1000 Hz$. Each point is obtained from the theoretical sensitivity calculation of Eq. 6.22

The dependence of $h_{0,\mathrm{min}}$ on α_h is not monotonic and results from a balance between different effects. Increasing α_h increases the observation time and therefore includes more segments in the analysis. However, at later times the signal amplitude is lower because of the spin-down evolution, so these additional segments do not necessarily improve the sensitivity. At the same time, changing the number of segments also changes the statistical background entering the detection statistic, as reflected by the dependence on N_eff in Eq. 6.23. Therefore, including more data does not always lead to better sensitivity.

In addition, the detector noise is not stationary over the observation period. The contribution of each segment depends on the noise power spectral density $S_n(f_i)$, which also enters Eq. 6.23. A later segment with a weaker signal can therefore still contribute to the sensitivity if the detector noise at that time and frequency is sufficiently low. These competing effects produce the relatively shallow minima seen for some of the curves in Fig. 7.3.

For each set of source parameters, we choose the value of α_h that minimizes $h_{0,\mathrm{min}}$. In some cases the minimum is weakly defined, indicating that a shorter observation time can be used with little loss in sensitivity and with a lower computational cost. In other cases the minimum is more pronounced, making the choice of α_h more important. This optimization therefore provides a practical way of selecting the observation window while accounting for the signal evolution, detector noise, and statistical properties of the search.

The observation times T_obs derived from this optimization are shown in Fig. 7.4 where each point corresponds to the duration associated with the optimal α_h. This approach ensures that the analysis focuses on the portions of the dataset where the signal amplitude is significant, refining the search strategy by balancing sensitivity and computational efficiency. By adjusting T_obs for each set of source parameters, the method provides a systematic and physically motivated way to define the observation window in the search.

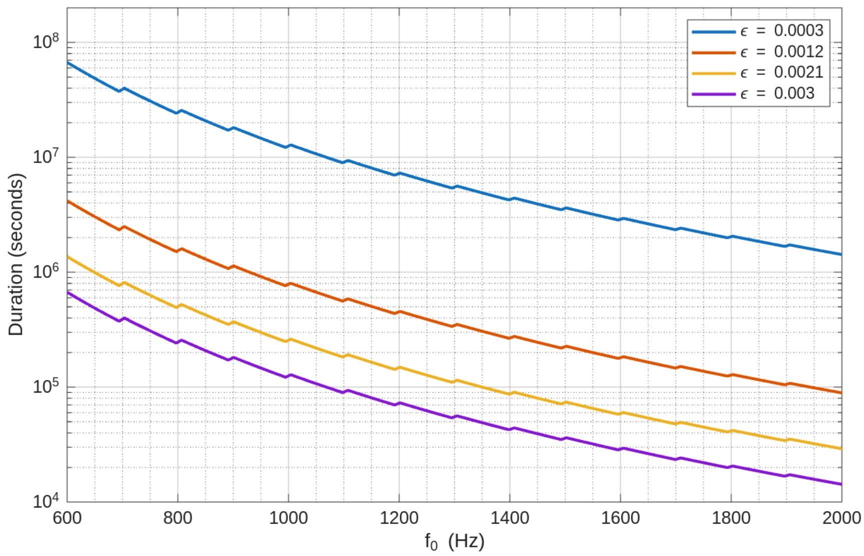

Figure 7.4. Observation time T_{obs} as a function of f_0 for different ellipticities, corresponding to the optimal α_{h} derived from Fig. 7.3.

7.1.4 Frequency band

The selection of the frequency band for the analysis is directly linked to the signal evolution over the chosen observation window T_{obs}. Starting from the initial frequency f_0, the gravitational-wave signal undergoes a spin-down as described in Sec.4.1. The lower edge of the frequency band is defined by the frequency reached at the end of the observation window, $f(T_{\mathrm{obs}})$, ensuring that the analysis includes the entire portion of the signal that significantly contributes to the detection statistic.

Mathematically, the frequency band is given by:

$$f_{\mathrm{band}} \in [f(T_{\mathrm{obs}}), f_0] \,, \tag{7.7}$$

By defining the frequency band with the observation window, the analysis ensures that computational resources are focused on the portion of the spectrum where the signal is most significant.

7.2 GFH-v2 algorithmic improvements

The GFH-v2 pipeline represents a substantial improvement with respect to the original implementation of the Generalized Frequency Hough transform [32], both in terms of data handling and computational strategy. The modifications are aimed at increasing computational efficiency and ease of use within the broader gravitational-wave data analysis framework [34].

The computational implementation of the algorithmic improvements described in this section was developed by L. Pierini within the Virgo Collaboration. The GFH-v2 method and its main computational developments are described in Ref. [34]. The work presented in this thesis focuses on the astrophysical optimization of the search setup, the validation of the pipeline through signal injection studies, and its application to searches for long-transient gravitational-wave signals.

First major difference concerns the preprocessing of detector data. The original implementation started with the Short Fourier Transform Database, and the relatively long FFTs (typically of duration $\mathcal{O}(10^3)$ s) were reprocessed into shorter segments, with durations of the order of tens of seconds, determined according to the coherence time T_{FFT}. These shorter FFTs were then restricted to the frequency band of interest, and simulated signal injections were performed at this stage. The peakmap was then constructed by identifying significant local maxima in the normalized power spectrum of each FFT segment.

In contrast, the GFH-v2 approach adopts a different strategy. After extracting the frequency band of interest, the SFDB data blocks are combined and inverse Fourier transformed to reconstruct a time-domain signal corresponding to that band. This generates a sub-sampled, complex analytic time series, restricted to the frequency band spanned by the signal over the observation time T_{obs}, namely from the initial frequency f_0 down to the value reached due to spin-down (see Sec. 7.1.4). This representation is closely analogous to the Band Sampled Data (BSD) framework [23], which has been widely adopted in continuous-wave searches. However, an additional cleaning procedures typically applied in standard BSD-based analyses to suppress persistent narrow-band disturbances, which are particularly problematic for quasi-monochromatic signals, are not applied in the present context, as the signals of interest evolve over a relatively broad frequency range. This approach enables a more flexible implementation of subsequent analysis steps. In particular, operations such as signal injection or peakmap construction can be performed directly in the time domain using existing libraries, improving reproducibility of the analysis pipeline.

A second major innovation of GFH-v2 lies in the implementation of the core Hough transform. In the original GFH algorithm, the mapping from the peakmap to the Hough parameter space was performed through a double nested loop. The outer loop iterated over time, selecting peaks corresponding to each FFT segment, while the inner loop iterated over the discretized values of the parameter k, updating the corresponding bins in the Hough map. This approach suffers from significant computational limitations, in particular, loops for different peaks accessing the same memory locations for writing, limits the possibility to parallelize the operation and to exploit modern computing architectures.

In GFH-v2, this limitation is overcome by restructuring the algorithm. The loop over time is entirely removed, and the computation is instead organized around the parameter k, which determines the slope of the signal trajectory in the transformed (t, x) space (see Eq. 6.7). For each discrete value of k, the full peakmap is processed simultaneously by applying the corresponding linear transformation and the construction of a histogram along the grid of transformed frequencies x_0. In the present implementation, the histogram is constructed using unweighted counts, meaning that each selected peak contributes equally. While weighted implementations, incorporating information on detector sensitivity or noise non-stationarity, are possible and have been explored in other contexts, they are not included here in order to maintain simplicity. The extension to weighted statistics is planned for future developments.

The result of the histogram fills one column in the Hough map at the location

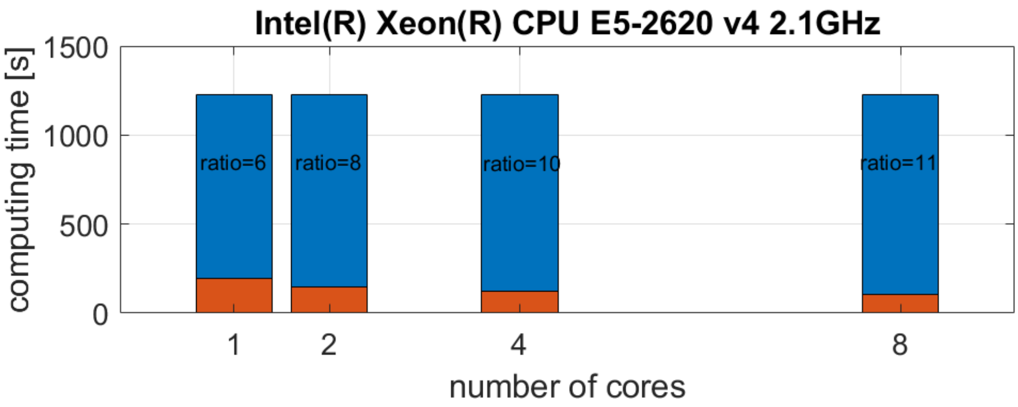

Figure 7.5. Computing time comparison between the old GFH and GFH-v2 implementations [34]. Blue bar: original GFH implementation running on a single thread. Red bars: GFH-v2 implementation using multithreading.

corresponding to the selected k value. This new implementation of the transform is made by means of highly-optimized functions, which compute the 1D histograms using buffer arrays to speed up memory access. Compared to the original implementation, where the Hough map was computed through a double nested loop over time indexes and k values with direct memory access, the GFH-v2 avoids the outer time loop and efficiently integrates the entire peakmap along each k value.

Figure 7.5 shows a comparison of the computing times for the original GFH and the GFH-v2 implementations. The test dataset covers an 800 Hz-wide frequency band and a 9-hour time window, analyzed with $T_{\rm FFT} = 2$ s. The tests were performed on an Intel Xeon E5-2620 machine (16 cores, 2.1 GHz, hyperthreading). While the original implementation runs on a single thread, GFH-v2 exploits multithreading. The figure therefore compares the computational performance of the two implementations as used here, rather than providing a direct single-thread comparison of the underlying algorithms. Under this configuration, GFH-v2 reduces the computing time by approximately one order of magnitude. The improvement results from the restructuring of the Hough transform together with the possibility of parallelizing the computation over the k grid [34].

Here, each different k value of the grid is mapped in a different column in the Hough map, so the loop can be performed in parallel exploiting hyper-threading or multi-core CPUs. While implementations on Graphics Processing Units (GPUs) are also possible [149], the current analysis demonstrates that CPU-based execution is sufficient for the parameter space explored in this work. However, GPU acceleration remains a good option for future searches involving larger datasets or extended parameter ranges.

A schematic representation of the complete GFH-v2 workflow is shown in Fig. 7.6, summarizing the main processing steps from the input SFDB to the follow-up [34].

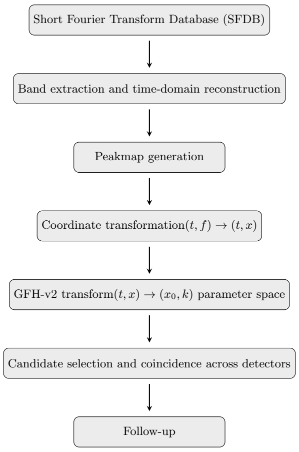

Figure 7.6. Schematic view of the GFH-v2 pipeline workflow.

7.3 Data characteristics

To validate the performance of the GFH-v2 pipeline described in Chapter 7.2, we use detector data from the fourth observing run (O4) of the LIGO-Virgo-KAGRA detector network. The properties of the detector data, including sensitivity and spectral characteristics, play a crucial role in determining the effectiveness of long-transient gravitational-wave searches.

In this section we describe the data used in this study, including the characteristics of the O4 observing run, the selection of the O4a data segments used for the validation analysis, and the spectral properties of the selected data.

7.3.1 The O4 observing run

The fourth observing run of the LVK gravitational-wave collaboration represented the most sensitive period of gravitational-wave observations to date. The run began on 24 May 2023 and concluded on 18 November 2025, following a series of commissioning upgrades aimed at improving detector stability and strain sensitivity across the network.

O4 significantly increased the number of known gravitational-wave events. Real-time searches identified roughly 250 candidate events during the run, the vast majority of which were consistent with compact binary coalescences [12]. Most of these events correspond to mergers of binary black holes, which continue to dominate the currently observed gravitational-wave population. Several notable events were detected during O4. For example, the event GW231123 is currently the most massive binary black hole merger observed, producing a remnant black hole with a mass above 200 $M_\odot$. Another event, GW250114 achieved a SNR of approximately 77-80, making it one of the loudest gravitational-wave detections recorded so far.

The observing run was divided into three phases to accommodate detector upgrades and maintenance periods. The first phase, O4a (24 May 2023 - 16 January 2024), primarily involved the two LIGO detectors; LIGO Hanford (H1) and LIGO Livingston (L1). The second phase, O4b (April 2024 - January 2025), included

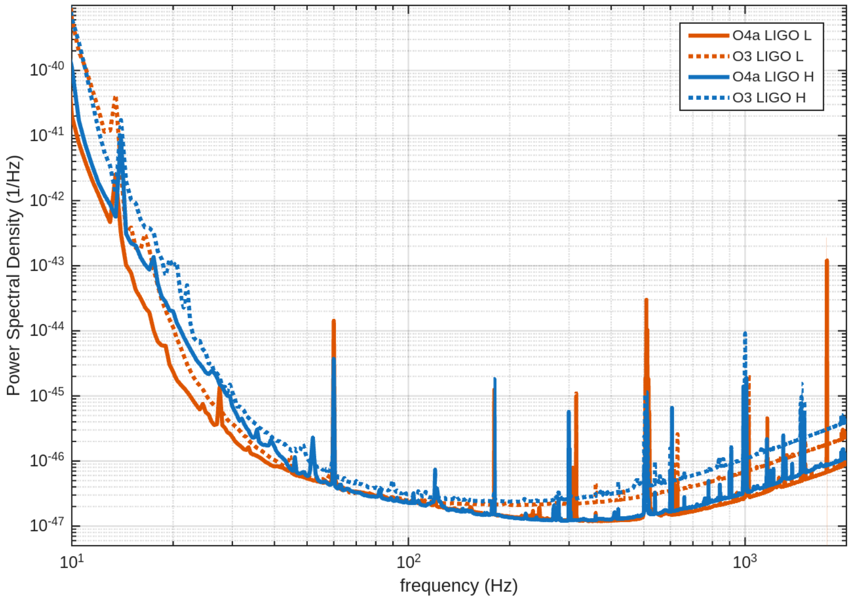

Figure 7.7. Power spectral density for the Advanced LIGO detectors during the observing runs O3 (dotted lines) and O4a (solid lines). The sensitivity improvement compared to previous observing runs enhances the prospects for detecting long-transient gravitational-wave signals from nearby sources.

participation from the Virgo detector and intermittent contributions from the KAGRA detector. The final phase, O4c (January 2025 - November 2025), continued observations mainly with the LIGO and Virgo detectors.

Significant improvements in detector sensitivity were achieved during O4. In particular, the LIGO detectors reached a BNS inspiral range exceeding approximately 160 Mpc. This represents more than a factor of two improvement relative to the first observing run (O1).

Figure 7.7 compares the noise spectral densities of the Advanced LIGO detectors during O3 and O4a, illustrating the improvement in detector sensitivity between the two observing runs. The procedure used to compute the average noise spectra from the SFDB data is described in the following subsection 7.3.2.

The improved detector sensitivity achieved during O4 make this dataset particularly valuable for validating gravitational-wave search pipelines. In this work, we focus specifically on the O4a data segment, which provides extended periods of stable detector operation suitable for the validation of the GFH-v2 long-transient search pipeline.

7.3.2 Average spectra of the O4a data

The sensitivity of GW searches strongly depend on the spectral properties of the detector noise. In particular, the noise power spectral density determines the frequency-dependent strain sensitivity of the detectors. To characterize the noise properties of the O4a data used in this analysis, we compute the average noise power

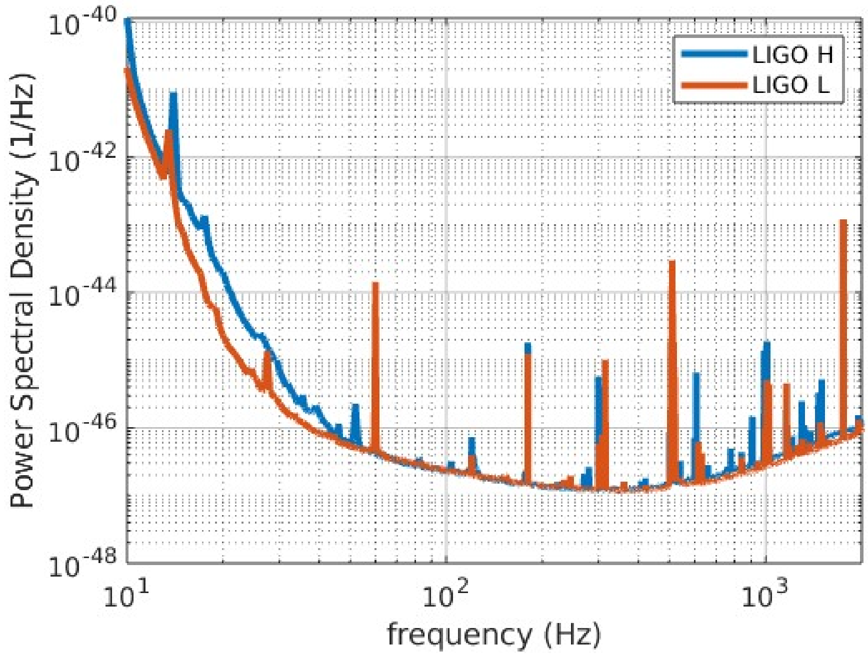

Figure 7.8. Average noise spectral densities of both detectors computed over the full O4a dataset

spectral densities for both the LIGO Hanford and LIGO Livingston detectors. The PSDs shown here, as well as those used for the O3-O4a comparison in Fig. 7.7, are computed from the SFDB data [131] by averaging the power spectra of the individual FFT segments belonging to science time, applying basic data-quality vetoes and a weighted averaging procedure that reduces the influence of noisier spectra [31].

Figure 7.8 shows the average PSDs for both detectors computed over the full O4a dataset used in this work. The spectra illustrate the typical frequency-dependent sensitivity of the Advanced LIGO detectors during O4a. Unlike Fig. 7.7, whose purpose is to compare the detector sensitivity between O3 and O4a, Fig. 7.8 focuses only on O4a and provides a detailed characterization of the noise spectra of the H1 and L1 data relevant to the analysis presented in this work.

7.3.3 Selected O4a segments

The dataset used in this study is drawn from the first portion of the fourth observing run, commonly referred to as O4a which spans the period from 24 May 2023 to 16 January 2024 [63, 140]. Relative to the previous observing run (O3), O4a marked a substantial upgrade to the interferometers aimed at improving strain sensitivity, duty cycle, and overall detector stability [150].

During O4a, the Virgo detector [58] was not participating in science observations due to commissioning activities intended to improve its sensitivity for later phases of the run. The KAGRA detector [6] and the GEO 600 detector [59] were operating during parts of this period; however, their sensitivity remained significantly lower than that of the Advanced LIGO interferometers [4]. Thus the analysis presented in

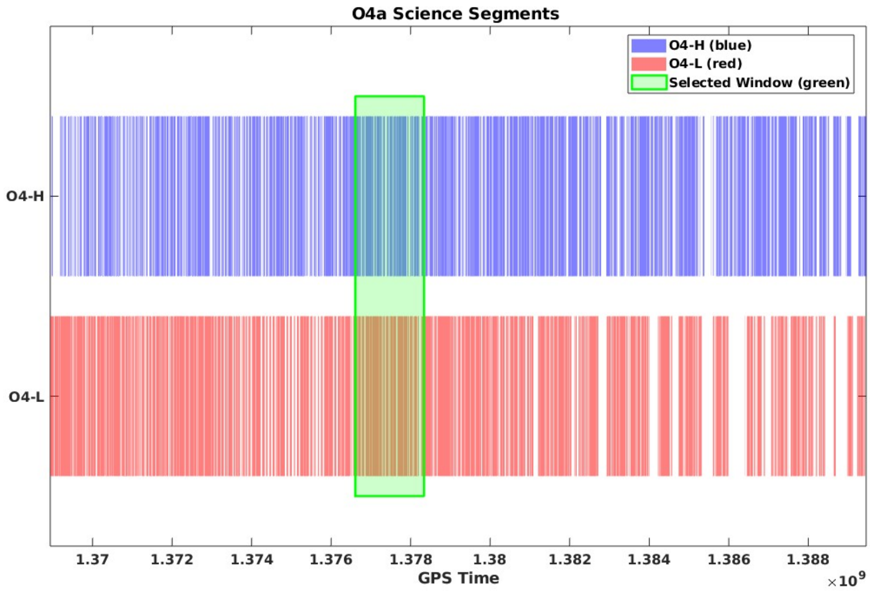

Figure 7.9. Science-mode segments for the LIGO Hanford and Livingston detectors during the O4a observing period. The green shaded region marks the 20-day interval selected for the analysis presented in this work.

this work uses data only from the two Advanced LIGO detectors: LIGO Hanford (H1) and LIGO Livingston (L1).

To evaluate the empirical sensitivity of the GFH-v2 pipeline, we select a contiguous 20-day interval of data beginning on 20 August 2023 (Modified Julian Date MJD: 60176.991). This time period was chosen because it contains long stretches of stable detector operation with relatively consistent noise characteristics.

The actual data used for the analysis correspond to the *science segments* identified by the detector data quality flags [140]. These segments represent periods during which the detectors were operating in science mode and the recorded strain data are considered suitable for astrophysical analysis. Periods affected by instrumental issues, calibration problems, or poor data quality are excluded from the analysis.

The GFH-v2 pipeline determines the effective observation time T_{obs} individually for each injected signal, based on its initial frequency f_0 and ellipticity ϵ (see Sec. 7.1.3 and Fig. 7.2). This effective observation duration corresponds to the portion of the signal evolution that falls within the selected dataset and only this effective duration is used in the analysis when estimating detection efficiency and sensitivity. For the upper ellipticity sub-interval considered in the empirical sensitivity study (see Sec. 7.1.1), the full evolution of the simulated signals is contained within the selected 20-day data window. This ensures that the injected signals are not limited by the dataset, allowing a consistent and unbiased evaluation of the pipeline sensitivity.

Figure 7.9 shows the science-mode segments for the full O4a observing period together with the selected 20-day analysis window highlighted in green. A zoomed-in view of this selected interval is shown in Fig. 7.10, illustrating the distribution of science segments and the availability of coincident observing time between the

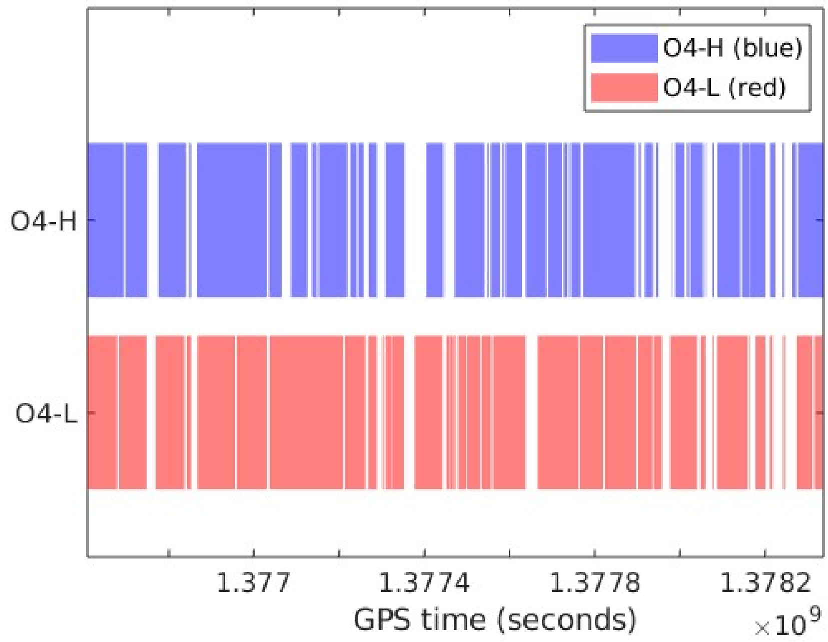

Figure 7.10. Expanded view of the selected 20-day O4a data interval used in this analysis for the GFH-v2 pipeline validation.

Hanford and Livingston detectors during the period used in this work.

7.4 Signal injections

To validate the performance of the pipeline and to estimate its sensitivity, simulated signals were injected into the data. The injections were performed in the time-domain reduced-analytic series obtained from the O4a SFDB, following the procedure described in Sec. 7.2. The injected signals span the parameter space defined in Sec. 7.1.1 (see Table 7.1).

The full range of ellipticity, $\epsilon \in [3 \times 10^{-4}, 3 \times 10^{-3}]$, was divided into five representative sub-intervals. This choice allows to probe how the signal properties change across the parameter space, in particular the combined effect of amplitude and spin-down, while keeping the total number of injections computationally manageable. For each sub-interval, injections were performed with the ellipticity drawn from a uniform distribution within that sub-interval, over the full range of initial frequencies f_0, using a spacing of 10 Hz. This spacing was chosen as a reasonable compromise between covering the parameter space and keeping the number of injections computationally manageable. A more detailed study of the optimal spacing is left for future work. Within each 10 Hz frequency interval and the selected ellipticty sub-interval, approximately 150 signals were generated, with the exact number varying between 120 and 180 depending on the band; In some regions, additional injections were done.

The remaining physical parameters are also randomized. In particular, the inclination angle is sampled assuming a uniform distribution in $\cos\iota \in [-1, 1]$, and the polarization angle is drawn uniformly in its full range. This ensures that the injected population does not introduce biases related to source orientation. The procedure is repeated for different source distances in order to study the detection efficiency as a function of distance.

The effective observation time $T_{\rm obs}$ for each injected signal is determined by its initial frequency f_0 and ellipticity ϵ, as described in Sec. 7.1.3 (see also Fig. 7.2). The coherence time $T_{\rm FFT}$ is chosen consistently with the criteria discussed in Sec. 7.1.2, so that the signal remains confined within a single frequency bin over each FFT segment.

All injections are assumed to start at the beginning of the dataset. This simplifies the analysis, as it removes the need to scan over the signal start time. In a more realistic scenario, the signal could start at any time within the observation window. Including this additional parameter would require introducing a grid in start time, which increases the number of trials. A possible extension of this work would include such a search over start times, with an appropriate choice of step size to balance parameter-space coverage and computational cost.

7.5 Candidate selection

The identification of significant candidates from the Hough maps is a crucial step of the analysis. This procedure is designed to reduce the large number of bins in the map to a reasonable set of promising outliers, while keeping a high probability of retaining true signals. The method consists of three main steps: segmentation of the Hough map, selection of candidates within each segment, and evaluation of coincidences.

7.5.1 Hough map segmentation

In order to explore the parameter space in a uniform way, the Hough map is divided into smaller regions (blocks) in the (x_0, k) plane, following the standard procedure used in Frequency Hough and continuous-wave searches [31, 32]. This segmentation allows the selection procedure to identify candidates across the full parameter space, avoiding a concentration of candidates in only a few regions.

The division along the x_0 axis is chosen based on the extent of the parameter space covered by the signal. In the case of the injection study, the number of blocks is adjusted according to the number of injected signals and the width of the spin-down band. This choice helps control the density of selected candidates and ensures that different signals can be independently identified.[2]

Along the k axis, the map is divided such that each block has approximately the same number of bins in both directions. This results in blocks that are roughly square-shaped in the (x_0, k) plane, which simplifies the comparison of candidates across different regions.

[2] In a real search, the segmentation is typically fixed, for example using a predefined number of blocks along each axis. This will be discussed in the next chapter.

7.5.2 Candidate selection within each block

Once the Hough map is divided into blocks, candidates are selected independently within each block. For each block, the bin with the highest number count is identified as the primary candidate. This bin corresponds to the most significant with respect to the local background.

In order to allow for the presence of multiple signals within the same region, a second candidate can also be selected. This is done only if it is sufficiently separated from the first candidate. In this analysis, a minimum distance of 6 bins in the x_0 direction is required. This condition reduces the probability of selecting multiple candidates originating from the same signal or from local noise fluctuations.

7.5.3 Coincidence analysis

After candidate selection, a coincidence analysis is performed to suppress false alarms (see Sec.6.6.3. The basic idea is that a true astrophysical signal should be observed consistently across different detectors, or should match the parameters of an injected signal in validation studies.

The coincidence between candidates from different detectors is evaluated using a distance in the (x_0, k) parameter space:

$$d_{\text{coin}} = \sqrt{\left(\frac{x_{0,2} - x_{0,1}}{\delta x_0}\right)^2 + \left(\frac{k_2 - k_1}{\delta k}\right)^2}, \tag{7.8}$$

where δx_0 and δk are the grid spacings. Candidates are considered coincident if this distance is smaller than a chosen threshold.

An additional coincidence check is used to evaluate the recovery of injected signals. In this case, the distance is computed between the candidate parameters and the injected signal parameters:

$$d_{\text{coin\_inj}} = \sqrt{\left(\frac{x_{0,\text{cand}} - x_{0,\text{inj}}}{\delta x_0}\right)^2 + \left(\frac{k_{\text{cand}} - k_{\text{inj}}}{\delta k}\right)^2}. \tag{7.9}$$

In this study, only the parameters x_0 and k are varied, and a coincidence threshold of $d_{\text{coin}} = 2$ is used. In more general searches, additional parameters such as sky position or braking index would be included, typically requiring a larger coincidence threshold.

7.5.4 False alarm rate and critical ratio threshold

The final step in the candidate selection process is the application of a threshold on the critical ratio, which measures the statistical significance of a candidate. The critical ratio is defined in Sec.6.6.2. This quantity provides a simple way to quantify how much a candidate stands out above the noise background.

The choice of the threshold CR_{thr} determines the balance between sensitivity and false-alarm probability. A low threshold increases the number of detected signals, but also leads to a higher rate of false candidates. On the other hand, a high threshold reduces false alarms but may cause weaker signals to be missed. To determine a suitable value, injection studies were performed using O4a data at a fixed source

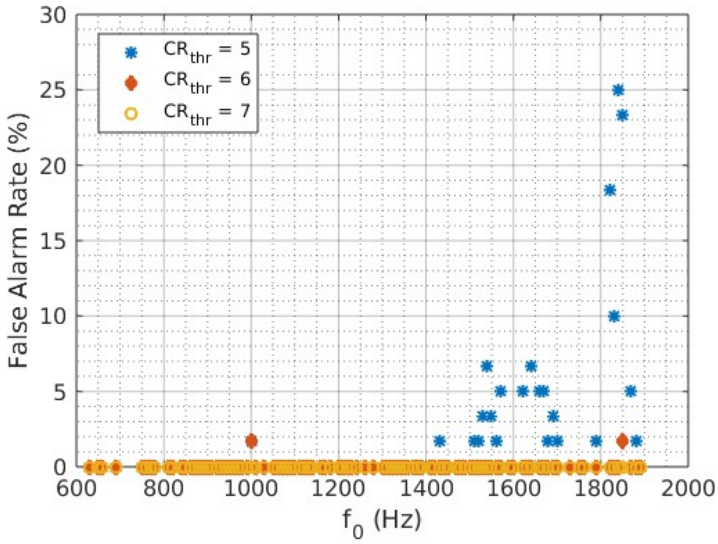

Figure 7.11. False-alarm rate as a function of frequency for different critical ratio thresholds $CR_{\rm thr}$. Most points are zero for higher thresholds (6 and 7), illustrating that the chosen $CR_{\rm thr} = 7$ effectively suppresses false alarms across nearly all f_0 whereas $CR_{\rm thr} = 5$ shows a non-negligible false-alarm fraction

distance of 1000 Mpc. For each value of $CR_{\rm thr}$, the fraction of false alarms was estimated as a function of frequency.

Figure 7.11 shows the resulting false-alarm rate for different threshold values. As expected, the false-alarm rate decreases rapidly as the threshold increases.

In this work, we require the false alarm probability to remain below 0.1%. The study shows that the threshold needed to satisfy this requirement is not exactly the same for all frequencies and ellipticity intervals. In some regions of the parameter space, a lower threshold would already be sufficient, while in others a slightly higher threshold would be required. Rather than using a different threshold for each individual configuration, we adopt a single threshold for the entire analysis. This simplifies the pipeline and ensures that the significance of candidates is evaluated consistently across all searches. To remain conservative, we choose the largest threshold value required by the false alarm study.

Thresholds below $CR_{\rm thr} \approx 5$ lead to a significant number of false coincidences, while thresholds above 7 begin to reduce the recovery efficiency for weaker signals. Based on these results, a value of $CR_{\rm thr} = 7$ is adopted. This choice provides a good compromise, ensuring a low and stable false-alarm rate across the full frequency range while maintaining a reasonable sensitivity to signals.

7.6 Sensitivity estimation

The next step is to quantify how sensitive the GFH-v2 pipeline is to the signal model considered in this work. In practical terms, we want to determine the weakest signals that can be detected, or equivalently, the largest distance at which a source can still be observed.

Two complementary approaches are used: First, we derive a theoretical estimate based on the analytical expressions presented in Sec. 6.7. These equations provide the expected minimum detectable strain amplitude and the corresponding maximum detectable distance as functions of the signal parameters and detector noise.

Second, we perform injection studies in real detector data. Simulated signals are added to the data and searched for using the full pipeline. The fraction of recovered injections provides an empirical measurement of the actual sensitivity.

Comparing these two approaches serves two purposes. It verifies that the implementation behaves as expected and also shows how closely the analytical predictions describe the performance of the pipeline when applied to real detector data.

7.6.1 Theoretical sensitivity

The analytical expressions derived in Sec. 6.7 allow us to estimate the sensitivity of the search before performing computationally expensive injection campaigns. In particular, they provide two useful quantities: the minimum detectable strain amplitude, $h_{0,\mathrm{min}}$ and the maximum detectable distance, D_{max}.

The quantity $h_{0,\mathrm{min}}$ represents the smallest signal amplitude that is expected to produce a candidate above the selected threshold with the required confidence level. Once this amplitude is known, Eq. (6.24) can be used to convert it into the corresponding source distance.

Figure 7.12 shows the theoretical sensitivity of the GFH-v2 pipeline obtained using the equations described in Sec. 6.7 together with real O4a data. The upper panel presents the minimum detectable strain amplitude, $h_{0,\mathrm{min}}$, while the lower panel shows the corresponding maximum detectable distance, D_{max}, as a function of the initial signal frequency f_0. Different curves correspond to different values of ellipticity.

The source sky position is kept fixed to that of SN 2023ixf, while the detector response is averaged over the unknown source orientation, as described in Sec. 6.7. In particular, $\cos\iota$ is sampled uniformly in $[-1, 1]$ and the polarization angle ψ uniformly in $[-45°, 45°]$. The theoretical curves therefore represent orientation-averaged sensitivities rather than sensitivities for a particular inclination or polarization.

To estimate the sensitivity, we use the PSDs computed from the complete O4a observing run for both LIGO detectors. Since the noise level is slightly different between the two detectors, we conservatively take, at each frequency, the larger PSD value between LIGO Hanford and LIGO Livingston.

The overall behaviour of the curves follows directly from Eq. (6.22) and Eq. (6.24). In general, $h_{0,\mathrm{min}}$ increases with f_0, although the exact behaviour also depends on the signal evolution, the corresponding analysis parameters, and the frequency-dependent detector noise.

An important point when comparing the two panels of Fig. 7.12 is that D_{max} is not determined by $h_{0,\mathrm{min}}$ alone when different ellipticities are considered. Using $\mathcal{A}_{\mathrm{min}} = h_{0,\mathrm{min}}/f_0^2$ in Eq. (6.24), the maximum distance can be written as

$$D_{\mathrm{max}} = \frac{4\pi^2 G}{c^4} \frac{I \epsilon f_0^2}{h_{0,\mathrm{min}}}. \tag{7.10}$$

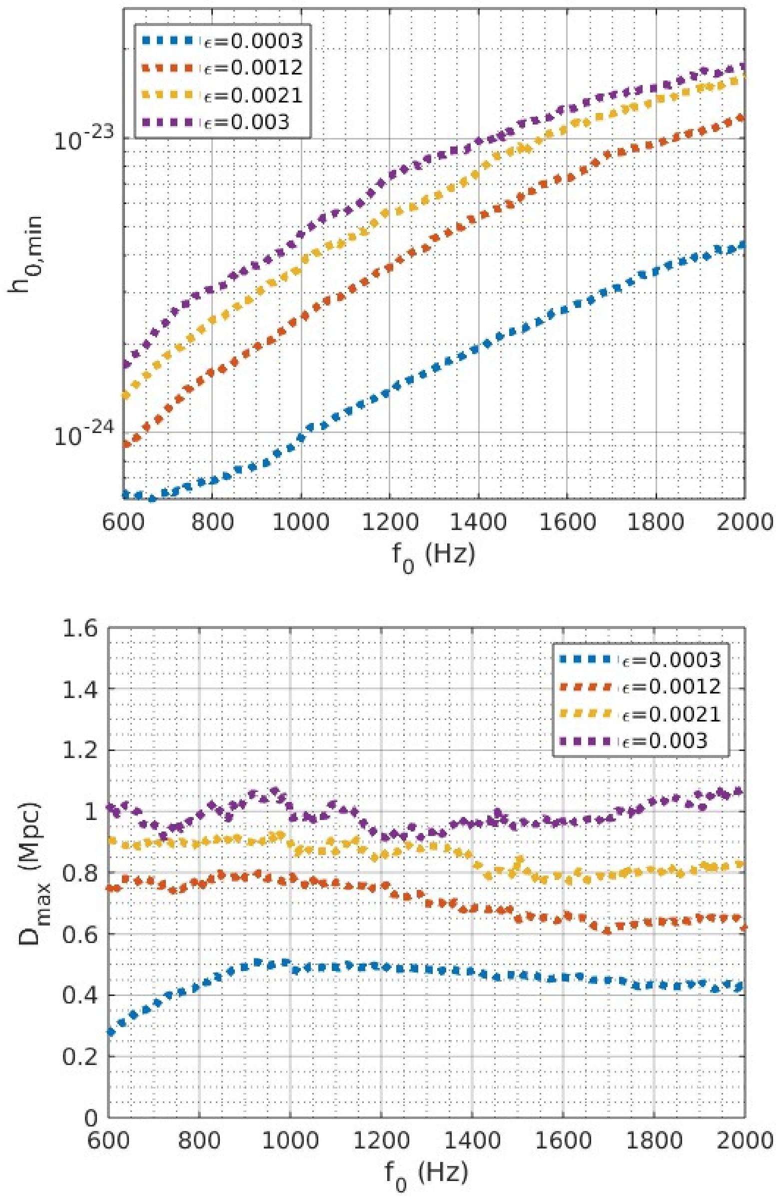

Figure 7.12. Theoretical sensitivity obtained using full O4a LIGO data for the Livingston and Hanford detectors [63, 140], taking the maximum PSD value between the two detectors at each frequency to ensure a conservative estimate (see also Fig. 7.8 for the PSD overview) *Upper:* Minimum detectable strain amplitude $h_{0,\mathrm{min}}$ as a function of the signal initial frequency f_0. *Lower:* Corresponding maximum detectable distance D_{max} as a function of f_0. Both panels refer to $\Gamma = 90\%$ and a critical ratio threshold of $CR_{\mathrm{thr}} = 7$.

Thus, at fixed f_0 and ϵ, a lower $h_{0,\text{min}}$ corresponds to a larger detection distance. However, this relation cannot be used directly to compare curves with different ellipticities, since D_{max} also scales directly with ϵ. This explains why the lowest $h_{0,\text{min}}$ curve in the upper panel does not correspond to the highest D_{max} curve in the lower panel. Although the search reaches a lower strain threshold for the smaller-ellipticity signals, these sources also produce intrinsically weaker GW emission, resulting in a smaller detection distance.

The lower values of $h_{0,\text{min}}$ obtained for smaller ellipticities are related to the slower frequency evolution of these signals. A smaller ellipticity corresponds to a smaller spin-down parameter k and therefore to a longer signal. This generally allows a longer coherent time and a larger amount of useful data to contribute to the search, improving the strain sensitivity. Conversely, signals with larger ellipticity evolve more rapidly and are observed over a shorter effective duration.

This trend is not expected to continue indefinitely toward smaller ellipticities. As the spin-down becomes slower, the signal duration eventually becomes comparable to or longer than the available observation window. Beyond this point, decreasing the ellipticity does not provide the same gain from increasing the amount of data included in the analysis, and the improvement in $h_{0,\text{min}}$ is expected to saturate. The ellipticity range considered in this work was selected for the GFH-v2 validation study and does not extend sufficiently far toward smaller values to characterize this transition. Determining the location of this turnover would therefore require extending the theoretical study to smaller ellipticities and longer signal durations, which is left for future work.

Finally, the impact of the real detector PSDs, which are not flat, introduces small frequency-dependent variations in the sensitivity, producing small-scale fluctuations in the curves. These PSD-induced variations are smaller than the main f_0^2-driven trend and do not qualitatively alter the observed sensitivity behavior.

Dependence on inclination angle

The observed amplitude of a continuous gravitational-wave signal depends not only on the intrinsic source strength but also on the orientation of the neutron star

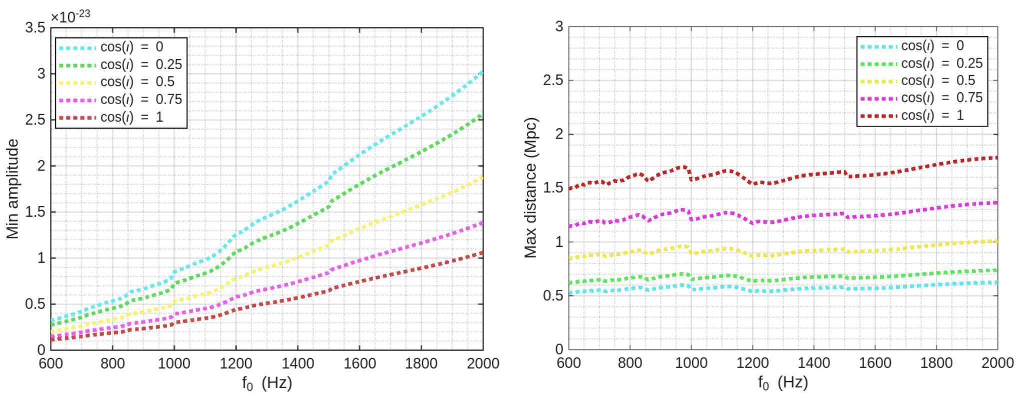

Figure 7.13. Theoretical sensitivity as a function of the initial frequency f_0 for different values of $\cos\iota$.

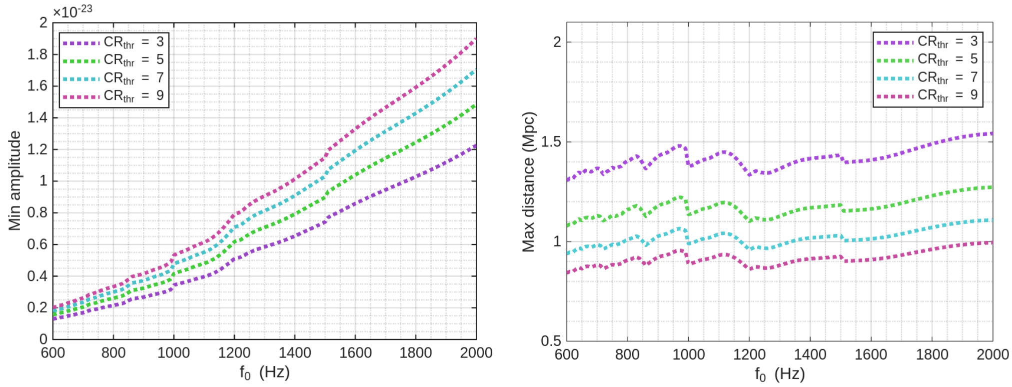

Figure 7.14. Theoretical sensitivity as a function of the signal initial frequency f_0 for different CR_{thr}.

relative to the observer. This orientation is described by the inclination angle ι, defined as the angle between the star's rotation axis and the line of sight.

When the star is viewed along its rotation axis ($\iota = 0°$ or $180°$), the signal is circularly polarized and the detected amplitude is maximal. When the star is viewed edge-on ($\iota = 90°$), the signal is linearly polarized and the detected amplitude is smaller.

Figure 7.13 illustrates how the theoretical sensitivity changes for different values of $\cos\iota$. The most favorable orientations lead to lower $h_{0,\mathrm{min}}$ and larger detectable distances, while edge-on systems are more difficult to detect.

Dependence on CR threshold

The theoretical sensitivity also depends on the adopted critical ratio threshold. A larger threshold requires a more significant candidate and therefore a stronger signal.

Figure 7.14 shows the predicted sensitivity for several values of CR_{thr}. As the threshold increases, the minimum detectable strain becomes larger and the corresponding maximum detectable distance decreases.

This behavior reflects the trade-off discussed earlier: stricter candidate selection reduces the false alarm probability, but it also reduces sensitivity to weaker signals.

7.6.2 Empirical sensitivity

The theoretical sensitivity derived in the previous section is based on the assumption that the detector noise is Gaussian and stationary. In practice, real detector data deviate from this ideal behaviour. Noise fluctuations, and transient disturbances introduce non-Gaussian features. These effects can influence the performance of the search pipeline. For this reason, it is necessary to evaluate the sensitivity directly on real data. This is done through simulated signal injections, which allow us to measure how efficiently the pipeline can recover signals in realistic conditions.

For each set of injections (as described in Sec. 7.4), we estimate the the maximum detectable distance, by requiring that a fixed fraction of the signals is recovered. In particular, we define the sensitivity as the distance at which 90% of the injected signals are detected. A signal is considered detected if it produces a candidate with $CR \geq CR_{\rm thr}$ and is found in coincidence across detectors. In this study, we restrict the study to the highest ellipticity sub-interval ($\epsilon \in [2.5 \times 10^{-3}, 3 \times 10^{-3}]$), which corresponds to the strongest signals in the explored parameter space to simplify the analysis. Lower ellipticities lead to smaller detectable distances but do not significantly change the overall behaviour of the efficiency curves.

Efficiency curves

For each frequency and distance, the detection efficiency is defined as the fraction of injected signals that are successfully recovered by the pipeline. It is computed as

$$\eta(D, f_0) = \frac{N_{\rm cand}(D, f_0; CR \geq CR_{\rm thr})}{N_{\rm inj}(f_0)} \times 100\%, \tag{7.11}$$

where $N_{\rm inj}(f_0)$ is the number of injected signals at a given initial frequency f_0, and $N_{\rm cand}$ is the number of those injections that are recovered with a candidate satisfying the threshold $CR \geq CR_{\rm thr}$ and passing the coincidence criteria across detectors. The efficiency is evaluated for different source distances, allowing us to construct efficiency curves as a function of D for each frequency.

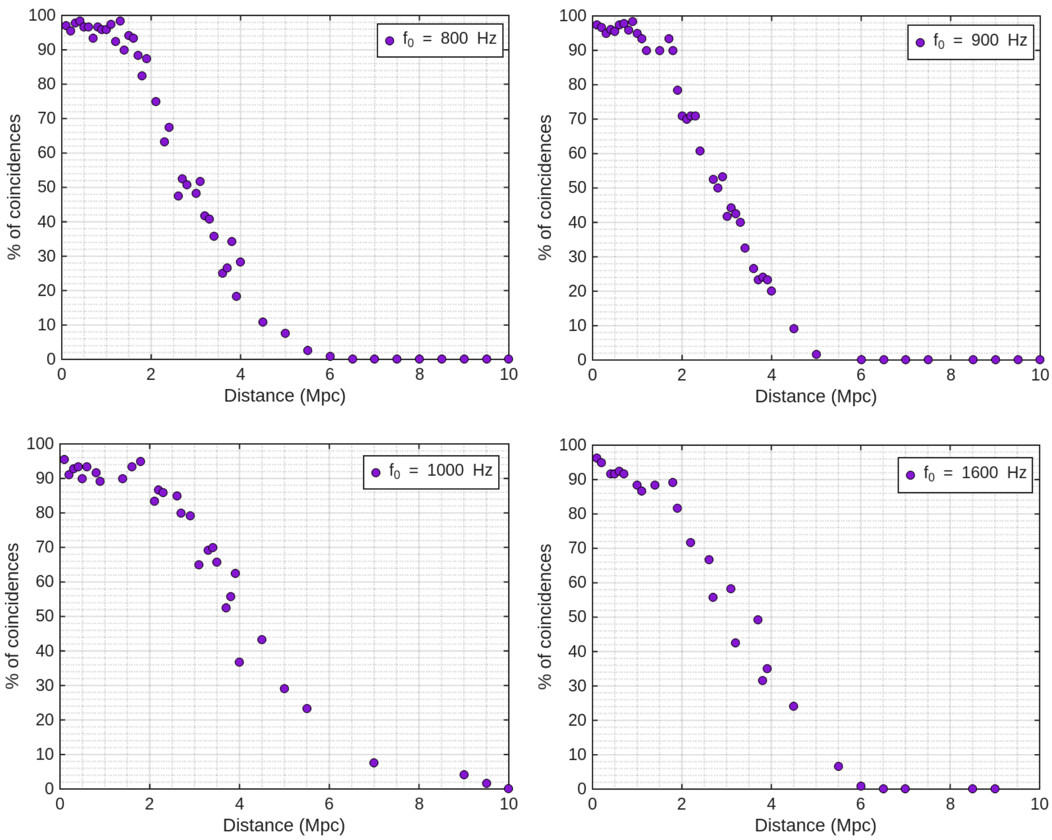

Figure 7.15. Detection efficiency as a function of source distance for selected initial frequencies. Each curve shows the fraction of injected signals that are recovered by the pipeline. The efficiency decreases with distance as the signal amplitude becomes weaker.

Figure 7.15 shows examples of efficiency curves for different initial frequencies. At small distances, the injected signals are strong and are almost always detected, so the efficiency is close to 1. As the distance increases, the signal amplitude decreases, and the efficiency gradually drops. At sufficiently large distances, the signals become too weak to be detected, and the efficiency approaches zero.

Sensitivity calculation from efficiency curves

The empirical sensitivity is obtained from the efficiency curves by identifying the distance at which the detection efficiency reaches 90%. We denote this distance as $D_{\max}$. For each frequency, the injections are ordered by increasing distance. We then identify two points: the largest distance at which the efficiency is still above 90%, and the next distance at which the efficiency falls below 90%. These two points define a small interval that brackets the desired value of $D_{\max}$. The final estimate of $D_{\max}$ is obtained by linear interpolation between these two points.

This procedure is based directly on the discrete set of injection results and does not assume any particular functional form for the efficiency curve. Although one could estimate the 90% crossing using a smooth fit to the data, the approach adopted here avoids extrapolation beyond the data points and provides a simple and data-driven estimate. Figure 7.16 illustrates the procedure used to determine the maximum detectable distance. In the upper panel, the horizontal line marks the 90% efficiency level, while the intersection with the efficiency curve defines the corresponding distance. The uncertainty on $D_{\max}$ is estimated from the spacing between the two neighboring distance points used in the interpolation as shown in asymmetric error bars.

The values of $D_{\max}$ obtained at different frequencies are combined to produce the overall sensitivity curve of the pipeline, shown in the lower panel of Fig. 7.16. This curve represents the maximum distance at which signals can be detected with 90% efficiency as a function of frequency.

7.6.3 Comparison between theoretical and empirical Estimates

Figure 7.17 presents the comparison between the empirical maximum detectable distances obtained from injection studies and the corresponding theoretical sensitivity estimates across the analyzed frequency range.

Overall, the empirical sensitivity follows the theoretical trend, although deviations up to a factor of ~ 2 are observed in certain frequency bands. In some bands, the empirical $D_{\max}$ falls below the theoretical prediction, typically in regions affected by strong spectral features, such as suspension violin modes and their harmonics [151] (as highlighted by the shaded gray regions in Fig. 7.17). These disturbances raise the local noise level and reduce the recovery efficiency, leading to a lower measured sensitivity relative to the theoretical expectation.

Conversely, at some frequencies, the empirical sensitivity exceeds the theoretical one, sometimes by factors of 1.5-2. One possible explanation is that the theoretical sensitivity curve is based on a conservative assumption: at each frequency, it uses the maximum of the H1 and L1 detector PSDs. This choice effectively corresponds to adopting the noisier of the two detectors at that frequency, and therefore provides

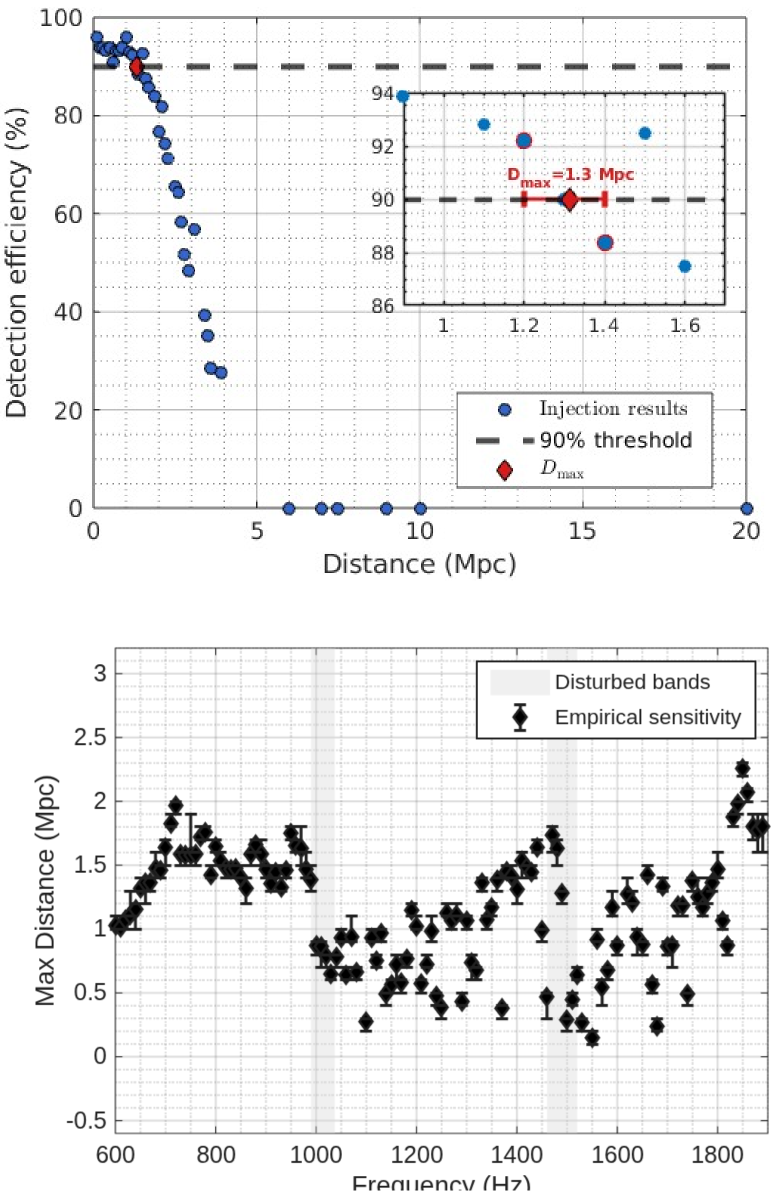

Figure 7.16. Determination of the empirical sensitivity of the pipeline from injection studies using O4a data for ellipticity $\epsilon \in [2.5 \times 10^{-3}, 3 \times 10^{-3}]$ and a critical ratio threshold $CR_{\mathrm{thr}} = 7$. Top: Detection efficiency as a function of distance for a representative frequency ($f_0 = 1400$ Hz). The maximum detectable distance, $D_{\max}$, is obtained by linear interpolation at the 90% detection efficiency level, with the horizontal bars indicating the associated uncertainty. Bottom: Empirical sensitivity curve, showing $D_{\max}$ as a function of the initial signal frequency, corresponding to a 90% detection efficiency.

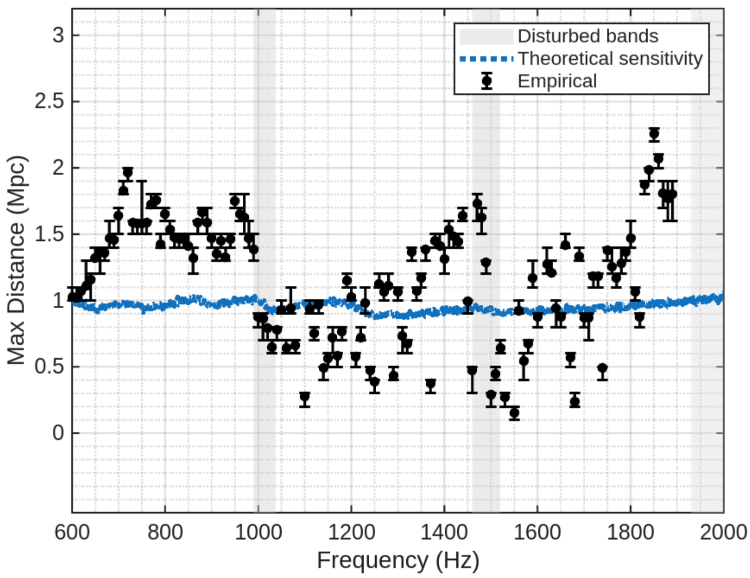

Figure 7.17. Comparison between the empirical maximum distance obtained from signal injections and the theoretical sensitivity estimate across the analyzed frequency range, for the upper ellipticity sub-interval $\epsilon \in [2.5 \times 10^{-3}, 3 \times 10^{-3}]$, using a 90% confidence level and $CR_{\text{thr}} = 7$. The theoretical sensitivity here uses a 10-day PSD corresponding to the effective duration of the injections in the upper ellipticity sub-interval, taking the maximum value between H1 and L1 detectors to remain conservative. The shaded gray regions indicate frequency bands affected by instrumental disturbances [151], which lead to a degradation of the empirical sensitivity.

a conservative estimate of the noise level. As a result, the predicted sensitivity is slightly underestimated.

Overall, the comparison indicates that the empirical results are consistent with theoretical expectations at the order-of-magnitude level, capturing the main trends while naturally reflecting real data variations.

7.6.4 Comparison of detector sensitivity across O4

The sensitivity studies presented in the previous sections were performed using O4a data. To assess how representative these results are of the detector performance over the complete O4 observing run, we compare the average noise spectra from O4a, O4b, and O4c.

As shown in Fig. 7.18, the three observing periods have similar noise levels over the 600–2000 Hz frequency range considered in this work. Relative to O4a, the median ASD is lower by approximately 5-7% in L1 and 8-10% in H1 during O4b and O4c. The later parts of O4 therefore show a modest improvement in detector sensitivity compared with the O4a data used in this study.

Although the full GFH-v2 sensitivity analysis was not repeated using O4b and O4c data, this comparison suggests that the sensitivity obtained with O4a provides a reasonable estimate of the performance expected during O4, with some improvement expected for the later periods. For a directed long-transient search, however, the

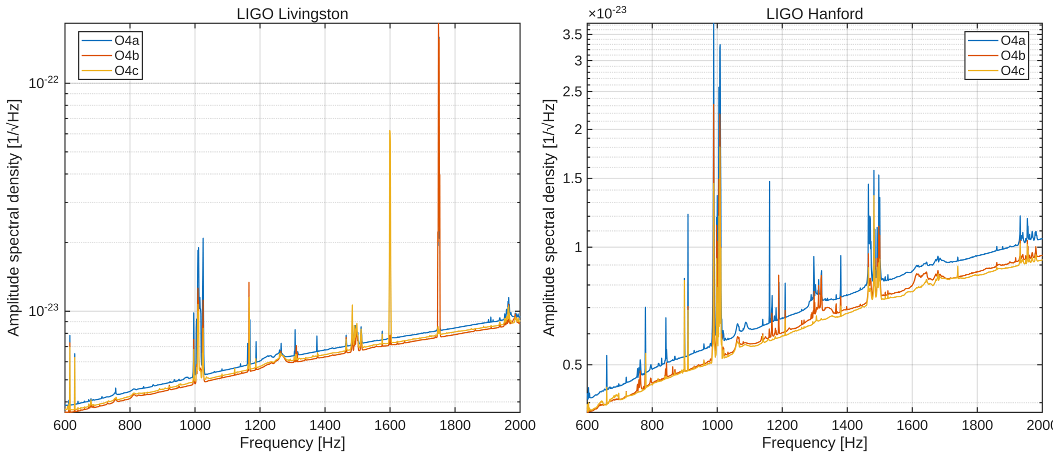

Figure 7.18. Comparison of the average noise amplitude spectral densities during O4a, O4b, and O4c for the LIGO Livingston and Hanford detectors. The spectra are obtained from the SFDB data using the same weighted averaging procedure.

actual sensitivity depends on the detector noise and data availability around the time of the astrophysical event.

7.7 Conclusion

In this chapter, we presented the development and validation of the GFH-v2 pipeline for the search of long-transient gravitational-wave signals from newborn magnetars. The search parameter space was defined using astrophysical considerations, and the choices of coherence time, observation time, and frequency range were optimized to balance sensitivity and computational cost.

Several algorithmic improvements were introduced with respect to the previous version of the pipeline, resulting in a more efficient analysis. The performance of GFH-v2 was evaluated using simulated tCW signals injected into real O4a LIGO data. The recovery studies showed that the pipeline is able to detect signals over a wide range of source parameters and distances. A comparison with the O4b and O4c noise spectra also shows that the O4a data used for the validation are broadly representative of the detector sensitivity during O4, with modest improvements in the later observing periods.

Overall, these results demonstrate that GFH-v2 provides a reliable and computationally efficient framework for directed searches for long-transient gravitational-wave signals. Having validated its performance, the pipeline is now ready to be applied to real astrophysical targets. In the next chapter 8, GFH-v2 is used to perform a directed search for long-transient gravitational-wave emission from the possible compact remnant of SN 2023ixf.

Chapter 8

Search for the SN2023ixf Remnant in ER15 Data

This chapter presents the search for long-transient gravitational waves associated with the possible magnetar remnant of SN 2023ixf using data from LIGO Engineering Run 15 (ER15). We first summarize the astrophysical properties of the supernova and the available electromagnetic observations. We then describe the ER15 dataset, the parameter space explored in the search, the candidate selection procedure, and the follow-up analysis. Finally, since no candidate survives the follow-up stage, we estimate upper limits on the maximum detectable distance of the source for different signal parameters. The results presented in this chapter form the basis of a manuscript currently in preparation for submission to Physical Review D.

8.1 SN 2023ixf: discovery and basic properties

The supernova SN 2023ixf was discovered on 19 May 2023 by the Japanese amateur astronomer Koichi Itagaki in the nearby spiral galaxy M101 (also known as the Pinwheel Galaxy) [146]. It was quickly confirmed and classified as a Type II core-collapse supernova based on its spectral features [152], which show strong hydrogen lines typical of explosions of massive stars that still retain their outer hydrogen envelope, including narrow emission features associated with photo-ionized circumstellar material (CSM) [153].

SN 2023ixf is located at right ascension $\alpha = 14^{\mathrm{h}}03^{\mathrm{m}}38.580^{\mathrm{s}}$ and declination $\delta = +54^{\circ}18'42.10''$, located in the southeastern spiral arm of M101. The host galaxy M101 is one of the closest star-forming galaxies to the Milky Way. Distance measurements place it at approximately 6.85 Mpc, making SN 2023ixf one of the nearest core-collapse supernovae observed in recent decades.

Because of this proximity, SN 2023ixf has been considered an important target for multi-messenger astronomy [154]. It has been extensively observed across the electromagnetic spectrum, and also targeted in neutrino, gamma-ray, and gravitational-wave searches [155, 156]. Such supernovae are of particular interest because they may leave behind a rapidly rotating neutron star (a magnetar), which can potentially emit long-transient gravitational waves due to asymmetries in its shape or strong magnetic field.

Figure 8.1. Host galaxy M101 with SN 2023ixf. Credit: Florian Rünger (2023), CC BY-SA 4.0, via Wikimedia Commons.

The progenitor is consistent with a red supergiant star [154]. Early-time observations suggest interaction with circumstellar material, indicating that the star underwent significant mass loss before explosion. This is important because such environments are also associated with conditions that may produce rapidly spinning neutron star remnants.

8.2 Electromagnetic observations

SN 2023ixf was extensively monitored across the electromagnetic spectrum shortly after its discovery. The early-time data provide strong constraints on both the explosion epoch and the circumstellar environment.

Optical photometry shows a very fast initial rise, followed by a bright peak within $\sim$ 5-6 days. The early light curve exhibits a multi-component structure, with an initial steep rise likely powered by shock cooling or shock breakout in dense CSM, followed by a slower rise consistent with photon diffusion in the expanding ejecta [157, 158]. This behaviour is not typical of standard Type II-P supernovae and supports the presence of confined CSM close to the progenitor.

Early spectroscopy (within $\sim$ 1-3 days) reveals a hot blue continuum with narrow emission lines of H, He, C, and N, often referred to as "flash-ionization" features [153, 159]. These lines are produced by recombination in dense CSM that has been photo-ionized by the initial UV/X-ray flash from shock breakout. The line profiles show narrow cores and broader electron-scattering wings, indicating that

Property	Value
Discovery date	19 May 2023 [146]
Type	Type II core-collapse supernova
Host galaxy	M101 (Pinwheel Galaxy)
Distance	∼6.85 Mpc
Coordinates	RA=210.91075°, DEC=54.311694°
Progenitor mass	∼8-15 $M_\odot$
EM counterpart	Optical, X-ray, radio emission

Table 8.1. Main properties of SN 2023ixf.

the CSM is both dense and optically thick at early times [160].

The flash-ionization phase lasted only a few days, after which the spectra transitioned to typical Type II P-Cygni profiles as the photosphere receded into the SN ejecta. This transition marks the point at which the forward shock had largely crossed the inner CSM shell, and the system became dominated by expanding ejecta rather than CSM interaction.

Multi-wavelength observations further support this interpretation. X-ray emission was detected within days of explosion and reached luminosities up to $\sim 10^{40}$ erg s^{-1}, consistent with shock heating in dense CSM [161]. Radio emission was initially suppressed due to free-free absorption, but later became detectable once the shock reached less dense regions [162]. These observations together confirm a dense but radially confined CSM distribution.

The early electromagnetic signal is particularly important for gravitational-wave searches because it constrains the explosion time to within a narrow window. In this work, we use the explosion epoch derived from early optical and X-ray constraints to define the on-source window for the gravitational-wave analysis.

8.3 Engineering run 15

Engineering Run 15 was a commissioning data-taking period of the LIGO detectors at the Livingston (L1) and Hanford (H1) observatories, carried out shortly before the start of the fourth observing run (O4). ER15 took place from 26 April to 24 May 2023 [163].

The main purpose of engineering runs is to prepare the detectors for observing mode. During this period, the instruments are tested under near-observing conditions, including checks of calibration, detector performance, and data quality [155]. The data are not always at full observing quality, but parts of it can still be used for scientific analyses if standard quality requirements are satisfied.

ER15 was also a transition phase from commissioning to stable observing operations. During this period, the detectors were brought to improved and more stable configurations, with continued work on sensitivity, calibration, and control systems. In particular, this run was used as a preparation step for O4, including tests of the full data analysis and alert infrastructure under realistic conditions.

The explosion of SN 2023ixf occurred during this period, making ER15 the only available LIGO dataset covering the event time. Virgo was not taking data during

ER15, so this analysis uses only the two LIGO detectors.

8.3.1 Data availability

The data available for this analysis are restricted to the time window approved by the LIGO-Virgo-KAGRA Collaboration for searches associated with SN 2023ixf, spanning from 2023 May 15 14:13 UTC to 2023 May 19 17:31 UTC. This window was defined jointly for burst and long-transient searches. Therefore, the end of the analyzed interval on May 19 is not set by an assumption about the maximum duration of the expected GW signal, but by the available approved dataset for this source.

SN 2023ixf was discovered on 2023 May 19, although the explosion occurred earlier. The epoch of SN first light- the moment when optical emission first emerged from the stellar surface is estimated to be MJD 60082.743 ± 0.083, corresponding to 2023 May 18 $\approx$17:50 UTC, approximately 0.98 days before the optical discovery [164]. The actual core collapse and neutron star formation occurred shortly before this, as the shock takes some time to travel from the collapsing core to the stellar surface. The gravitational-wave emission from a newly born magnetar remnant would therefore begin slightly earlier than first light. We therefore search the available coincident H1-L1 data within the conservative on-source window adopted for SN 2023ixf [155].

The full approved window contains nine coincident H1-L1 science segments. But not all of them are suitable for this search. The first four segments (ending before GPS 1368337146) are either short in duration or occur more than two days before the estimated explosion epoch, making them unlikely to contain a long-transient signal from the remnant. The last two segments (starting from GPS 1368547400) occur after a gap of more than two hours and are each only a few hundred seconds long, too short to contribute meaningfully to the analysis. Their contribution to a long-transient search is therefore negligible compared with the three central segments, and they are not included in the analysis.

We therefore use the three central coincident segments listed in Table 8.2, starting from GPS 1368350720 (2023 May 17 09:25 UTC), which is approximately 32 hours before the estimated first-light epoch. This provides coverage before the expected electromagnetic emergence of the supernova and allows for the uncertain delay between core collapse and first light.

Segment	GPS start	GPS end	Duration
1	1368350720	1368371200	20480 s ($\sim$5.7 hr)
2	1368418766	1368436239	17473 s ($\sim$4.9 hr)
3	1368449835	1368460501	10666 s ($\sim$3.0 hr)
Total			48619 s ($\approx$0.56 days)

Table 8.2. Coincident H1-L1 science segments used in this search. GPS times are given together with approximate durations.

The total coincident data amounts to approximately 48 600 s ($\approx$ 0.56 days), with a duty cycle of roughly 45% over the selected window. The full time span from the start of the first segment to the end of the last, including the gaps between

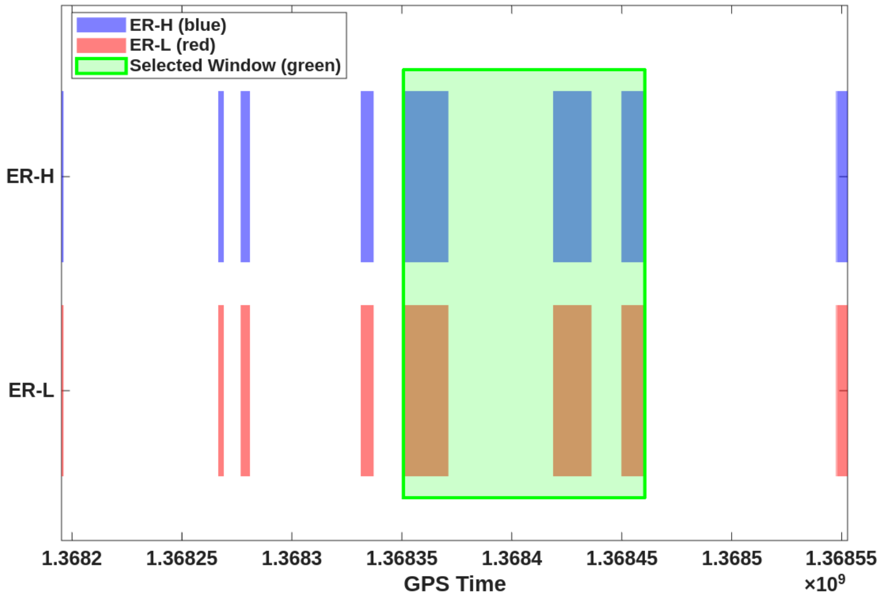

Figure 8.2. Distribution of coincident H1-L1 science segments in the ER15 analysis window.The green shaded region indicates the interval containing the three central coincident segments selected for this search. Additional coincident data are present outside this interval, but consist of shorter and more isolated segments. The selected interval spans approximately 1.27 days including gaps.

them, is about 1.27 days. This total window is what determines the maximum signal duration that can be tracked in this search.

The gaps between segments do not prevent the analysis. The GFH-v2 pipeline works on short Fourier transforms of fixed length, so it processes each segment independently and does not need continuous data. But the 1.27 day span of the selected dataset limits the signal evolution that can be tested with these data. The search therefore covers only the part of the long-transient signal that falls within the available coincident data.

The distribution of segments within the analysis window is shown in Fig. 8.2.

8.3.2 Spectral comparison with O4a

To assess the quality of the ER15 data, we compare its PSD with the noise curves from the O4a observing run. Since the sensitivity of a search depends directly on the detector noise level, this comparison provides a useful benchmark for evaluating the expected search performance.

The ER15 spectra are computed from the SFDB data using the same procedure described in Sec. 7.3.2 for the O4a data. For ER15, the calculation uses the three coincident H1-L1 science segments selected for the search, while the O4a spectra are computed using the full O4a science dataset. The power spectra of the individual FFT segments belonging to science time are combined using a weighted averaging procedure that reduces the contribution of noisier spectra [31, 131].

Figure 8.3 compares the PSD of the ER15 data with the corresponding O4a

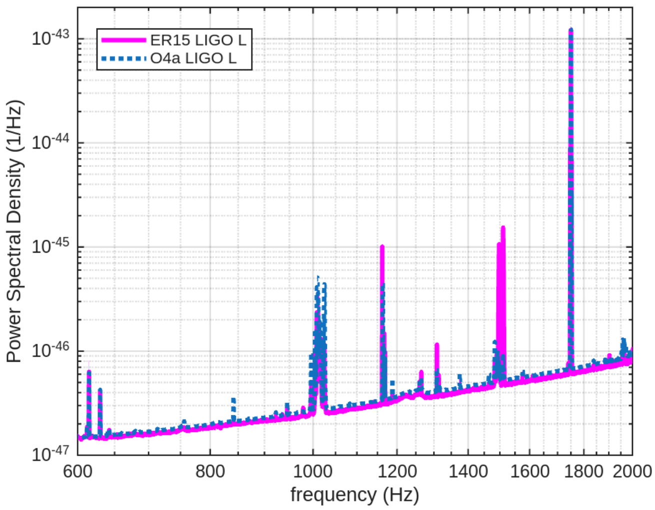

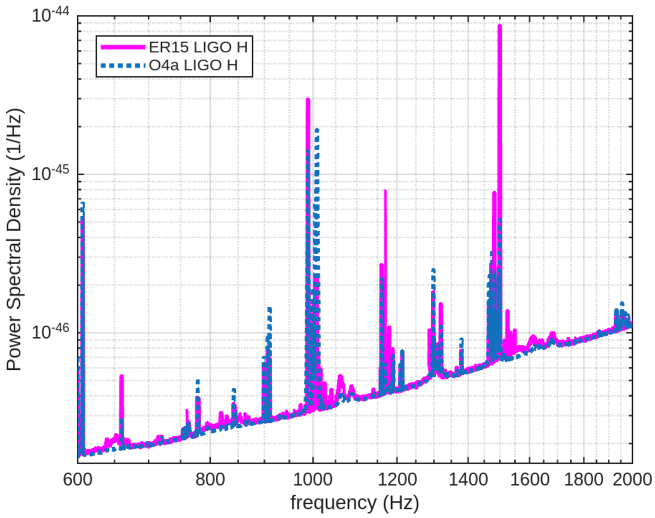

Figure 8.3. Comparison of the power spectral density of ER15 data with O4a sensitivity curves. The upper panel shows the L1 detector and the lower panel shows the H1 detector. In both detectors, the ER15 sensitivity follows a similar overall spectral shape across the analysed frequency range. The comparison indicates that the ER15 data quality is sufficient for performing a meaningful long-transient gravitational-wave search.

detector sensitivity. The overall shape of the spectra is similar in both detectors, indicating that the dominant noise sources affecting the interferometers during ER15 are comparable to those present during standard observing conditions.

The comparison shows that the ER15 sensitivity is slightly worse than, but still broadly consistent with, early O4 data over the analysed frequency band. Some excess noise is visible in specific frequency regions, but the overall shape and level of the PSD remain similar. This confirms that ER15 data has enough quality to be used for a meaningful gravitational-wave search.

8.4 Parameter space explored

The search is carried out over the parameter space defined in Sec. 7.1.1, where the choice of ranges of the physical parameters is motivated and validated.

The initial frequency f_0 is chosen between 600 Hz and 2000 Hz, divided into 10 Hz steps. This choice provides a good balance between resolution and computational cost, and is consistent with the setup used in the validation studies discussed in the previous chapter.

We select a ellipticity range between $\epsilon \in [3 \times 10^{-4}, 3 \times 10^{-3}]$. Lower ellipticities would produce longer-lived signals requiring more data to accumulate sufficient signal-to-noise ratio, and are therefore not accessible with the limited ER15 dataset. This range is further divided into five sub-intervals in order to explore different signal strengths.

In total, the search covers $140 \times 5 = 700$ independent configurations, each of which is processed separately through the full GFH-v2 pipeline as described in Chapter 7. The size of the corresponding (x_0, k) Hough maps varies between configurations because the parameter ranges and grid resolutions depend on the signal parameters. The analysed configurations contain approximately 10^6-10^7 Hough-map grid points each. Overall, the search explores of order 10^9 grid points, illustrating the computational scale of the analysis.

8.4.1 Critical ratio estimation

In previous work [34], the critical ratio (CR) was computed using the mean and standard deviation estimated over the full Hough map obtained from the peakmap, spanning the entire frequency range under consideration. While this approach provides a global characterization of the noise background, it implicitly assumes statistical stationarity of the noise across the full parameter space.

However, in the present analysis we observe that noise properties are not uniform over wide frequency intervals. In particular, variations in the detector noise spectral density and the presence of spectral artifacts introduce non-uniform fluctuations in the Hough map as a function of frequency. This effect becomes especially relevant in the context of the present search, where the analysis is performed over frequency bands that depend on the initial signal frequency f_0 and on the corresponding spin-down evolution. As a consequence, estimating the CR using global statistics may lead to a suboptimal characterization of the local noise background, potentially affecting the ranking of candidates.

To address this limitation, we adopt a localized estimation of the noise statistics. Specifically, for each value of f_0, the CR is computed using the mean and standard deviation evaluated over a restricted Hough map constructed within a narrow frequency interval of width 10 Hz centered around the corresponding search band. Within such a limited frequency range, the noise properties can be reasonably approximated as stationary, leading to a more reliable estimate of the background distribution.

The critical ratio is thus defined as

$$\mathrm{CR} = \frac{y - \mu_{\mathrm{loc}}}{\sigma_{\mathrm{loc}}}, \tag{8.1}$$

where y is the number count in a given Hough map bin, while μ_{loc} and σ_{loc} denote the mean and standard deviation computed over the reduced (local) Hough map.

The validity of this approach has been assessed through injection studies performed on ER data. These tests demonstrate that the localized estimation improves the consistency of the CR across different frequency regions.

8.4.2 Critical ratio threshold using false alarm estimation

In order to identify significant candidates in the data, it is necessary to define a threshold on the critical ratio. This is quantified through the false alarm probability, which represents the probability that noise alone produces a candidate above the chosen threshold. In this work, we require the false alarm probability to be below 0.1%. This ensures that only a very small fraction of noise fluctuations are selected as candidates, making the search more robust.

To estimate the false alarm probability, we follow the same procedure described in Section 7.5.4. From this study, we select a threshold value of $CR_{\mathrm{thr}} = 3.5$, which satisfies the requirement that the false alarm probability remains below 0.1% across the analyzed parameter space.

Although the optimal threshold may vary slightly with frequency and ellipticity due to changes in noise properties, we adopt a single conservative value for the entire analysis.

8.4.3 Computational implementation

The search was performed using 700 independent HTCondor jobs submitted to the INFN CNAF computing cluster[1], where each job corresponds to a specific combination of frequency and ellipticity interval. Each job ran on a single CPU core and processed one complete search configuration, covering peakmap construction, Hough transform, and candidate selection.

The jobs were distributed across heterogeneous computing nodes of the CNAF cluster, with different processor architectures and computing performance. The performance of the allocated CPUs is characterized by the HEPSCORE benchmark; for the nodes used in this analysis, the HEPSCORE per core ranged from approximately 11 to 25. The execution time depends strongly on the search configuration, mainly because the coherence time, observation time, and analysed frequency band vary with f_0 and ϵ.

The total computational cost is approximately 61.4 CPU-hours. Since all jobs are independent, they can be run in parallel, which makes the workflow suitable for distributed computing systems. Although the present analysis was performed using CPU resources, a GPU implementation of the GFH pipeline is also available and can be used to reduce the computational cost of future searches [34]. Overall, the pipeline is computationally efficient and can be scaled to larger parameter spaces without significant difficulty.

[1] CNAF is the national computing facility of the Italian Institute for Nuclear Physics (INFN) and serves as Italy's Tier-1 centre for the Worldwide LHC Computing Grid (WLCG), providing large-scale distributed computing resources for high-energy physics and astroparticle experiments.

8.5 Search results

After constructing the peakmaps and applying the GFH-v2 transform, candidates are selected independently in each detector. A coincidence condition is then applied to identify candidates that are consistent between the two detectors which significantly reduces the number of noise-induced candidates.

After applying both the coincidence requirement and the critical ratio threshold, a total of 131 candidates are obtained. These candidates correspond to the most significant outliers in the dataset and are therefore selected for further investigation.

The coincident candidates are not distributed uniformly across the search configurations. This is expected because the different configurations do not correspond to identical searches: the analysed bandwidth, observation time, coherence time, and number of Hough parameter-space grid points vary with the signal parameters. Local spectral disturbances can also contribute to differences in the number of candidates between configurations.

Most candidates are consistent with noise fluctuations and detector artifacts, as expected in a wide parameter-space search. Therefore, an additional follow-up stage is required to test their consistency with a true astrophysical signal.

8.6 Candidate follow-up

The purpose of the follow-up stage is to test whether the selected candidates are compatible with a true astrophysical signal or are instead produced by noise fluctuations.

In this work, we use a heterodyne-based follow-up method similar to that described in 6.6.4. The basic idea is to remove the expected phase evolution of the signal from the data using the candidate parameters. If the candidate corresponds to a true signal, this procedure transforms it into a nearly monochromatic signal. This allows us to analyze the data with longer coherence times, which increases sensitivity and enhances the critical ratio.

To account for the finite resolution of the Hough grid, the correction is not performed only at the recovered candidate parameters. For each candidate, a 5×5 grid centred on the recovered (f_0, k) values is explored, extending by two bins in each direction. This accounts for a possible offset between the true signal parameters and the grid point identified by the search.

Before applying the follow-up procedure to the search candidates, its behaviour was tested using simulated signals injected into ER15 data. The injections were processed with the same heterodyne correction and follow-up procedure used for the search candidates. These tests showed that, when the correction is applied using parameters consistent with the injected signal, the signal becomes more concentrated in frequency and its CR increases when a longer coherence time is used.

First follow-up stage Each candidate is corrected (heterodyned) using its estimated parameters. The corrected data is then re-analyzed using a longer coherence time:

$$T_{\mathrm{FFT,new}} = 3 \times T_{\mathrm{FFT,old}}. \tag{8.2}$$

If the candidate is due to a real signal, its power becomes more concentrated in frequency, and the CR is expected to increase.

Candidate selection For each candidate, the CR obtained after the first follow-up, CR_{FU}, is compared with that obtained in the original search, CR_{search}. The criterion used to retain a candidate is

$$CR_{\mathrm{FU}} > CR_{\mathrm{search}}. \tag{8.3}$$

This criterion tests whether the candidate becomes more significant when the data are corrected according to its expected signal evolution and analysed with a longer coherence time. Candidates for which the CR does not increase are rejected.

Second follow-up stage The surviving candidates are further analyzed using an even longer coherence time:

$$T_{\mathrm{FFT,new}} = 6 \times T_{\mathrm{FFT,old}}. \tag{8.4}$$

A real signal is expected to remain consistent with the applied correction and to continue gaining significance, providing an additional consistency test.

In this analysis, none of the candidates showed a consistent increase in critical ratio during the first follow-up stage. As a result, no candidates were selected for the second stage. This indicates that all identified candidates are consistent with noise fluctuations, and no evidence for a gravitational-wave signal associated with SN 2023ixf is found in the analyzed data.

8.7 Upper-limit estimation

Since none of the candidates survived the follow-up stage, we proceed with the estimation of upper limits on the maximum detectable distance. In the context of this search, the upper limit represents the maximum distance at which at least 90% of simulated signals are recovered above the loudest coincident outlier found in the actual search. More specifically, for each point in the parameter space, the upper limit corresponds to the largest distance at which at least 90% of the injected signals are recovered with a critical ratio greater than or equal to the maximum critical ratio observed in the search.

In order to do this, for each ellipticity subinterval and each frequency band, we first identify the maximum critical ratio, CR_{max}, among the coincident candidates obtained in the search and subsequently rejected by the follow-up. This value is then used as the reference threshold for the upper-limit estimation. We inject simulated signals into the same dataset using the same search setup and parameter ranges adopted in the analysis. The injections are repeated at increasing distances in order to determine how far the source can be placed while still allowing the pipeline to recover at least 90% of the signals with $CR \geq CR_{\mathrm{max}}$ and with coincidence between the two detectors.

It is important to distinguish CR_{max} from the fixed search threshold $CR_{\mathrm{thr}} = 3.5$. The latter is used in the initial search to select significant candidates, whereas CR_{max}

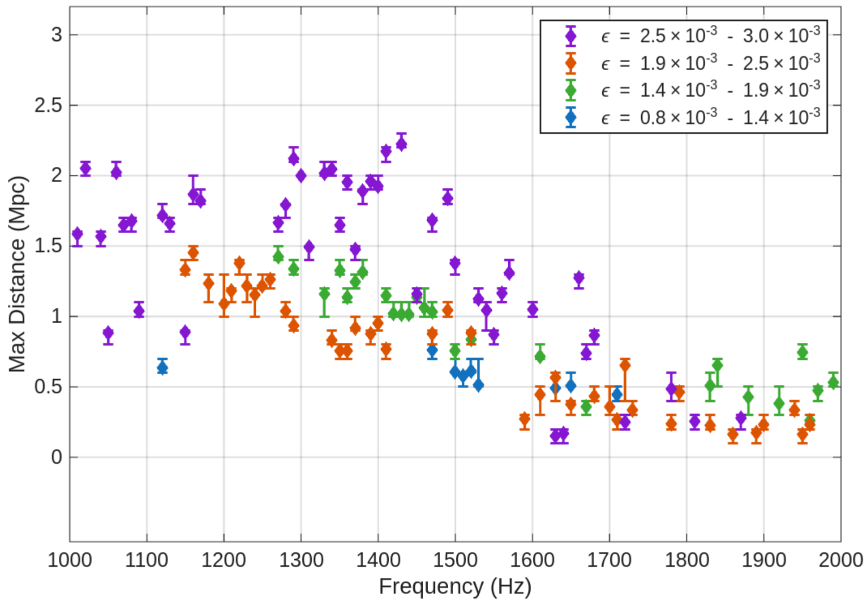

Figure 8.4. Upper limits expressed as the maximum detectable distance (defined as in Ref. [34]) as a function of the initial frequency f_0 for the different ellipticity intervals where an upper limit could be determined. Although five ellipticity intervals are included in the search, no upper limit could be determined for the lowest interval according to the procedure described in the text. Each color corresponds to a different ellipticity range.

is the critical ratio of the loudest coincident candidate actually observed in a given region of parameter space. The upper-limit procedure therefore requires an injected signal to be at least as significant as the loudest outlier found in the real search, rather than only exceeding the initial candidate selection threshold.

With this definition, an upper limit can only be assigned to regions where at least one coincident candidate is present in the original search, since otherwise there is no measured CR_{max} against which the injections can be compared. One could instead use the fixed threshold $CR_{\mathrm{thr}} = 3.5$ in regions without candidates, but this would correspond to a detection-efficiency estimate such as that used in the validation study of Chapter 7, rather than the upper-limit procedure adopted here. This condition mainly affects the lower ellipticity intervals. In addition, for some low-ellipticity and low-frequency configurations where a coincident candidate is present, the injected signals do not reach 90% recovery efficiency even at very small distances. No upper limit is reported in either case.

The difficulty in recovering the low-ellipticity signals is consistent with the limited duration of the ER15 dataset. These signals evolve more slowly and require longer observation times to accumulate sufficient signal power. Additional injection tests using longer O4a data stretches show that such signals become recoverable when more data are available. Therefore, the absence of an upper limit in these regions should not be interpreted as an limitation of the GFH-v2 method.

The resulting upper limits are shown in Fig. 8.4. Although five ellipticity intervals are included in the search, an upper limit could not be determined for the lowest

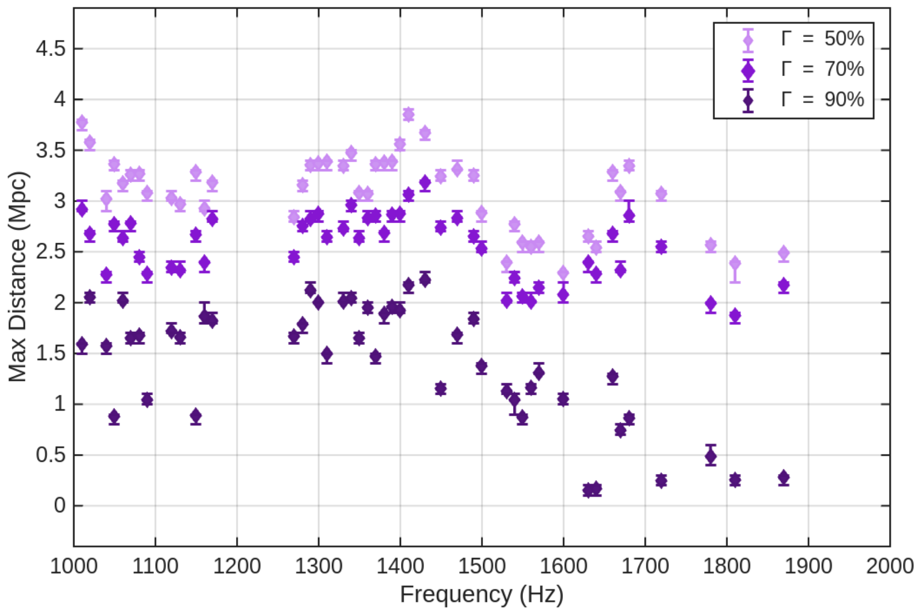

Figure 8.5. Maximum detectable distance as a function of the initial frequency f_0 for the highest ellipticity interval considered in the search. Results are shown for recovery efficiencies of 50%, 70%, and 90%.

interval according to the procedure described above. For the higher ellipticity intervals, upper limits are obtained across most of the analysed frequency range, whereas for lower ellipticities they are available only over a more restricted range.

Figure 8.5 shows the maximum detectable distance as a function of the initial frequency f_0 for the highest ellipticity interval considered in the search, using three different recovery efficiencies: 50%, 70%, and 90%. As expected, the maximum detectable distance decreases as the required recovery efficiency increases. The 90% curve provides the most conservative estimate and is adopted as the reference upper limit throughout this work.

For most of the analyzed frequency range, the 90% upper limits lie between approximately 1 and 2.5 Mpc, while the 50% upper limits reach distances of up to about 4 Mpc. Although these upper limits remain below the distance to SN 2023ixf, which is approximately 6.85 Mpc, they provide a crucial characterization of the sensitivity achieved with the ER15 dataset and quantify the performance of the pipeline under realistic observing conditions. These results also serve as a useful benchmark for testing the improvements expected from future observing runs and from the enhanced sensitivity of current and next-generation gravitational-wave detectors.

8.8 Conclusions

A directed search for long-transient gravitational waves from a possible magnetar remnant of SN 2023ixf was performed using LIGO ER15 data and the GFH-v2 pipeline. The search covered initial GW frequencies $f_0 \in [600, 2000]$ Hz and ellipticities $\epsilon \in [3 \times 10^{-4}, 3 \times 10^{-3}]$, corresponding to 700 independent search configurations. After applying coincidence requirements and a critical ratio threshold of $CR_{\text{thr}} = 3.5$, a total of 131 candidates were identified on which a two-stage follow-up analysis was done.

No candidate survived the follow-up stage. All identified candidates are consistent with noise fluctuations, and no evidence for gravitational-wave emission associated with SN 2023ixf is found in the ER15 data. Upper limits on the maximum detectable distance were estimated for different signal parameters. For the highest ellipticity interval, the 90% upper limits reach 1-2.5 Mpc across the analysed frequency band, below the distance to M101 (≈ 6.85 Mpc).

These results demonstrate that the GFH-v2 pipeline can be successfully applied to real detector data in a directed search for a specific astrophysical event. Future observations of nearby core-collapse supernovae with O5 and next-generation detectors, combined with improved pipeline sensitivity will extend the detectable distance.

Chapter 9

Discussion and Conclusions

9.1 Summary of results

The main aim of this thesis was to study long-transient gravitational waves from newly born magnetars and to develop methods to search for these signals in gravitational-wave detector data.

The first part of the work focused on the astrophysical properties of newborn magnetars and the gravitational waves they are expected to produce. In particular, the connection between gravitational-wave signals and electromagnetic counterparts was explored. Using models of magnetar-driven shock breakout emission, we estimated how detectable these events could be with future ultraviolet missions. The results show that instruments like ULTRASAT could provide useful electromagnetic triggers for gravitational-wave searches [38].

The second part of the thesis focused on data-analysis methods for long-transient signals. After reviewing the Generalized Frequency Hough method, an improved version called GFH-v2 was validated and optimized for long-transient searches through physically motivated choices of the search parameters and extensive injection studies. This new pipeline includes physically motivated choices for parameters such as coherence time, observation time, and frequency range, along with improvements in the computational implementation. Tests using real O4a data and simulated signals show that the pipeline can recover long-transient signals across a wide parameter space while remaining computationally efficient [34].

Finally, the GFH-v2 pipeline was used in a directed search for long-transient gravitational waves from the possible remnant of SN 2023ixf using LIGO ER15 data. No candidate survived the follow-up analysis. Upper limits were placed on the signal parameters. Although no evidence of a signal was found, this study shows that the GFH-v2 framework can be applied to real data for nearby core-collapse supernova remnants.

The work in this thesis has led to scientific publications. The study of magnetar-driven shock breakouts and ULTRASAT prospects was published in [38], where the author is first author. The GFH-v2 development and validation study has been published in Physical Review D [34]. The search methodology was also presented in the proceedings of the 24th International Conference on General Relativity and Gravitation (GR24) and the 16th Edoardo Amaldi Conference on Gravitational

Waves (Amaldi16) [165]. The SN 2023ixf directed search is being prepared for submission to Physical Review D, also with the author as first author.

9.2 Multi-messenger perspective

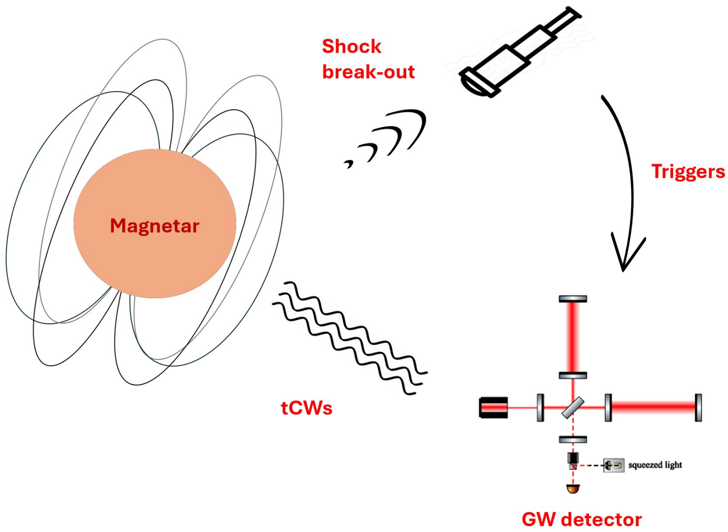

Figure 9.1. Multi-messenger connection between magnetar-powered shock breakouts and long-transient gravitational waves. Detection of the ultraviolet shock breakout provides an electromagnetic trigger that enables directed searches for the associated gravitational-wave signal from the newborn magnetar.

One of the main motivations for searching for long-transient gravitational waves is their connection with multi-messenger astronomy. Electromagnetic observations can provide the time and sky position of a newly born neutron star, which strongly reduces the search space in gravitational-wave data. In the case of magnetar-driven shock breakout signals, electromagnetic observations can also help constrain the physical properties of the source and improve predictions for the gravitational-wave signal.

A combined detection of gravitational waves and electromagnetic radiation would allow, for the first time, direct observation of the birth of a neutron star and possibly a magnetar. This would provide important information about dense matter, magnetic field evolution, and how rapidly rotating neutron stars are formed. Even a single detection would be a major milestone for gravitational-wave astronomy and would significantly improve our understanding of magnetars.

9.3 Future developments

There are several possible directions to improve and extend this work.

On the astrophysics side, more detailed models of magnetar-driven shock breakouts can be studied by including different types of progenitor stars, explosion energies, and ejecta masses. The effect of incomplete thermalization of the magnetar wind could also change the predicted electromagnetic signal and detection rates.

On the data-analysis side, an important extension of the GFH-v2 pipeline will be to relax the assumption of a known signal start time. In realistic searches, the gravitational-wave signal may not begin exactly at the start of the analysed data segment but at any time within a time window following the electromagnetic trigger. Future implementations will therefore scan over a discrete grid of possible start times, balancing parameter-space coverage, computational cost, and sensitivity. The pipeline can also be extended to include more general spin-down models, different braking indices, and effects such as fallback accretion [29, 55, 100, 108]. Further improvements could include adaptive weighting schemes that take into account variations in detector noise and sensitivity [31, 166].

Another interesting direction is to combine GFH-v2 with machine-learning methods. Recent studies have shown that machine-learning techniques can quickly identify long-transient candidates at very low computational cost and wider sky coverage [167, 168]. Even though these methods have lower sensitivity than GFH-v2, these could be used to generate candidate triggers that are then followed up with GFH-v2, combining speed with more detailed analysis.

Future observing runs of Advanced LIGO, Advanced Virgo, and KAGRA, as well as next-generation detectors like the Einstein Telescope and Cosmic Explorer, will greatly improve the sensitivity to long-transient signals. These detectors will allow us to probe much larger volumes of the Universe and will significantly improve the chances of multi-messenger observations of newborn magnetars.

9.4 Final conclusions

Long-transient gravitational waves are among the most difficult signals to detect, but they also carry very rich scientific information. The work presented in this thesis contributes to the understanding of newborn neutron stars and magnetars through both electromagnetic and gravitational-wave studies, while also improving the methodology used to search for their long-transient gravitational-wave emission.

This thesis reviewed the theoretical framework describing long-transient gravitational waves from newborn magnetars and the data analysis methods used to search for them. It also presented an electromagnetic study of shock breakout emission from newborn magnetars, highlighting the role of early electromagnetic observations in constraining the properties of compact remnants and motivating future multi-messenger searches. The GFH-v2 search methodology was then optimized and validated using extensive signal injection studies in O4a data, leading to physically motivated choices of the search parameters and a detailed assessment of the pipeline sensitivity. Finally, the validated pipeline was applied to a directed search for long-transient gravitational-wave emission from the possible compact remnant of SN 2023ixf using LIGO ER15 data.

Although no gravitational-wave signal was detected in the analyses presented here, the work establishes and validates a robust framework for future searches for long-transient gravitational-wave signals from nearby core-collapse supernovae. The combination of electromagnetic studies, methodological developments, and applications to real detector data provides a solid foundation for future searches as detector sensitivity continues to improve.

As gravitational-wave detectors become more sensitive and new electromagnetic facilities come online, the possibility of observing the birth of a neutron star through both gravitational waves and electromagnetic signals is becoming increasingly realistic. Such a discovery would provide unique insight into the physics of compact objects, improve our understanding of the formation, early evolution, and internal physics of neutron stars and magnetars, and represent a major step forward in multi-messenger astronomy.

Acknowledgements

As I write these final pages, I find myself thinking less about the physics and more about the people.

Over the past four years, this PhD has taken me across countries, research groups, conferences, and collaborations. Along the way there were challenges, doubts, and difficult periods, but also many rewarding experiences and friendships. Looking back, I realise that this thesis is not only the result of my work, but also of the support, guidance, and kindness of many people who accompanied me throughout this journey.

The first person I would like to thank is my supervisor, Prof. Pia Astone.

There are some people who leave such a deep mark on your life that it becomes difficult to describe their importance in a few paragraphs. For me, Pia is one of those people. Throughout my PhD, she was my guide, my strongest supporter, and very often the person who helped me believe in myself when I was struggling to do so. No matter how busy she was, she always found time for discussions, advice, encouragement, and help. Some problems that seemed impossible to me after weeks of struggle would suddenly become clear after a short conversation with her, and every meeting with her left me feeling more confident than when I walked in.

More than anything else, she gave me the confidence to keep going. Whenever I doubted myself, she somehow had more confidence in me than I had in myself. She celebrated every small achievement, encouraged me after every setback, and reminded me to keep going when it would have been much easier to give up. Looking back now, I know that I would not be submitting this thesis without her. She taught me much more than how to do research. She showed me what it means to be a mentor who truly cares about her students, not only as researchers but also as people. Meeting Pia has been one of the greatest gifts of these four years. I will always be grateful that, among all the people I could have had as a supervisor, I had her.

I would also like to thank my co-supervisor, Prof. Dafne Guetta, for giving me the opportunity to join this PhD programme and for the many opportunities she provided throughout it. During the beginning of my PhD, she helped me settle into a completely new environment and made the transition much easier by taking care of many practical and administrative aspects. She also played an important role in initiating my first research project, helping me get started and sharing her ideas and scientific perspective during its early stages. I am grateful for the many opportunities she gave me to present our work, attend conferences, and actively participate in the research community from an early stage of my PhD. I also sincerely appreciate the effort she invested in building and supporting this PhD programme. She was always quick to respond whenever something needed attention, and whenever something had to be arranged or resolved, she made sure it was taken care of.

I would also like to thank Sapienza University of Rome, Ariel University, and INFN Roma for the support and opportunities they provided throughout my PhD. I am grateful to both universities for making this joint PhD possible and to INFN Roma for supporting my participation in conferences and scientific meetings, which became an important part of my research journey.

I would also like to thank Prof. Andrzej Krolak and Prof. Joseph Covas Vidal for their careful evaluation of my thesis and for the thoughtful comments and suggestions they provided. Their feedback helped me improve and strengthen the final version of this work.

A special thank you goes to Cristiano Palomba. Throughout my PhD, and especially during its final stages, Cristiano was always available for discussion, clarification, and advice. Many of the scientific ideas and interpretations presented in this thesis became clearer through our conversations. No matter how basic or naive my questions seemed, he always took them seriously and helped me understand things better. His willingness to discuss science and explain concepts helped me grow as a researcher. I also sincerely appreciate his readiness to help with practical and administrative matters whenever I needed assistance.

I would also like to thank Simone Dall'Osso, who played a crucial role during the early stages of my PhD. He helped me build the foundations needed for the work and introduced me to many of the concepts that became central to my research. His explanations, patience, and guidance helped me get started during the early stages of my PhD.

I am grateful to Sabrina D'Antonio and Lorenzo Pierini for the many valuable discussions we shared throughout my PhD. Sabrina's insights and discussions helped me better understand and interpret my results, while Lorenzo's support with the analysis pipeline and its development was invaluable.

I would also like to thank everyone in the Virgo collaboration and the LVK Continuous wave community. It has been a privilege to learn from and work alongside so many talented people.

A special thank you goes to the Virgo Rome group, including professors, postdocs, students, and staff, for creating such a nice environment.

Among them, I would especially like to thank Neil Lu. When I first arrived in Rome, Neil was one of the first people who helped me navigate a completely new environment. He was a wonderful friend and a constant source of support.

I would also like to thank Francesca Attadio. If there was a problem, there was a very good chance Francesca knew how to solve it. From helping me find accommodation to helping me navigate countless practical difficulties, she made life in Rome significantly easier. Her help arrived exactly when it was needed most, more times than I can count.

I am also grateful to Francesco Amicucci and Martina Di Cesare for their friendship, kindness, and for the many enjoyable conversations and moments we shared throughout these years.

I would like to thank all the Virgo-Rome PhD students and colleagues with whom I shared this journey. Even if I cannot name everyone individually, they contributed greatly to making these years memorable.

A special thank you goes to my office mates from Room 127, especially Silvio and

Alya. Beyond our daily crossword breaks, I will always remember the conversations, laughter, and the friendly atmosphere they brought to the office. I would also like to thank everyone else who shared Room 127. Although I was often the only non-Italian in the room, I never felt left out, and it was always a pleasant place to spend the day.

I am also grateful to my Indian and Malayali friends in Italy, including Ann, Tushara, Vipul, Neethish, Hari, Akant, and many others, for the friendly company and the moments we shared during these years.

Outside academia, there are people without whom this journey would have been much harder.

To Bhagya: thank you for being my constant throughout these years. You listened to every frustration, every worry, every small success, and every moment of self-doubt. You never asked me to be less emotional, less worried, or less myself. Even while dealing with your own PhD, you always had the patience and kindness to support me. I honestly cannot imagine these years without you, and I am incredibly lucky to have you in my life.

To my best friend, Fabi: thank you for the countless calls, conversations, jokes, and moments of friendship. Time, distance, and different cities never changed our friendship, and I am grateful for that every day.

I would also like to thank my dear friends Jithu, Sree, Reshu, Gifty, Aswadh, Saju, Santhu, Navaneetha, Ayushi and many others who remained part of my life throughout these years. Whether near or far, your friendship mattered more than you know. A special mention goes to the IISER TVM community across different batches in Europe, with whom I shared many trips, gatherings, and moments that truly made it feel like a home away from home. There are many of you, and even if I cannot name everyone individually, I carry those memories with great gratitude.

To Sruthy: I don’t really know how to put you in formal words, so I won’t try. You’re just... you. My constant support, my daily dose of chaos and calm, and somehow the person who always makes everything feel okay again. I don’t say it often, but I somehow ended up with the best sister.

To Achan and Amma: thank you for your love, support, and for everything you have done for me throughout my life. This thesis is only one small chapter of a much longer story that would not exist without you.

I would also like to thank Giulia and her family for welcoming me into their home during my years in Rome. I am grateful for their kindness and for the warm and comfortable environment they created. I especially want to thank Mercy, with whom I often shared conversations about our daily lives whenever she was around. Those small everyday moments made life in Rome a little more familiar and warm.

Finally, I would like to thank two teachers who helped shape the path that eventually led me here.

Ambili Teacher, my physics teacher in school, was one of the first people who made physics feel exciting and meaningful. The curiosity she inspired in me many years ago ultimately set me on the path that led to this thesis.

I am also deeply grateful to Soumen Basak. Through my master’s project, he introduced me to gravitational-wave research and helped me take my first steps into this field. Without his guidance and encouragement, I may never have become part of this community.

To everyone mentioned here, and to those whose names I may have unintentionally missed, thank you.

This thesis may have my name on its cover, but it carries a little part of all of you within it.

Bibliography

[1] A. Einstein, Sitzungsberichte der Königlich Preussischen Akademie der Wissenschaften , 688 (1916).

[2] R. A. Hulse and J. H. Taylor, The Astrophysical Journal Letters **195**, L51 (1975).

[3] B. P. Abbott *et al.*, Physical Review Letters **116**, 061102 (2016), arXiv:1602.03837 [gr-qc] .

[4] J. Aasi *et al.*, Classical and Quantum Gravity **32**, 074001 (2015), arXiv:1411.4547 [gr-qc] .

[5] F. Acernese *et al.*, Classical and Quantum Gravity **39**, 045006 (2022), arXiv:2107.03294 [gr-qc] .

[6] T. Akutsu *et al.*, Progress of Theoretical and Experimental Physics **2021**, 05A102 (2021), arXiv:2009.09305 [gr-qc] .

[7] B. P. Abbott *et al.*, Living Reviews in Relativity **21**, 3 (2018), arXiv:1304.0670 .

[8] B. P. Abbott *et al.*, Physical Review X **9**, 031040 (2019), arXiv:1811.12907 [astro-ph.HE] .

[9] R. Abbott *et al.*, Physical Review D **109**, 022001 (2024), arXiv:2108.01045 [gr-qc] .

[10] R. Abbott *et al.*, Physical Review X **13**, 041039 (2023), arXiv:2111.03606 [gr-qc] .

[11] The LIGO Scientific Collaboration, the Virgo Collaboration, and the KAGRA Collaboration, arXiv e-prints , arXiv:2508.18082 (2025), arXiv:2508.18082 [gr-qc] .

[12] The LIGO Scientific Collaboration, the Virgo Collaboration, and the KAGRA Collaboration, arXiv e-prints , arXiv:2605.27225 (2026), arXiv:2605.27225 [gr-qc] .

[13] B. P. Abbott *et al.*, Physical Review Letters **119**, 161101 (2017), arXiv:1710.05832 [gr-qc] .

[14] B. P. Abbott *et al.*, The Astrophysical Journal Letters **848**, L12 (2017), arXiv:1710.05833 [astro-ph.HE] .

[15] P. D. Lasky, Publications of the Astronomical Society of Australia **32**, e034 (2015), arXiv:1508.06643 [astro-ph.HE] .

[16] K. Riles, Living Reviews in Relativity **26**, 3 (2023), arXiv:2206.06447 [astro-ph.HE] .

[17] K. Wette, Astroparticle Physics **153**, 102880 (2023), arXiv:2305.07106 [gr-qc] .

[18] R. C. Duncan and C. Thompson, The Astrophysical Journal Letters **392**, L9 (1992).

[19] R. Prix, S. Giampanis, and C. Messenger, Physical Review D **84**, 023007 (2011), arXiv:1104.1704 [gr-qc] .

[20] C. Palomba, Astronomy & Astrophysics **367**, 525 (2001).

[21] C. Cutler, Physical Review D **66**, 084025 (2002), arXiv:gr-qc/0206051 [gr-qc] .

[22] A. Corsi and P. Mészáros, The Astrophysical Journal **702**, 1171 (2009), arXiv:0907.2290 [astro-ph.CO] .

[23] A. Sur and B. Haskell, Monthly Notices of the Royal Astronomical Society **502**, 4680 (2021), 2010.15574 [astro-ph.HE] .

[24] S. Dall'Osso and L. Stella, in *Astrophysics and Space Science Library*, Astrophysics and Space Science Library, Vol. 465, edited by S. Bhattacharyya, A. Papitto, and D. Bhattacharya (2022) pp. 245–280, arXiv:2103.10878 [astro-ph.HE] .

[25] C. A. Raithel, European Physical Journal A **55**, 80 (2019), arXiv:1904.10002 [astro-ph.HE] .

[26] N. Yunes, M. C. Miller, and K. Yagi, Nature Reviews Physics **4**, 237 (2022), arXiv:2202.04117 [gr-qc] .

[27] C. Thompson and R. C. Duncan, Monthly Notices of the Royal Astronomical Society **275**, 255 (1995).

[28] K. Riles, Progress in Particle and Nuclear Physics **68**, 1 (2013), arXiv:1209.0667 [hep-ex] .

[29] O. Hamil, J. R. Stone, M. Urbanec, and G. Urbancová, Physical Review D **91**, 063007 (2015), arXiv:1608.01383 [astro-ph.HE] .

[30] K. Riles, Modern Physics Letters A **32**, 1730035-685 (2017), arXiv:1712.05897 [gr-qc] .

[31] P. Astone, A. Colla, S. D'Antonio, S. Frasca, and C. Palomba, Physical Review D **90**, 042002 (2014), arXiv:1407.8333 [astro-ph.IM] .

[32] A. Miller *et al.*, Physical Review D **98**, 102004 (2018), arXiv:1810.09784 [astro-ph.IM] .

[33] B. P. Abbott *et al.*, The Astrophysical Journal **875**, 160 (2019), arXiv:1810.02581 [gr-qc] .

[34] S. Sajith Menon *et al.*, Physical Review D **113**, 123042 (2026), arXiv:2512.09878 [astro-ph.IM] .

[35] L. Bonolis, L. Maiani, and G. Pancheri, *Bruno Touschek 100 Years: Memorial Symposium 2021* (Springer International Publishing, 2023).

[36] E. Pian *et al.*, Nature **551**, 67 (2017), arXiv:1710.05858 [astro-ph.HE] .

[37] N. R. Tanvir *et al.*, The Astrophysical Journal Letters **848**, L27 (2017), arXiv:1710.05455 [astro-ph.HE] .

[38] S. S. Menon, D. Guetta, and S. Dall'Osso, The Astrophysical Journal **955**, 12 (2023), arXiv:2305.07761 [astro-ph.HE] .

[39] S. Dall'Osso and D. Guetta, The Astrophysical Journal **991**, 5 (2025).

[40] D. Kasen, B. D. Metzger, and L. Bildsten, The Astrophysical Journal **821**, 36 (2016).

[41] L.-D. Liu, H. Gao, X.-F. Wang, and S. Yang, The Astrophysical Journal **911**, 142 (2021).

[42] Y. Shvartzvald *et al.*, arXiv e-prints , arXiv:2304.14482 (2023), arXiv:2304.14482 [astro-ph.IM] .

[43] C. W. Misner, K. S. Thorne, and J. A. Wheeler, *Gravitation* (W. H. Freeman and Company, 1973).

[44] M. Maggiore, *Gravitational Waves. Vol. 1: Theory and Experiments* (Oxford University Press, 2007).

[45] S. Klimenko *et al.*, Physical Review D **93**, 042004 (2016), arXiv:1511.05999 [gr-qc] .

[46] B. P. Abbott *et al.*, Physical Review D **95**, 042003 (2017), arXiv:1611.02972 [gr-qc] .

[47] R. Abbott *et al.*, Physical Review D **104**, 122004 (2021), arXiv:2107.03701 [gr-qc] .

[48] W. G. Anderson, P. R. Brady, J. D. Creighton, and É. É. Flanagan, Physical Review D **63**, 042003 (2001), arXiv:gr-qc/0008066 [gr-qc] .

[49] S. Klimenko, I. Yakushin, A. Mercer, and G. Mitselmakher, Classical and Quantum Gravity **25**, 114029 (2008), arXiv:0802.3232 [gr-qc] .

[50] B. Allen and J. D. Romano, Physical Review D **59**, 102001 (1999), arXiv:gr-qc/9710117 [gr-qc] .

[51] N. Christensen, Reports on Progress in Physics **82**, 016903 (2019), arXiv:1811.08797 [gr-qc] .

[52] T. Regimbau, Research in Astronomy and Astrophysics **11**, 369 (2011), arXiv:1101.2762 [astro-ph.CO] .

[53] C. Caprini and D. G. Figueroa, Classical and Quantum Gravity **35**, 163001 (2018), arXiv:1801.04268 [astro-ph.CO] .

[54] P. Jaranowski, A. Królak, and B. F. Schutz, Physical Review D **58**, 063001 (1998), arXiv:gr-qc/9804014 [gr-qc] .

[55] A. Corsi and B. J. Owen, Physical Review D **83**, 104014 (2011), arXiv:1102.3421 [gr-qc] .

[56] J. Weber, Physical Review **117**, 306 (1960).

[57] R. Weiss, Quarterly Progress Report, MIT Research Laboratory of Electronics (1972).

[58] F. Acernese *et al.*, Classical and Quantum Gravity **32**, 024001 (2015), arXiv:1408.3978 [gr-qc] .

[59] B. Willke *et al.*, Classical and Quantum Gravity **19**, 1377 (2002).

[60] B. Iyer *et al.*, *LIGO-India Project Proposal and Technical Report*, Tech. Rep. LIGO-M1100296 (LIGO Laboratory, 2011) available at LIGO Document Control Center.

[61] R. Abbott *et al.*, SoftwareX **13**, 100658 (2021), arXiv:1912.11716 [gr-qc] .

[62] R. Abbott *et al.*, The Astrophysical Journal Supplement Series **267**, 29 (2023), arXiv:2302.03676 [gr-qc] .

[63] The LIGO Scientific Collaboration, the Virgo Collaboration, and the KAGRA Collaboration, arXiv e-prints , arXiv:2508.18079 (2025), arXiv:2508.18079 [gr-qc] .

[64] The LIGO Scientific collaboration, the Virgo collaboration, and the KAGRA collaboration, arXiv e-prints , arXiv:2605.27090 (2026), arXiv:2605.27090 [gr-qc] .

[65] LIGO Scientific Collaboration, Virgo Collaboration and KAGRA Collaboration, Ligo, virgo and kagra observing run plans, `https://observing.docs.ligo.org/plan/#timeline` (2025).

[66] M. Punturo *et al.*, Classical and Quantum Gravity **27**, 194002 (2010).

[67] D. Reitze *et al.*, in *Bulletin of the American Astronomical Society*, Vol. 51 (2019) p. 35, arXiv:1907.04833 [astro-ph.IM] .

[68] M. Branchesi *et al.*, Journal of Cosmology and Astroparticle Physics **2023** (7), 068, arXiv:2303.15923 [gr-qc] .

[69] M. Evans *et al.*, arXiv e-prints , arXiv:2109.09882 (2021), arXiv:2109.09882 [astro-ph.IM] .

[70] P. Amaro-Seoane *et al.*, arXiv e-prints , arXiv:1702.00786 (2017), arXiv:1702.00786 [astro-ph.IM] .

[71] S. Kawamura *et al.*, Classical and Quantum Gravity **28**, 094011 (2011).

[72] J. Luo *et al.*, Classical and Quantum Gravity **33**, 035010 (2016), arXiv:1512.02076 [astro-ph.IM] .

[73] J. G. Rollins, E. Hall, C. Wipf, and L. McCuller, pygwinc: Gravitational Wave Interferometer Noise Calculator, Astrophysics Source Code Library, record ascl:2007.020 (2020), ascl:2007.020 .

[74] W. Baade and F. Zwicky, Proceedings of the National Academy of Science **20**, 259 (1934).

[75] J. Chadwick, Proceedings of the Royal Society of London Series A **136**, 692 (1932).

[76] R. Giacconi, H. Gursky, F. R. Paolini, and B. B. Rossi, Physical Review Letters **9**, 439 (1962).

[77] A. Hewish, S. J. Bell, J. D. H. Pilkington, P. F. Scott, and R. A. Collins, Nature **217**, 709 (1968).

[78] A. Heger, C. L. Fryer, S. E. Woosley, N. Langer, and D. H. Hartmann, The Astrophysical Journal **591**, 288 (2003), arXiv:astro-ph/0212469 [astro-ph] .

[79] S. Chandrasekhar, The Astrophysical Journal **74**, 81 (1931).

[80] S. L. Shapiro and S. A. Teukolsky, *Black holes, white dwarfs, and neutron stars: The physics of compact objects* (Wiley, 1983).

[81] P. Haensel, A. Y. Potekhin, and D. G. Yakovlev, *Neutron Stars 1 : Equation of State and Structure*, Vol. 326 (Springer, 2007).

[82] H.-T. Janka, Annual Review of Nuclear and Particle Science **62**, 407 (2012), arXiv:1206.2503 [astro-ph.SR] .

[83] A. Burrows and J. M. Lattimer, The Astrophysical Journal **307**, 178 (1986).

[84] H. A. Bethe, Reviews of Modern Physics **62**, 801 (1990).

[85] N. Chamel and P. Haensel, Living Reviews in Relativity **11**, 10 (2008), arXiv:0812.3955 [astro-ph] .

[86] J. M. Lattimer and M. Prakash, The Astrophysical Journal **550**, 426 (2001), arXiv:astro-ph/0002232 [astro-ph] .

[87] F. Weber, Progress in Particle and Nuclear Physics **54**, 193 (2005), arXiv:astro-ph/0407155 [astro-ph] .

[88] C. Y. Tsang, M. B. Tsang, W. G. Lynch, R. Kumar, and C. J. Horowitz, Nature Astronomy **8**, 328 (2024), arXiv:2310.11588 [nucl-th] .

[89] G. Raaijmakers *et al.*, The Astrophysical Journal Letters **918**, L29 (2021), arXiv:2105.06981 [astro-ph.HE] .

[90] C. Thompson and R. C. Duncan, The Astrophysical Journal **408**, 194 (1993).

[91] R. N. Manchester, G. B. Hobbs, A. Teoh, and M. Hobbs, The Astronomical Journal **129**, 1993 (2005), arXiv:astro-ph/0412641 [astro-ph] .

[92] S. Mereghetti, Astronomy and Astrophysics Review **15**, 225 (2008), arXiv:0804.0250 [astro-ph] .

[93] V. M. Kaspi and A. M. Beloborodov, Annual Review of Astronomy and Astrophysics **55**, 261 (2017), arXiv:1703.00068 [astro-ph.HE] .

[94] C. Thompson and R. C. Duncan, The Astrophysical Journal **473**, 322 (1996).

[95] P. M. Woods and C. Thompson, *Compact stellar X-ray sources*, edited by W. H. G. Lewin and M. van der Klis, Vol. 39 (Cambridge University Press, 2006) pp. 547–586.

[96] P. Beniamini, K. Hotokezaka, A. van der Horst, and C. Kouveliotou, Monthly Notices of the Royal Astronomical Society **487**, 1426 (2019), arXiv:1903.06718 [astro-ph.HE] .

[97] D. Kasen and L. Bildsten, The Astrophysical Journal **717**, 245 (2010).

[98] B. D. Metzger, B. Margalit, D. Kasen, and E. Quataert, Monthly Notices of the Royal Astronomical Society **454**, 3311 (2015), arXiv:1508.02712 [astro-ph.HE] .

[99] B. D. Metzger, D. Giannios, T. A. Thompson, N. Bucciantini, and E. Quataert, Monthly Notices of the Royal Astronomical Society **413**, 2031 (2011), arXiv:1012.0001 [astro-ph.HE] .

[100] S. Dall'Osso, S. N. Shore, and L. Stella, Monthly Notices of the Royal Astronomical Society **398**, 1869 (2009), arXiv:0811.4311 [astro-ph] .

[101] R. Ciolfi and L. Rezzolla, Monthly Notices of the Royal Astronomical Society **435**, L43 (2013), arXiv:1306.2803 [astro-ph.SR] .

[102] R. J. Tayler, Monthly Notices of the Royal Astronomical Society **161**, 365 (1973).

[103] J. Braithwaite and Å. Nordlund, Astronomy & Astrophysics **450**, 1077 (2006), arXiv:astro-ph/0510316 [astro-ph] .

[104] R. Ciolfi, V. Ferrari, L. Gualtieri, and J. A. Pons, Monthly Notices of the Royal Astronomical Society **397**, 913 (2009), arXiv:0903.0556 [astro-ph.SR] .

[105] R. Ciolfi, V. Ferrari, and L. Gualtieri, Monthly Notices of the Royal Astronomical Society **406**, 2540 (2010), arXiv:1003.2148 [astro-ph.SR] .

[106] D. Lai and S. L. Shapiro, The Astrophysical Journal **442**, 259 (1995), arXiv:astro-ph/9408053 [astro-ph] .

[107] G. Ushomirsky, C. Cutler, and L. Bildsten, Monthly Notices of the Royal Astronomical Society **319**, 902 (2000), arXiv:astro-ph/0001136 [astro-ph] .

[108] A. L. Piro and E. Thrane, The Astrophysical Journal **761**, 63 (2012), arXiv:1207.3805 [astro-ph.HE] .

[109] A. K. Harding, I. Contopoulos, and D. Kazanas, The Astrophysical Journal Letters **525**, L125 (1999), arXiv:astro-ph/9908279 [astro-ph] .

[110] J. E. Gunn and J. P. Ostriker, Nature **221**, 454 (1969).

[111] B. J. Owen, L. Lindblom, C. Cutler, B. F. Schutz, A. Vecchio, and N. Andersson, Physical Review D **58**, 084020 (1998), arXiv:gr-qc/9804044 [gr-qc] .

[112] P. D. Lasky, C. Leris, A. Rowlinson, and K. Glampedakis, The Astrophysical Journal Letters **843**, L1 (2017), arXiv:1705.10005 [astro-ph.HE] .

[113] L. Stella, S. Dall'Osso, G. L. Israel, and A. Vecchio, The Astrophysical Journal Letters **634**, L165 (2005), arXiv:astro-ph/0511068 [astro-ph] .

[114] L. Mestel and H. S. Takhar, Monthly Notices of the Royal Astronomical Society **156**, 419 (1972).

[115] M. Shibata, T. W. Baumgarte, and S. L. Shapiro, The Astrophysical Journal **542**, 453 (2000), arXiv:astro-ph/0005378 [astro-ph] .

[116] S. Chandrasekhar, Physical Review Letters **24**, 611 (1970).

[117] J. L. Friedman and B. F. Schutz, The Astrophysical Journal **222**, 281 (1978).

[118] L. Lindblom, B. J. Owen, and S. M. Morsink, Physical Review Letters **80**, 4843 (1998), arXiv:gr-qc/9803053 [gr-qc] .

[119] N. Andersson and K. D. Kokkotas, International Journal of Modern Physics D **10**, 381 (2001), arXiv:gr-qc/0010102 [gr-qc] .

[120] S. K. Lander and D. I. Jones, Monthly Notices of the Royal Astronomical Society **494**, 4838 (2020), arXiv:1910.14336 [astro-ph.HE] .

[121] J. M. Lattimer and M. Prakash, Physics Reports **621**, 127 (2016), memorial Volume in Honor of Gerald E. Brown.

[122] S. Dall'Osso, L. Stella, and C. Palomba, Monthly Notices of the Royal Astronomical Society **480**, 1353 (2018), arXiv:1806.11164 [astro-ph.HE] .

[123] I. Sagiv *et al.*, The Astronomical Journal **147**, 79 (2014).

[124] A. Spitkovsky, The Astrophysical Journal **648**, L51 (2006).

[125] R. A. Chevalier and N. Soker, The Astrophysical Journal **341**, 867 (1989).

[126] N. Ganot *et al.*, The Astrophysical Journal **820**, 57 (2016).

[127] B. M. Gaensler *et al.*, The Astrophysical Journal Letters **620**, L95 (2005), arXiv:astro-ph/0501563 [astro-ph] .

[128] P. Madau and M. Dickinson, Annual Review of Astronomy and Astrophysics **52**, 415 (2014).

[129] N. Aghanim *et al.*, Astronomy & Astrophysics **641**, A6 (2020).

[130] P. Astone, S. Frasca, and C. Palomba, Classical and Quantum Gravity **22**, S1197 (2005).

[131] P. Astone and S. D'Antonio, Creation of the short fft data base (sfdb), oar.it (2025).

[132] R. Tenorio, D. Keitel, and A. M. Sintes, Universe **7**, 474 (2021), arXiv:2111.12575 [gr-qc] .

[133] R. Prix, in *Astrophysics and Space Science Library*, Astrophysics and Space Science Library, Vol. 357, edited by W. Becker (2009) p. 651.

[134] B. Krishnan *et al.*, Physical Review D **70**, 082001 (2004), arXiv:gr-qc/0407001 [gr-qc] .

[135] P. R. Brady and T. Creighton, Physical Review D **61**, 082001 (2000), arXiv:gr-qc/9812014 [gr-qc] .

[136] L. Sun *et al.*, Classical and Quantum Gravity **37**, 225008 (2020), arXiv:2005.02531 [astro-ph.IM] .

[137] P. Astone *et al.*, Physical Review D **65**, 022001 (2001), arXiv:gr-qc/0011072 [gr-qc] .

[138] C. Palomba, P. Astone, and S. Frasca, Classical and Quantum Gravity **22**, S1255 (2005).

[139] P. V. C. Hough, in *Proceedings of the 2nd International Conference on High-Energy Accelerators and Instrumentation (HEACC 1959)* (CERN, Geneva, Switzerland, 1959) pp. 554–558.

[140] Gravitational Wave Open Science Center, GWOSC, `https://gwosc.org/O4/O4a/` (2025).

[141] O. J. Piccinni *et al.*, Classical and Quantum Gravity **36**, 015008 (2019), arXiv:1811.04730 [gr-qc] .

[142] C. Palomba, On the sensitivity of peakmap-based methods for the search of continuous gravitational wave signals, `https://tds.virgo-gw.eu/?r=25138` (2025), public Virgo note.

[143] L. Xie, D.-M. Wei, Y. Wang, and Z.-P. Jin, The Astrophysical Journal **934**, 125 (2022), arXiv:2206.12874 [astro-ph.HE] .

[144] C.-Y. Song and T. Liu, The Astrophysical Journal **952**, 156 (2023), arXiv:2301.05401 [astro-ph.HE] .

[145] S. Dall'Osso and L. Stella, Astrophysics and Space Science **308**, 119 (2007), arXiv:astro-ph/0702075 [astro-ph] .

[146] K. Itagaki, Transient Name Server Discovery Report **2023-1158**, 1 (2023).

[147] C. D. Kilpatrick *et al.*, The Astrophysical Journal Letters **952**, L23 (2023), arXiv:2306.04722 [astro-ph.SR] .

[148] L. Ferrari *et al.*, Astronomy & Astrophysics **687**, L20 (2024), arXiv:2406.00130 [astro-ph.SR] .

[149] I. L. Rosa *et al.*, Universe **7**, 218 (2021).

[150] E. Capote *et al.*, Physical Review D **111**, 062002 (2025), arXiv:2411.14607 [gr-qc] .

[151] Gravitational Wave Open Science Center, O4 instrumental lines (2024).

[152] D. A. Perley, A. Gal-Yam, I. Irani, and E. Zimmerman, Transient Name Server AstroNote **119**, 1 (2023).

[153] K. A. Bostroem *et al.*, The Astrophysical Journal Letters **956**, L5 (2023), arXiv:2306.10119 [astro-ph.HE] .

[154] W. Jacobson-Galán, Universe **11**, 231 (2025), arXiv:2507.08078 [astro-ph.HE] .

[155] A. G. Abac *et al.*, The Astrophysical Journal **985**, 183 (2025), arXiv:2410.16565 [astro-ph.HE] .

[156] D. Guetta, A. Langella, S. Gagliardini, and M. Della Valle, The Astrophysical Journal Letters **955**, L9 (2023), arXiv:2306.14717 [astro-ph.HE] .

[157] G. Li *et al.*, Nature **627**, 754 (2024), arXiv:2311.14409 [astro-ph.HE] .

[158] G. Hosseinzadeh *et al.*, The Astrophysical Journal Letters **953**, L16 (2023), arXiv:2306.06097 [astro-ph.HE] .

[159] W. V. Jacobson-Galán *et al.*, The Astrophysical Journal Letters **954**, L42 (2023), arXiv:2306.04721 [astro-ph.HE] .

[160] N. Smith *et al.*, The Astrophysical Journal **956**, 46 (2023), arXiv:2306.07964 [astro-ph.HE] .

[161] B. W. Grefenstette *et al.*, The Astrophysical Journal Letters **952**, L3 (2023), arXiv:2306.04827 [astro-ph.HE] .

[162] D. Matthews *et al.*, Transient Name Server AstroNote **146**, 1 (2023).

[163] S. Soni *et al.*, Classical and Quantum Gravity **42**, 085016 (2025), arXiv:2409.02831 [astro-ph.IM] .

[164] D. Hiramatsu *et al.*, The Astrophysical Journal Letters **955**, L8 (2023), arXiv:2307.03165 [astro-ph.HE] .

[165] S. S. Menon *et al.*, in *Journal of Physics Conference Series*, Journal of Physics Conference Series, Vol. 3177 (IOP, 2026) p. 012121.

[166] M. Oliver, D. Keitel, and A. M. Sintes, Physical Review D **99**, 104067 (2019), arXiv:1901.01820 [gr-qc] .

[167] F. Attadio *et al.*, Physical Review D **110**, 103047 (2024), arXiv:2407.02391 [astro-ph.IM] .

[168] A. L. Miller *et al.*, Physical Review D **100**, 062005 (2019), arXiv:1909.02262 [astro-ph.IM] .